2013

Melt generation beneath Arctic Ridges: Implications from Ule

Lynne J. Elkins
Bryn Mawr College, lelkins@brynmawr.edu

K. W. Sims

J. Prytulak

J. Blichert-Toft

T. Elliott

See next page for additional authors

Custom Citation

Elkins, L.J., Sims, K.W.W., Prytulak, J., Blichert-Toft, J., Elliott, T., Blusztajn, J., Fretzdorff, S., Reagan, M., Haase, K., Humphris, S., Schilling, J.-G., "Melt generation beneath Arctic Ridges: Implications from U decay series disequilibria in the Mohns, Knipovich, and Gakkel Ridges", *Geochimica et Cosmochimica Acta* (2013)

Authors
Lynne J. Elkins; K. W. Sims; J. Prytulak; J. Blichert-Toft; T. Elliott; J. Blusztajn; S. Fretzdorff,; M. Reagan; K. Haase; S. Humphris; and J.-G. Schilling

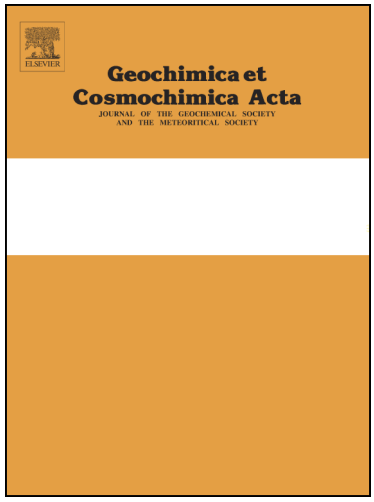

Melt generation beneath Arctic Ridges: Implications from U decay series disequilibria in the Mohns, Knipovich, and Gakkel Ridges

L.J. Elkins, K.W.W. Sims, J. Prytulak, J. Blichert-Toft, T. Elliott, J. Blusztajn, S. Fretzdorff, M. Reagan, K. Haase, S. Humphris, J.-G. Schilling

PII: S0016-7037(13)00670-4
DOI: http://dx.doi.org/10.1016/j.gca.2013.11.031
Reference: GCA 8564

To appear in: *Geochimica et Cosmochimica Acta*

Received Date: 22 February 2013
Accepted Date: 25 November 2013

Please cite this article as: Elkins, L.J., Sims, K.W.W., Prytulak, J., Blichert-Toft, J., Elliott, T., Blusztajn, J., Fretzdorff, S., Reagan, M., Haase, K., Humphris, S., Schilling, J.-G., Melt generation beneath Arctic Ridges: Implications from U decay series disequilibria in the Mohns, Knipovich, and Gakkel Ridges, *Geochimica et Cosmochimica Acta* (2013), doi: http://dx.doi.org/10.1016/j.gca.2013.11.031

Melt generation beneath Arctic Ridges: Implications from U decay series disequilibria in the Mohns, Knipovich, and Gakkel Ridges

L.J. Elkins[a,b] *, K.W.W. Sims[c,b], J. Prytulak[d,e], J. Blichert-Toft[f], T. Elliott[e], J. Blusztajn[b], S. Fretzdorff[g], M. Reagan[h], K. Haase[i], S. Humphris[b], J.-G. Schilling[j]

[a] Bryn Mawr College, Bryn Mawr, PA, USA
[b] Woods Hole Oceanographic Inst., Woods Hole, MA, USA
[c] University of Wyoming, Laramie, WY, USA
[d] Imperial College, London, UK
[e] Bristol Isotope Group, University of Bristol, Bristol, UK
[f] Laboratoire de Géologie de Lyon, Ecole Normale Supérieure de Lyon and Université Claude Bernard Lyon 1, CNRS UMR 5276, 46 Allée d'Italie, 69007 Lyon, France
[g] Research Centre Juelich GmbH, Rostock, Germany
[h] University of Iowa, Iowa City, IA, USA
[i] GeoZentrum Nordbayern, Erlangen, Germany
[j] Univ. Rhode Island, Narragansett, RI, USA
* lelkins@brynmawr.edu, Department of Geology, Bryn Mawr College, Bryn Mawr, PA, USA, (610)526-7971, fax: (610)526-5180

Running title: Uranium-series excesses in Arctic MORB

Keywords: Arctic, mid-ocean ridge basalt, radium, thorium, protactinium, Gakkel

For submission to *Geochimica et Cosmochimica Acta*.

ABSTRACT

We present new ^{238}U-^{230}Th-^{226}Ra-^{210}Pb, ^{235}U-^{231}Pa, and Nd, Sr, Hf, and Pb isotope data for the slow- to ultraslow-spreading Mohns, Knipovich, and Gakkel Ridges. Combined with previous work, our data from the Arctic Ridges cover the full range of axial depths from the deep northernmost Gakkel Ridge shallowing upwards to the Knipovich, Mohns, and Kolbeinsey Ridges north of Iceland. Age-constrained samples from the Mohns and Knipovich Ridges have ($^{230}Th/^{238}U$) activity ratios ranging from 1.165 to 1.30 and 1.101 to 1.225, respectively. The high ^{230}Th excesses of Kolbeinsey, Mohns, and Knipovich mid-ocean ridge basalts (MORB) are erupted from ridges producing relatively thin (Mohns, Knipovich) to thick (Kolbeinsey) oceanic crust with evidence for sources ranging from mostly peridotite (Kolbeinsey) to eclogite-rich mantle (Mohns, Knipovich). Age-constrained lavas from 85ºE on the Gakkel Ridge, on the other hand, overlie little to no crust and range from small (~5%) ^{230}Th excesses to small ^{238}U excesses (~5%). The strong negative correlation between ($^{230}Th/^{238}U$) values vs. axial ridge depth among Arctic ridge basalts is controlled not only by solidus depth influence on ^{238}U-^{230}Th disequilibria, but also by variations in mantle source lithology and depth to the base of the lithosphere, which is expected to vary at ultra-slow spreading ridges. Small ^{231}Pa excesses (65% excess) in age-constrained basalts support the presence of eclogite in the mantle source for this region. Conversely, the ultraslow-spreading Gakkel Ridge basalts are homogeneous, with Sr, Nd, and Hf radiogenic isotopic signatures indicative of a long time-averaged depleted mantle source. The Gakkel samples have minimum ($^{226}Ra/^{230}Th$) ratios ranging from 3.07 to 3.65 ± 3%, which lie along and extend the global negative correlation between ^{226}Ra and ^{230}Th excesses observed in MORB. The new ^{230}Th-^{226}Ra data support a model for global MORB production in which deep

melts record interaction with shallower materials. This scenario requires either mixing with shallow-derived melts, or melt-rock reaction with shallower rocks in the lithosphere or crust.

1. INTRODUCTION

The thickness of oceanic crust produced by volcanism at mid-ocean ridges is a direct manifestation of the total quantity of mantle melt produced at a given ridge location. Based on correlations of mid-ocean ridge crustal thickness and major element composition, Klein and Langmuir (1987) proposed that thicker crust is produced by a longer mantle melt column and overall higher degree of melting, with the extent of melting being controlled by local mantle temperature. Bourdon et al. (1996b) further observed that the measured (^{230}Th/^{238}U) for mid-ocean ridge basalts (MORB) inversely correlates with depth to the ridge axis. They suggested that thicker crust (i.e. higher degree of melting) and a correspondingly deeper melt column produce higher (^{230}Th/^{238}U) by generating more melt in the garnet stability field. This model recently appeared to be supported by U-series data on the Kolbeinsey Ridge (Elkins et al., 2011), the Klein and Langmuir (1987) shallow ridge end member location, where thick crust is accompanied by relatively high (^{230}Th/^{238}U) in young, unaltered MORB.

Albeit a unifying global theory that couples physiographic and compositional information with depth of melting information provided by U-Th disequilibria, the study of Bourdon et al. (1996b) was limited by several factors: 1) the global MORB U-series data set available at the time was relatively small, making only a broad survey possible; 2) there was generally poor age control on the samples; and 3) their model of mantle temperature control on (^{230}Th/^{238}U) did not consider factors such as lithological heterogeneity in the mantle source to be as influential as temperature. This latter point has been raised by numerous other studies (Lundstrom, 2000; Niu

and Batiza, 1993, 1997; Niu et al., 2001; Russo et al., 2009; Sims et al., 2002; Sims et al., in press; Waters et al., 2011). The paradigm was later revisited in literature reviews that incorporated larger, more recent data sets (Elliott and Spiegelman, 2003; Lundstrom, 2003), where the inverse correlation continued to be statistically supported, though with relatively large scatter (Elliott and Spiegelman, 2003). Because the Arctic ridges show a wide range of axial depth but also overlie regions of chemically heterogeneous mantle (e.g. Andres et al., 2004; Blichert-Toft et al., 2005; Debaille et al., 2009; Devey et al., 1994; Elkins et al., 2011; Haase et al., 1996; Haase et al., 2003; Mertz et al., 1991; Mertz and Haase, 1997; Mertz et al., 2004; Schilling et al., 1999), they provide an important opportunity to evaluate the influence of source heterogeneity versus potential temperature control on U-series isotope variations of MORB.

An additional factor influencing the melt process at mid-ocean ridges is the rate of seafloor spreading, which ranges from ultraslow (≤12 mm/a) to slow (12-55 mm/a), intermediate (55-70 mm/a), and fast (≥70 mm/a) (Dick et al., 2003; Small, 1998). While recent studies have systematically explored the nature of crustal accretion and geochemical characteristics of MORB, considering evidence from U-series and long-lived isotopes, at fast-spreading ridges (Kokfelt et al., 2005; Lundstrom et al., 1998a; Lundstrom et al., 1999; Rubin et al., 2005; Sims et al., 2002; Sims et al., 2003; Turner et al., 2011; Waters et al., 2011; Waters et al., 2013a; b) and several slow-spreading locations (Elkins et al., 2011; Peate et al., 2001; Russo et al., 2009; Standish and Sims, 2010), measurements of U-series isotopes from the globally most ultraslow-spreading end member, the Gakkel Ridge, are lacking. Ultraslow-spreading mid-ocean ridges represent an important component of the global ridge system and thus are a critical setting in which to further explore basalt petrogenesis.

For some time the shallowest ridges studied were also the slowest spreading ridges, making it difficult to disentangle the effects of axial depth from those of spreading rate on (^{230}Th/^{238}U) (e.g., Elliott and Spiegelman, 2003). For the Arctic ridge system north of Iceland, however, the slowest spreading ridge (the Gakkel Ridge) also has a deep ridge axis, making it ideal for differentiating between the effects of spreading rate and axial depth on U-series disequilibria. The Arctic ridge system in fact spans the full range of shallow to deep axial ridge depth at slow- and ultraslow-spreading rates, from the shallow, thick, slow-spreading Kolbeinsey Ridge (averaging 1100 m deep) to the deep, thin, ultraslow-spreading Gakkel Ridge (up to 5000 m deep; Figure 1). The drastic variations in crustal thickness make the Arctic ridge system a good choice for studying the effects of factors such as magma supply and melt fraction, in addition to the effects of spreading rate. The chemically and isotopically heterogeneous mantle (e.g. Andres et al., 2004; Blichert-Toft et al., 2005; Debaille et al., 2009; Devey et al., 1994; Elkins et al., 2011; Haase et al., 1996; Haase et al., 2003; Mertz et al., 1991; Mertz and Haase, 1997; Mertz et al., 2004; Schilling et al., 1999) underlying the slow-spreading Arctic ridges likewise provides a test of the role of source heterogeneity on U-series isotope variations. Therefore this region is an important location to simultaneously study all three factors (mantle heterogeneity, crustal thickness, and ridge spreading rate) and gauge their relative importance. Here we present ^{238}U-^{230}Th-^{226}Ra-^{210}Pb and ^{235}U-^{231}Pa disequilibria and Nd, Sr, Pb, and Hf isotope data for a suite of submarine basaltic samples from the Arctic Mohns, Knipovich, and Gakkel Ridges (Table 1, Figure 1). These data provide constraints on the relationships between mantle temperature, source heterogeneity, spreading rate, and ocean crust production.

2. GEOLOGIC SETTING

Arctic mid-ocean ridges (Figure 1, Appendix A) vary significantly in spreading rate, angle of divergence, segment length, axial depth, crustal thickness, and extent of magmatism. Spreading rates range from slow (16-18 mm/a for the Knipovich, Mohns, and Kolbeinsey Ridges; Breivik et al., 2006; Mosar et al., 2002) to ultraslow (<13 mm/a for the Gakkel Ridge; Goldstein et al., 2008; Michael et al., 2003), and spreading direction ranges from nearly orthogonal (Kolbeinsey and Gakkel Ridges) to moderately (Mohns Ridge) or highly oblique (Knipovich Ridge; Okino et al., 2002) divergence, such that effective spreading rates on the Knipovich Ridge are ultraslow (Mosar et al., 2002). Ridge segments range from a series of small pull-apart basins forming a detachment zone on the Knipovich Ridge (Okino et al., 2002; Sokolov, 2011; Yampol'skiy and Sokolov, 2012), to extremely long, unbroken segments along most of the Mohns and Gakkel Ridges (Klingelhofer et al., 2000). Crustal thickness steadily decreases and axial depth correspondingly increases northward from the anomalously shallow Kolbeinsey Ridge along the entire Arctic ridge system, culminating with the very deep Gakkel Ridge, which has little to no crust (Jokat and Schmidt-Aursch, 2007; Jokat et al., 2012; Kandilarov et al., 2008; Klingelhofer et al., 2000; Kodaira et al., 1997; Ljones et al., 2004; Mjelde et al., 2008; Okino et al., 2002; Ritzmann et al., 2002). Likewise, volcanic activity is continuous and ridge-focused on the more southerly Kolbeinsey and Mohns Ridges but is intermittent along the Knipovich Ridge (Crane et al., 2001). Volcanism is limited to isolated volcanic centers along the Western Volcanic Zone (WVZ) and Eastern Volcanic Zone (EVZ) of the Gakkel Ridge and is almost nonexistent in the Gakkel Ridge's central Sparsely Magmatic Zone (SMZ) (Goldstein et al., 2008; Michael et al., 2003).

Previous work has examined the major element, trace element, and long-lived radiogenic isotopic compositions of MORB from the Arctic mid-ocean ridges (Andres et al., 2004; Blichert-

Toft et al., 2005; Debaille et al., 2009; Devey et al., 1994; Elkins et al., 2011; Goldstein et al., 2008; Haase et al., 1996; Haase et al., 2003; Hanan et al., 2000; Lassiter and Snow, 2009; Liu et al., 2008; Mertz and Haase, 1997; Mertz et al., 1991; Mertz et al., 2004; Nauret et al., 2010; Nauret et al., 2011; Neumann and Schilling, 1984; Salters, 1996; Schilling et al., 1983; Schilling et al., 1999; Stracke et al., 2011; Trønnes et al., 1999; Waggoner, 1989). Unlike the overall depletion in trace elements and radiogenic isotopes on the adjacent Kolbeinsey Ridge (where "depletion" refers to long-term incompatible element depletion as manifested through less radiogenic $^{87}Sr/^{86}Sr$, $^{206}Pb/^{204}Pb$, $^{207}Pb/^{204}Pb$, and $^{208}Pb/^{204}Pb$ and high ε_{Nd} and ε_{Hf}) (Andres et al., 2004; Blichert-Toft et al., 2005; Devey et al., 1994; Elkins et al., 2011; Hanan et al., 2000; Mertz et al., 1991; Mertz and Haase, 1997; Salters, 1996; Schilling et al., 1999; Schilling et al., 1983; Waggoner, 1989), the more northerly Jan Mayen Island region and Mohns and Knipovich Ridges have overall more enriched signatures, including a DUPAL-type $^{208}Pb/^{204}Pb$ and $^{207}Pb/^{204}Pb$ anomaly (Andres et al., 2004; Blichert-Toft et al., 2005; Debaille et al., 2009; Devey et al., 1994; Elkins et al., 2011; Haase et al., 1996; Haase et al., 2003; Hanan et al., 2000; Mertz and Haase, 1997; Mertz et al., 1991; Mertz et al., 2004; Neumann and Schilling, 1984; Schilling et al., 1999; Schilling et al., 1983; Trønnes et al., 1999; Waggoner, 1989). The exception to this pattern is Mohns and Knipovich Ridge ε_{Hf}, which is anomalously depleted for these two ridges. Overall, the radiogenic isotope systematics of Jan Mayen-Mohns-Knipovich volcanic rocks have been interpreted as indicating ancient plume-derived mantle material mixing with subcontinental lithospheric mantle remnants in an otherwise typical upper mantle peridotite melt source (Andres et al., 2004; Blichert-Toft et al., 2005; Debaille et al., 2009; Haase et al., 1996; Haase et al., 2003; Hanan et al., 2000; Mertz et al., 2004; Neumann and Schilling, 1984; Schilling et al., 1999; Schilling et al., 1983; Waggoner, 1989). While MORB from the WVZ of the Gakkel

Ridge likewise have relatively enriched signatures and a DUPAL-type Pb isotope anomaly thought to indicate the presence of abundant recycled material in the underlying mantle, EVZ basalts are trace element and isotopically depleted and seem to derive from a background mantle source different from their western counterparts (Goldstein et al., 2008).

3. METHODS

3.1. Sample selection and preliminary processing

Samples measured for this study include dredged basaltic glasses from cruises R/V Trident leg 139 in 1971, R/V Endeavor leg 26 in 1973, and a R/V Professor Logatchev expedition to the Knipovich Ridge in 1996, as well as samples retrieved by the Camper ROV on the R/V Oden Expedition 11/AGAVE expedition (2007) (Table 1, Figure 1). Samples were selected for sufficient quantities of fresh basaltic glass (> 1 g). Processing of samples involved the following steps: handpicking glass fragments for absence of visible crystals, surface alteration, or cloudiness; lightly leaching handpicked material for 15 minutes in 0.1 N oxalic acid + 2% hydrogen peroxide, rinsing in high purity distilled water, and leaching for 15 minutes in 0.1 N hydrochloric acid + 2% hydrogen peroxide followed by water rinses; and, finally, handpicking one to two more times for high-quality glass chips. The leaching procedure was used to remove any potential Mn oxide coating that remained unseen during picking (e.g. Bourdon et al., 2000; Lundstrom et al., 1999; Sims et al., 2003). Additional 10-gram aliquots of three Gakkel Ridge samples were crushed and processed for ^{210}Pb analysis by alpha counting methods. Further analytical details for all involved analytical facilities are included in Appendix B.

3.2. ^{238}U-^{230}Th and U and Th concentrations

($^{230}Th/^{232}Th$) was measured by multi-collector inductively-coupled plasma mass spectrometry (MC-ICP-MS) using Thermo Fisher NEPTUNE instruments at both the Woods Hole Oceanographic Institution (WHOI) (Ball et al., 2008; Sims et al., 2008a; Sims et al., 2008b) and the University of Bristol (Hoffmann et al., 2007; Sims et al., 2008b), and a Micromass PlasmaTrace 2 at the Institute of Geosciences, Kiel University, Kiel, Germany (Fretzdorff et al., 2003). Replicate analyses represent either repeat analyses of a single sample dissolution or separate dissolutions entirely, as listed in Table 2. Separate analyses from each facility are likewise listed in Table 2. Uncertainties in ^{238}U-^{230}Th isotopic measurements from the various laboratory facilities for this study are reported in Table 2 and are on the order of 2-3% (2σ for ($^{238}U/^{232}Th$) and 0.1-1% (2σ for ($^{230}Th/^{232}Th$) activity ratios. Additional analytical details and standard values are available in Ball et al. (2008), Elkins et al. (2011), Fretzdorff et al. (2003), Hoffmann et al. (2007), and Sims et al. (2008a, b) and in Appendix B.

Rock standards measured as unknowns during analytical runs are in good agreement between laboratories and are reproduced in Table 2. Analytical results between the WHOI and Bristol laboratories for this study are overall within their given 2σ uncertainties (Table 2). Notably, disequilibrium measurements of all dissolutions are within 2 % of the mean disequilibrium for all replicates. However, four samples had discrepancies between different analyses: END0026-010-001G and END0026-030-001G had higher U and Th concentrations in one set of Bristol measurements than in other replicates (5-7% and more than 30% higher, respectively), and samples TRI0139-030-002G and END0026-012-002G measured at Bristol had lower ($^{230}Th/^{232}Th$) than WHOI replicates (2% and 3% lower, respectively). Because these analyses represent separate dissolutions, the disparity could be explained by sample

heterogeneity. Alternately, incomplete equilibration between spike and sample during digestion is possible, but we consider this highly unlikely as samples were fumed repeatedly during digestion (see Appendix B for further details). We also expect that for a mixed 236U-229Th spike as used at the University of Bristol, poor sample-spike equilibration would influence Th concentration measurements far more than U measurements, which we do not observe. A more likely explanation, especially for the largest discrepancy of 30%, is either a weighing error or simple weight recording error, which would influence elemental abundances but not determination of disequilibrium given the use of a mixed ^{236}U-^{229}Th spike; a large weighing error is especially possible when using a highly concentrated spike, as occurred at the University of Bristol. Replicate disequilibrium measurements are in good agreement for all four samples (within 2 % of the mean disequilibrium for all replicates). Unfortunately, it is not possible to be definitive about the causes of these discrepancies, but we stress that they have no bearing on the inferences of this work.

3.3. ^{238}U-^{234}U

(^{234}U/^{238}U) was measured by MC-ICP-MS (Thermo Fisher NEPTUNE) at WHOI and the University of Bristol (Ball et al., 2008; Hoffmann et al., 2007; Sims et al., 2008a; Sims et al., 2008b). We report U isotopic uncertainties on the order of 0.2-0.5% (2σ for internal reproducibility and 0.5% (2σ for accuracy of rock standards, consistent with previous results using similar methods (e.g. Ball et al., 2008; Hoffmann et al., 2007; Koornneef et al., 2010; Richter et al., 2006; Rubin et al., 2005; Sims et al., 2008b) (Table 2). Rock standard analyses conducted alongside our samples are likewise consistent with previous results for those standards and are reproduced in Table 2. Further details regarding the analytical procedures used in the

laboratories where our measurements were conducted are available from Ball et al. (2008), Elkins et al. (2011), Hoffmann et al. (2007), Prytulak et al. (2008), and Sims et al. (2008b; 2013a), and in Supplementary Materials.

($^{234}U/^{238}U$) is a sensitive indicator of basalt alteration by interaction with seawater (($^{234}U/^{238}U$) = 1.14 ± 0.05 (Thurber, 1962)) or other seawater-derived crustal materials, such as low-temperature mineral precipitates or seawater-derived brines. A number of detailed treatments of variations in ($^{234}U/^{238}U$) activity ratios in basalts have previously demonstrated the importance of considering U isotopes when evaluating secondary alteration (e.g. Aumento, 1971; Bacon, 1978; Bourdon et al., 2000; Elkins et al., 2011; Glass et al., 2005; Macdougall, 1977; Macdougall et al., 1979; Moran and Buesseler, 1992, 1993; Pelt et al., 2008; Pietruszka et al., 2009; Pietruszka et al., 2011; Sims and Hart, 2006; Sims et al., 2002; Sims et al., 2003; Turekian and Bertine, 1971). Unaltered, uncontaminated basalt is here assumed to have ($^{234}U/^{238}U$) in equilibrium (i.e. ($^{234}U/^{238}U$) = 1.000) (e.g. Bourdon et al., 2000; Elkins et al., 2011; Ku et al., 1977; Macdougall et al., 1979; Pietruszka et al., 2011; Sims et al., 2003; Sims et al., 2002). Based on MC-ICP-MS analytical precision in MORB (e.g. Elkins et al., 2011; Table 2), we take ($^{234}U/^{238}U$) = 1.000 ± 0.5% to indicate secular equilibrium and thus minimal alteration of a rock.

3.4. ^{230}Th-^{226}Ra

Limited by the abundance of fresh glass (^{226}Ra analyses typically require > 1.5 g of MORB), we measured ($^{226}Ra/^{230}Th$) ratios only on seven samples by MC-ICP-MS at WHOI. Additional details of methods, analytical precisions, and reproducibilities are available in Elkins et al. (2011) and Sims et al. (2008b), and in Supplementary Material.

3.5. ^{235}U-^{231}Pa

Although also limited by sufficient availability of fresh glass, ($^{231}Pa/^{235}U$) was successfully analyzed by MC-ICP-MS for four samples at the University of Bristol. ^{235}U-^{231}Pa was not measured in samples from the Gakkel Ridge due to the later expedition and sampling dates, which made such analyses unfeasible. Further analytical details are available in Elkins et al. (2011), Prytulak et al. (2008), and Regelous et al. (2004) and in Supplementary Material.

3.6. ^{226}Ra-^{210}Pb

We further measured ^{210}Pb ($t_{1/2}$ = 22.6 ± 0.1 years; Holden, 1990) by alpha counting of ^{210}Po at the University of Iowa in three fresh, glassy Gakkel Ridge samples (Table 2) using methods of Reagan et al. (2005) and Waters et al. (2013a) (see Supplementary Material). Uncertainties for alpha counting measurements range from 7-11% (2σ, Table 2).

3.7. $^{87}Sr/^{86}Sr$, $^{143}Nd/^{144}Nd$, $^{206}Pb/^{204}Pb$, $^{207}Pb/^{204}Pb$, $^{208}Pb/^{204}Pb$ and $^{176}Hf/^{177}Hf$

$^{87}Sr/^{86}Sr$, $^{143}Nd/^{144}Nd$, $^{206}Pb/^{204}Pb$, $^{207}Pb/^{204}Pb$, $^{208}Pb/^{204}Pb$, and $^{176}Hf/^{177}Hf$ were measured for all those samples of the present study for which literature data were not available (Table 3) (for previous chemical and isotopic analyses, see Blichert-Toft et al., 2005; Hanan et al., 2000; Neumann and Schilling, 1984; Schilling et al., 1999; Schilling et al., 1983; Sigurdsson, 1981; Waggoner, 1989). All Hf and some Nd isotope ratios were measured by MC-ICP-MS (Nu Plasma HR) at the Ecole Normale Supérieure de Lyon. Sr and Pb isotope ratios were measured by MC-ICP-MS at WHOI. The Sr, Nd, and Pb isotope ratios for the three Knipovich Ridge samples were analyzed on leached glasses using a Finnigan MAT 262 mass spectrometer at GEOMAR, Kiel, Germany. Additional analytical details for all procedures are presented in

Blichert-Toft (2001), Blichert-Toft et al. (2005; 1997), Sims et al., 2013a; Elkins et al. (2011), Haase et al. (2004), Hart and Blusztajn (2006), Jackson and Hart (2006), Sims and Hart (2006), and Todt et al. (1996), and in Supplementary Material.

4. RESULTS

4.1. U-series isotopes in Arctic MORB

We measured 23 samples with U isotopes in equilibrium (($^{234}U/^{238}U$) = 1.000 ± 0.005) and four samples (END0026-014-001G, END0026-016-001G, END0026-032D-003G, END0026-021D-001G) with ($^{234}U/^{238}U$) ratios outside of analytical error of unity (Table 2). We consider these samples altered by secondary processes and therefore do not interpret their disequilibria in terms of primary magmatic processes. In keeping with their "enriched" trace element and radiogenic isotope characteristics, Mohns and Knipovich Ridge samples have relatively low ($^{238}U/^{232}Th$) ratios (0.74-0.92). These samples have ($^{230}Th/^{238}U$) (1.10-1.30; Table 2). Basalt samples from the EVZ of the Gakkel Ridge are relatively homogeneous with higher ($^{238}U/^{232}Th$) ratios (1.29-1.39). Gakkel MORB have particularly low, near-equilibrium ($^{230}Th/^{238}U$) ratios ranging from 0.95 to 1.05 (Table 2, Figure 3).

Of the 15 samples analyzed for ^{226}Ra concentrations, three basalts were in secular equilibrium (($^{226}Ra/^{230}Th$) = 1.00 ± 0.03), while 12 exhibited disequilibrium ($^{226}Ra/^{230}Th$) (1.05-3.7) outside of analytical uncertainties. Figure 4 shows ($^{226}Ra/^{230}Th$) and ($^{230}Th/^{238}U$) isotope results alongside the global data set. ($^{231}Pa/^{235}U$) in four samples from the Mohns and Knipovich Ridges (1.37-1.68; Table 2) are low relative to global MORB (e.g. age-constrained ($^{231}Pa/^{235}U$) = 2.43-2.91 on the EPR; Sims et al., 2002). The three measured samples from 85ºE on the Gakkel

Ridge have (^{210}Pb/^{226}Ra) in equilibrium, which does not limit their eruption ages further (Table 2).

4.2. Long-lived radiogenic isotopes

Our new measurements corroborate previous work showing that basalts from the Mohns and Knipovich Ridges are relatively variable and overall enriched in both trace element abundances and long-lived radiogenic isotopes (Andres et al., 2004; Blichert-Toft et al., 2005; Devey et al., 1994; Elkins et al., 2011; Goldstein et al., 2008; Haase et al., 1996; Haase et al., 2003; Hanan et al., 2000; Mertz et al., 1991; Mertz and Haase, 1997; Mertz et al., 2004; Neumann and Schilling, 1984; Schilling et al., 1999; Schilling et al., 1983; Trønnes et al., 1999; Waggoner, 1989) (Table 3, Figure 2). Similar to the previously measured EVZ lavas (Goldstein et al., 2008), our samples from the 85ºE volcanic center on the Gakkel Ridge are relatively isotopically uniform and come from a source indicative of long-term trace element depletion without "DUPAL"-type anomalies (EVZ: ^{208}Pb/^{206}Pb = 2.087 - 2.093, ^{207}Pb/^{204}Pb = 15.4270 - 15.4383, ^{208}Pb/^{204}Pb = 37.5402 - 37.6198; Table 3) observed on the Western Gakkel Ridge (Goldstein et al., 2008) and the Mohns and Knipovich Ridges (Blichert-Toft et al., 2005) (Table 3, Figure 2). As previously observed (Andres et al., 2004; Blichert-Toft et al., 2005), the Mohns and Knipovich Ridges have relatively high ε_{Hf}, particularly when compared to our EVZ Gakkel Ridge basalts. As in Salters et al. (2011), our Knipovich Ridge ε_{Hf} values are at the high extreme for global MORB, whereas the Gakkel Ridge samples are closer to the low extreme.

4.3. Disequilibria in Arctic basalts

4.3.1 Age constraints and filtering

If undisturbed, disequilibrium U-series activity ratios return to secular equilibrium within ~5 half-lives of the daughter nuclide. Hence, age constraints are necessary for robust interpretation of measured U-series in MORB. In the absence of such constraints, measured disequilibria are treated as minimum values.

Mid-ocean ridge basalts from the Kolbeinsey Ridge are known to be <10 ka based on eruption through sedimentary outwash from the end of the last glacial maximum (Elkins et al., 2011). The Mohns, Knipovich, and Gakkel Ridges, however, lack sedimentary constraints on eruption age, so we constrain the eruption ages based on U-series nuclides: if a sample has $(^{230}Th/^{238}U) \neq 1$, it is less than 375 ka in age; for $(^{231}Pa/^{235}U) \neq 1$, the sample is younger than 150 ka; for $(^{226}Ra/^{230}Th) \neq 1$, the sample is younger than 8 ka; and for $(^{210}Pb/^{226}Ra) \neq 1$, its age is < 100 years. Because of the large differences in half-life, measurement of disequilibria for the shorter-lived systems indicates that interpretations of primary magmatic processes based on disequilibria among the longer-lived nuclides are robust.

No samples have measurable $(^{210}Pb/^{226}Ra)$ disequilibrium, so none are constrained to <100 years. Twelve are constrained by $(^{226}Ra/^{230}Th) > 1$ to less than 8 ka, 11 of which are unaltered ($(^{234}U/^{238}U) = 1.000 \pm 0.5\%$) (see above). Two samples, one of which is unaltered (END0026-012-002G), have $(^{231}Pa/^{235}U) >1$ but either no ^{226}Ra data or $(^{226}Ra/^{230}Th) = 1.00 \pm 3\%$, constraining eruption age to < 150 ka. The $(^{231}Pa/^{235}U)$ ratio of sample END0026-012-002G is thus a minimum value due to possible aging since eruption. All remaining samples have $(^{230}Th/^{238}U) \neq 1$, restricting their ages to < 375 ka (Table 2).

4.3.2. Primary disequilibria in Arctic basalts

Only samples considered unaltered based on visual (i.e. handpicked fresh glass) or chemical (i.e. no measured ^{238}U-^{234}U disequilibrium) evidence are discussed below. This criterion eliminates four samples with ($^{234}U/^{238}U$) > 1.005 (Table 2, Figure 3). We choose to include in our discussion U-series data from four Knipovich Ridge samples without measured ($^{234}U/^{238}U$) (samples END0026-011D-1G, PL96 67-2, PL96 57-1, PL96 54-3), because they have ($^{230}Th/^{238}U$) values similar to Knipovich Ridge samples with ($^{234}U/^{238}U$) in secular equilibrium. We include them with the reservation that these samples may have experienced alteration, which we would expect to result in lowered ($^{230}Th/^{238}U$) ratios (e.g. Elkins et al., 2011; Pietruszka et al., 2011; Sims et al., 2003). All Knipovich Ridge samples without elevated ($^{234}U/^{238}U$) as evidence for alteration (five samples total) have moderately high ^{230}Th excesses (10% - 22%). Those five samples span a broad range of ($^{230}Th/^{232}Th$) (0.905-1.13) and ($^{238}U/^{232}Th$) (0.739-0.940), forming an array with a slope of 1.0 parallel to the equiline (Figure 3; $r^2 = 0.8$) and consistent with source heterogeneity control for Knipovich MORB. We observe that the slope is strongly controlled by one sample with a low value (Table 2). We further note that two samples from the Eggvin Bank area on the neighboring Northern Kolbeinsey Ridge segment span a similar sloped range (slope = 1.9) (Elkins et al., 2011).

We can constrain the ages of only two Knipovich and four Mohns Ridge samples. Unconstrained samples are included in figures (distinguished using smaller data symbols, e.g. Figure 3), but their disequilibrium values should be treated as minimum ratios. Age-constrained Mohns Ridge samples are relatively homogeneous compared to the unfiltered data set, clustering with a mean ^{230}Th excess of 22%. The two unaltered samples with age-constrained ($^{231}Pa/^{235}U$) disequilibria (END0026-010-001G from the Mohns Ridge and END0026-030-001G from the Knipovich Ridge) have relatively low ($^{231}Pa/^{235}U$) ratios (1.60-1.65 compared to MORB; e.g.

age-constrained ($^{231}Pa/^{235}U$) = 2.43-2.91 on the EPR, which overlap with unaltered samples from the Kolbeinsey Ridge; Elkins et al., 2011; Sims et al., 2002).

The three measured samples from 85ºE on the Gakkel Ridge are within uncertainty of ($^{210}Pb/^{226}Ra$) equilibrium (Table 2), indicating that the Gakkel Ridge samples have eruption ages older than 100 years or that they were erupted with no initial disequilibria. Without additional constraints we consider the ($^{226}Ra/^{230}Th$) disequilibria in the Gakkel samples as minimum values, despite being among the highest ($^{226}Ra/^{230}Th$) measured in any MORB. All Gakkel Ridge samples are chemically unaltered, with ($^{234}U/^{238}U$) of unity.

To remove possible chemical effects of alteration when considering the global MORB data in the literature (below), we restrict our data compilation to age-constrained samples with uranium isotope measurements and a filtering criterion of ($^{234}U/^{238}U$) = 1.00 ± 1%. This is less strict than the filtering criterion we use above for our own samples (($^{234}U/^{238}U$) = 1.000 ± 0.5%) due to our in-house knowledge of our analytical precision (Table 2). While recent, high precision (± 0.5 %) measurements are generally in equilibrium (Bourdon et al., 2000; Cooper et al., 2003; Elkins et al., 2011; Rubin et al., 2005; Russo et al., 2009; Sims et al., 2003; Sims et al., 2002; Standish and Sims, 2010; Sturm et al., 2000; Waters et al., 2011; 2013a; 2013b), some older studies have significantly lower precision and generally show higher disequilibria (Goldstein et al., 1989; Goldstein et al., 1991; Lundstrom et al., 1998a; Lundstrom et al., 1999; Peate et al., 2001; Tepley et al., 2004; Zou et al., 2002) (see Figure 7 in Elkins et al., 2011).

5. DISCUSSION: ARCTIC MELT GENERATION AND GLOBAL MORB PETROGENESIS

5.1. Geochemistry of Arctic MORB

The depth of the peridotite solidus as controlled by mantle potential temperature has been predicted as a controlling factor in producing varying crustal thicknesses (Klein and Langmuir, 1987) and by inference basaltic geochemical compositions (Klein and Langmuir, 1987) and ^{238}U-^{230}Th disequilibria (Bourdon et al., 1996b). In particular, using time-dependent melting models, Bourdon et al. (1996b) explained a broad global negative correlation between axial ridge depth and ($^{230}Th/^{238}U$) by inferring mantle temperature control over melt column depth (i.e. the depth to the peridotite solidus). Because the solidus depth controls the length of the melt column, this depth (whether inferred or an explicit model parameter) influences both the duration of melting during upwelling and the overall degree and quantity of melt produced in the garnet peridotite stability field, where $D_U > D_{Th}$, producing ($^{230}Th/^{238}U$) > 1 in the magma (Beattie, 1993a, b; Elkins et al., 2008; Hauri et al., 1994; La Tourette and Burnett, 1992; La Tourette et al., 1993; Landwehr et al., 2001; Salters and Longhi, 1999; Salters et al., 2002; Wood et al., 1999).

Figure 5 shows the relation between ($^{230}Th/^{238}U$) and axial depth for the Arctic mid-ocean ridge system. The Arctic data set nearly spans the complete range of both axial depth (250-4131 m) and ($^{230}Th/^{238}U$) (0.955-1.296) for MORB globally. The negative trend initially observed and modeled by Bourdon et al. (1996b) is considerably stronger for Arctic MORB than for the global data set: Elliott and Speigelman (2003) measured a weakly correlated r_s coefficient of -0.58 for all global ridge data, but the Arctic ridges alone (this study, Elkins et al., 2011) are strongly correlated with axial depth (r_s = -0.72; Figure 5). The high ($^{230}Th/^{238}U$) values measured in Kolbeinsey (Elkins et al., 2011), Mohns, and Knipovich MORB reflect melting that likely initiates in the presence of garnet. In contrast, EVZ Gakkel Ridge basalts erupt through very thin crust (Jokat and Schmidt-Aursch, 2007), and major element data (e.g. high MgO and Na_8) suggest that they are the result of smaller degrees of melting than is occurring at the other Arctic

ridges (Hellebrand et al., 2002; Michael et al., 2003). The overall low (^{230}Th/^{238}U) ratios in Gakkel MORB suggest a relatively shallow melt regime dominated by spinel peridotite (Figures 2, 3). The scatter observed in the global data set likely represents the influence and importance of a number of variables on melting, such as solidus depth, source heterogeneity, spreading rate, and the efficiency of melt extraction (see below for further details). We also consider all unaltered, age-constrained MORB data, while Bourdon et al. (1996b) only considered averaged (^{230}Th/^{238}U) compositions for each ridge segment in an attempt to omit local variations in MORB melting and melt transport regimes, which would create additional scatter in Figure 5.

The trend for age-constrained, unaltered MORB from slow- and ultraslow-spreading Arctic ridges appears initially to support the hypothesis that the depth to the peridotite solidus, and thus overall extent and initial depth of melting, exerts important control over crustal thickness, lava geochemistry, and the resulting (^{230}Th/^{238}U). In this model, MORB with high (^{230}Th/^{238}U) overlying thick axial crust (i.e. the Kolbeinsey Ridge) are the product of long melt columns with deep solidi, whereas MORB with low (^{230}Th/^{238}U) overlying thin or no crust (i.e. the Gakkel Ridge) are the product of short melt columns with shallow onset of melting (Bourdon et al., 1996b; Dick et al., 1984; Klein and Langmuir, 1987). The global relationship between (^{230}Th/^{238}U) and ridge depth in terms of simple solidus depth control was previously quantitatively explored by Bourdon et al. (1996b) using time-dependent melting models, whose results generally seemed to support a mantle solidus depth control on (^{230}Th/^{238}U) for most MORB. To compare the global model to the Arctic ridges, which cover a very wide range in ocean depth and thus crustal thickness, we have recalculated Bourdon et al. (1996b)'s peridotite porous flow model outcomes after Spiegelman and Elliott (1993) using the UserCalc program (Spiegelman, 2000; Figure 5) for slow and ultraslow passive melting rates of 1.1 x 10^{-4} kg/m^3/a

and 3.2 x 10^{-5} kg/m^3/a and maximum residual melt porosities of 0.1 to 0.5 %. For constant melt productivities of 0.5 %/kbar, these melting rates would correspond to solid mantle upwelling rates of 20 mm/a and 6 mm/a, respectively, which spans the range from the half spreading rate of the Gakkel Ridge EVZ (~6 mm/a) to more than twice the half-spreading rate of the Mohns Ridge (8.5 mm/a; Goldstein et al., 2008; Michael et al., 2003), thus encompassing passive upwelling as well as enhanced melting rates due to possible active upwelling near Jan Mayen. We assume a garnet peridotite source with 12% garnet, 8% clinopyroxene, 59% olivine, and 21% orthopyroxene (Table 4), and have included a change in peridotite mineralogy to reflect the loss of garnet at 25 kbar (instead of the older value of 20 kbar used by Bourdon et al. (1996b)) with updated, newer bulk partition coefficients (Table 4). Crustal thickness was determined from total melt fraction assuming complete melt extraction with a 15% density difference between mantle and crust, and corresponding axial depth was calculated using a simple isostatic model with 200 km compensation depth, no lithospheric mantle, dynamic support of the surrounding plate, and a density profile using densities after Lin et al. (1990) with 7-km thick crust overlain by 3 km of ocean water. This corresponds to a range of melt fractions from 10% for axial depths of 4 km to 22% melting as axial depths approach zero. We chose peridotite partition coefficients from more recent studies than those Bourdon et al. (1996b) had available (Salters and Longhi, 1999; Salters et al., 2002) due to more appropriate experimental temperature, pressure, and compositional conditions for peridotite mantle melting, and data for other coexisting mineral phases in the experimental runs. As previously discussed (e.g. Elliott and Spiegelman, 2003), it is difficult for dynamic melting calculations for peridotitic mantle to recreate the observed axial depth trends due to the overwhelming influence of deep, initial dynamic melt increments on (^{230}Th/^{238}U) in

the resulting liquids, so we limit our peridotite melting calculations in Figure 5 to reactive porous flow models after Spiegelman and Elliott (1993) and Spiegelman (2000).

The peridotite melt trajectories shown in Figure 5 demonstrate that our calculations cannot accurately reproduce the observed negative correlation between (^{230}Th/^{238}U) and axial depth in Arctic MORB. The more recent partition coefficients used here do slightly decrease the overall (^{230}Th/^{238}U) in the calculated melt relative to the calculations by Bourdon et al. (1996b), but they do not exert a strong control on the axial depth at which (^{230}Th/^{238}U) dramatically decreases. This is the most important way in which the calculations shown in Figure 5 fail to match global and Arctic data trends. This mismatch between measured MORB data and the shape of the modeled curves is principally due to the change in peridotite garnet-spinel reaction depth from 20 kbar in Bourdon et al. (1996b) to an updated, intermediate value of 25 kbar in this study (e.g., Klemme and O'Neill, 2000; Robinson and Wood, 1998; Walter et al., 2002): less melting consequently occurs in the garnet stability field, making it impossible to generate thin crust (i.e., a deep ridge axis) while maintaining a strong enough garnet signature (i.e., sufficiently high (^{230}Th/^{238}U)). We also note that models from previous works did not all continue to high enough axial depths to show the stepwise decrease to low, sustained (^{230}Th/^{238}U) in thin crust observed in Figure 5, but this is a necessary outcome of a melt column dominated by melting in the spinel peridotite stability field. The low (^{230}Th/^{238}U) of spinel peridotite-dominated melts at high axial depths is consistent across all peridotite melting models and is only slightly modified by differences in melting rate (Figure 5).

While these results do not preclude solidus depth exerting some control on the (^{230}Th/^{238}U) of MORB, it is necessary to consider other factors that may produce or influence the observed trend and contribute to the scatter observed in the global data set. Some discrepancies

between the measured data and the results of modeling calculations could be explained by the high degree to which U-series melt model outcomes are sensitive to uncertainties in mineral/melt partition coefficients (e.g., Elkins et al., 2011; Sims et al., 1999; Stracke et al., 2006), even with newer measurements using experimental conditions that more closely approach the mantle peridotite melting scenario (Salters and Longhi, 1999; Salters et al., 2002). However, this does not change the strong effect of the garnet-out reaction depth on the overall shape of the modeled trajectories.

Variations in melt productivities as a function of depth of melting (e.g. Asimow et al., 2001) may be important, in that higher melt productivities and higher melting rates are expected to reduce the (^{230}Th/^{238}U) observed in the melt. This is likely, however, to only increase the model misfit in Figure 5, since peridotite melt productivities are expected to be low until a melt fraction of several percent is reached, after which the productivities will increase continuously (Asimow et al., 2001). Increasing melt productivity over the course of the melting process would *decrease* the proportion of melting that occurs in the garnet peridotite stability field, causing our calculated curves to shift to even lower axial depths in Figure 5.

An additional possible source of variation is the relationship postulated between axial depth and crustal thickness (after Langmuir et al., 1992), which predicts: 1) an isostatically supported mantle column, and 2) a simple density relationship. For example, gravity data from the Gakkel Ridge may suggest an isostatically unsupported system (Coakley and Cochran, 1998). However, we do not expect this to shift the calculated curves far enough to the right in Figure 5 (i.e., to higher axial depths) to sufficiently explain global and Arctic MORB (^{230}Th/^{238}U) values. Altering the reference density profile used to calculate axial depth from crustal thickness can only accomplish an appropriately large shift of the calculated curves to greater axial depths if

crustal thickness is increased to unreasonably high values (> 8 km). Limiting the melt extraction to be less efficient, such that less than 100% of generated melts contributed to crustal thickness would only generate better matched model outcomes if deep melts with strong garnet signatures were preferentially sampled by ridge volcanism over shallower, spinel peridotite melts, which we consider mechanistically unlikely.

A further category of scenarios influencing MORB ($^{230}Th/^{238}U$) and/or axial depth considers shallow lithospheric processes occurring prior to eruption. Melt-rock reaction with lithospheric mantle during melt transport could plausibly occur beneath some ridges, particularly during slow melt transport; because those reactions would be controlled by the partitioning behavior of U and Th in the ambient spinel peridotitic rock, the effects on ($^{230}Th/^{238}U$) disequilibria may be difficult to distinguish from shallow peridotite melting. Models by Saal and Van Orman (2004) and Van Orman et al. (2006) considered the effects of disequilibrium melting and magma interaction with shallow crustal cumulates. These authors observed that effects similar to those generated by equilibrium porous flow models can be generated by chemical disequilibrium during melting, due to the differences in diffusion rates of U-series nuclides relative to isotopic decay rates (Van Orman et al., 2006). This chemical disequilibrium effect is, however, minor for ^{238}U-^{230}Th isotopic disequilibrium due to the similarity of U and Th diffusion coefficients (Van Orman et al., 2006), though it may more strongly affect the shorter-lived nuclides such as ^{226}Ra (Van Orman et al., 2006; see below).

New calculations by O'Neill and Jenner (2012) have suggested that open-system replenishment and cycling of mantle melts through magma chambers may significantly influence the trace element makeup of the subsequent basaltic eruptions. Overall, because garnet is absent in crustal magma chambers, we do not expect such processes to increase ($^{230}Th/^{238}U$) ratios in

basalts. However, they could influence ^{230}Th-^{226}Ra disequilibria: magma chamber processes, including continuous replenishment and crystallization, may more strongly influence U-series nuclides with shorter half-lives by creating disequilibria (e.g., high (^{226}Ra/^{230}Th) ratios) that are not subsequently diminished by aging during transport (see below). The extent to which variable shallow crustal effects occur, such as different degrees of magma chamber differentiation, magma replenishment and mixing, and reactions between the melt and crustal cumulates during transport, may influence U-series disequilibria to a small extent, contributing to the scattering observed in the global data set for ^{238}U-^{230}Th-^{226}Ra and ^{235}U-^{231}Pa. Such effects nonetheless fail to sufficiently explain the mismatch between the calculated model outcomes and measured data in Figure 5.

The models discussed above do not explicitly consider the depth of the top of the melting column (i.e. the base of the lithospheric cap, which, for example, is predicted to be as deep as 25 km for the Gakkel Ridge, and may also account for the deep fractionation of clinopyroxene in Knipovich MORB; Hellevang and Pedersen, 2005; Montesi and Behn, 2007), which is related to spreading rate and exerts an explicit control on melt column length. The steadily decreasing spreading rate northward along the Arctic Ridge system may influence overall degree of melting and crustal thickness by sub-adiabatic cooling near the surface and truncation of the melt column, particularly for solid upwelling rates slower than 1 cm/a (Montesi and Behn, 2007). A truncated melt column hence should generate lower overall degree of melting, decreasing resulting crustal thickness and increasing axial depth, while simultaneously increasing the relative influence of the deeper (garnet-bearing) part of the melt column on overall melt composition. In Figure 5 we show the result of an additional melt calculation for a truncated melt column, similar to those described above, with a melting rate of 1.1 x 10^{-4} kg/m^3/a, maximum

porosity of 0.1%, and a 20 km lithospheric cap during which no additional melting occurs. The resulting trajectory has higher (^{230}Th/^{238}U) than our other peridotite melting calculations and bounds much of the global and Arctic MORB data sets, though it is still too low to fully recreate those data. The overall shape of the curve (i.e., the axial depth at which (^{230}Th/^{238}U) drops abruptly due to the loss of garnet influence) likewise more closely resembles the shape of the measured Arctic data. We consider this more encouraging than the other peridotite melting models for slow and ultraslow spreading ridges, though it is difficult to generate the higher (^{230}Th/^{238}U) required to sufficiently explain global MORB generation. The predicted effect of a lithospheric cap suggests that spreading rate may be an important factor in producing crustal thickness variations at slow and ultraslow spreading ridges. The above calculations nonetheless still fail to explain the relatively high (^{230}Th/^{238}U) in the global data set, which includes intermediate and fast-spreading ridges that are not expected to overlie cold mantle lithosphere.

Finally, it has long been noted that the source of MORB is not homogeneous; both chemical and lithologic heterogeneity of the mantle source can influence ^{238}U-^{230}Th disequilibria in basalts (e.g. Langmuir et al., 1992; Niu and Batiza, 1993, 1997; Niu et al., 2001; Russo et al., 2009). Since both trace element ratios (e.g. U/Th or La/Sm) and long-lived radiogenic isotopes vary along the Arctic ridge system reflecting variations in underlying mantle composition (Figures 2, 4; Andres et al., 2004; Blichert-Toft et al., 2005; Debaille et al., 2009; Devey et al., 1994; Goldstein et al., 2008; Haase et al., 1996; Haase et al., 2003; Mertz et al., 1991; Mertz et al., 2004; Schilling et al., 1999; Trønnes et al., 1999), source heterogeneity is expected to influence the isotopic composition of Arctic MORB. For Knipovich and Mohns Ridge basalts, this mantle heterogeneity has been suggested to include a combination of enriched, recycled material and subcontinental lithospheric mantle remnants (Andres et al., 2004; Blichert-Toft et

al., 2005; Debaille et al., 2009; Devey et al., 1994; Goldstein et al., 2008; Haase et al., 1996; Haase et al., 2003; Mertz et al., 1991; Mertz et al., 2004; Schilling et al., 1999; Trønnes et al., 1999). To explore eclogitic melting further, we calculate the melt products of a recycled, eclogitic source in Figure 5, using the same model as for peridotite melting above. In Figure 5 (inset) we show the substantially higher (^{230}Th/^{238}U) ratios predicted for eclogitic melts compared to peridotitic melting conditions, both for a melting rate similar to peridotites for direct comparison (1.1 x 10^{-4} kg/m^3/a) and a higher melting rate (1.9 x 10^{-4} kg/m^{-3}/a), which would correspond to a solid upwelling rate of 2 cm/a for a higher constant melt productivity of 0.9 %/kbar (Table 4; Figure 5 inset; e.g., Elkins et al., 2011; Hirschmann and Stolper, 1996; Pertermann and Hirschmann, 2003a; Prytulak and Elliott, 2009; Waters et al., 2011). Crustal thicknesses produced by eclogite melting are calculated as above for peridotites, but assuming the eclogitic melting rates provided. Both melting rates produce similar results, and neither can reasonably explain the Arctic (^{230}Th/^{238}U) vs. axial depth variations by pure eclogite melting (Figure 5). Contributions of eclogitic melts to mantle melt mixtures contribute to the relatively high (^{230}Th/^{238}U) values observed as well as the scatter that persists in the filtered global data set, and particularly help resolve the mismatch between Knipovich and Mohns Ridge data and the calculated peridotite melt trajectories (Figure 5).

In support of a regional source heterogeneity effect in the Arctic mid-ocean ridge system, we observe that the U and Th isotope data for the Knipovich Ridge form a sloped array on a plot of (^{238}U/^{232}Th) vs. (^{230}Th/^{232}Th) (Figure 3). Heterogeneous source controls have previously been suggested to influence ^{238}U-^{230}Th on equiline diagrams (e.g. Lundstrom, 2000; Lundstrom et al., 1998b; Niu and Batiza, 1993, 1997; Niu et al., 2001; Russo et al., 2009; Sims et al., 2002; Waters et al., 2011): enriched eclogitic melt sources should be characterized by lower U/Th and

($^{238}U/^{232}Th$) ratios and correspondingly more enriched isotopic signatures (e.g. higher $^{87}Sr/^{86}Sr$), and melts from different mantle sources could mix to produce correlated arrays. We likewise observe a broad negative correlation between radiogenic isotopic composition ($^{87}Sr/^{86}Sr$) and both ($^{230}Th/^{232}Th$) and ($^{238}U/^{232}Th$) for the Knipovich Ridge (Figure 3c). Thus, for Knipovich MORB, and possibly for relatively enriched samples from the Mohns Ridge and neighboring Eggvin Bank as well, mantle heterogeneity could play a role in generating ^{238}U-^{230}Th disequilibria. This is in good agreement with considerable evidence for trace element and radiogenic isotope heterogeneity in the region (Andres et al., 2004; Blichert-Toft et al., 2005; Debaille et al., 2009; Devey et al., 1994; Goldstein et al., 2008; Haase et al., 1996; Haase et al., 2003; Mertz et al., 1991; Mertz et al., 2004; Schilling et al., 1999; Trønnes et al., 1999).

For increased sensitivity to variations in the timing of melting, which in turn is sensitive to the predicted elevated melting rates of mafic lithologies in a heterogeneous mantle, we measured ($^{231}Pa/^{235}U$) in uncontaminated, young Knipovich and Mohns Ridge basalts and found ratios > 1 (Table 2). Protactinium is more incompatible than U in all mantle lithologies, so any melting is expected to produce ^{231}Pa excesses in the melt (Blundy and Wood, 2003). Our measured Knipovich and Mohns Ridge ($^{231}Pa/^{235}U$) ratios are relatively low compared to the similarly slow-spreading, neighboring southern and central Kolbeinsey Ridge segments (($^{231}Pa/^{235}U$) = 2.26-2.50 for unaltered basalts; Elkins et al., 2011) and fast-spreading EPR MORB (age-constrained ($^{231}Pa/^{235}U$) = 2.43-2.91; Sims et al., 2002), and only slightly higher than the ($^{231}Pa/^{235}U$) previously measured for a nearby, age-constrained basalt from the Eggvin Bank (Figures 2, 6; Elkins et al., 2011). While only relatively few samples could be measured for ^{235}U-^{231}Pa disequilibria due to sample quantity limitations, the results are remarkably internally consistent and include age-constrained samples that are in good agreement with those for which

age constraints are not available. As discussed in further detail below and in agreement with the above observations, such small ^{231}Pa excesses are best explained by contributions from a mantle source containing eclogite.

The low (^{230}Th/^{238}U) of 85ºE Gakkel Ridge basalts suggests relatively shallow melt fractionation in the absence of garnet, and the presence of large minimum ^{226}Ra excesses (Figure 4) requires recent chemical fractionation with accompanying isotopic ingrowth. However, since the Gakkel Ridge axis likely overlies a thick lithospheric cap (Montesi and Behn, 2007), we envision a short melting column that is capped 15-25 km below the surface. The recently generated ^{226}Ra excesses observed thus require melt interaction with solid rock until relatively shallow (e.g., < 15 km) depths for all Gakkel Ridge samples. These Gakkel Ridge basalts, with low (^{230}Th/^{238}U) and high minimum (^{226}Ra/^{230}Th) values (3.07 to 3.65 ± 3%), lie at the extreme high (^{226}Ra/^{230}Th) end of the negative (^{226}Ra/^{230}Th) - (^{230}Th/^{238}U) trend observed in young MORB from the EPR (Sims et al., 2002) and unknown age samples from the Siqueiros Transform (Lundstrom et al., 1999), Garrett Transform (Tepley et al., 2004), and Juan de Fuca and Gorda Ridges (Goldstein et al., 1989; Goldstein et al., 1991; Goldstein et al., 1993) (Figure 4). This appears consistent with geochemical models suggesting that MORB are derived from mixtures of small- and large-degree melts extracted from different mantle depths (Iwamori, 1994; Jull et al., 2002; Kelemen et al., 1997; Lundstrom, 2000; Sims et al., 2003; Sims et al., 2002; Waters et al., 2011) at all spreading rates. In such a model, Gakkel Ridge basalts represent the shallow-sourced mixing end member. Alternatively, models by Van Orman et al. (2006) and Saal and Van Orman (2004) have suggested that the effects of differing diffusion rates on U-series nuclides can generate isotopic disequilibria in melts. When considering percolation reactions during melting and melt transport in mantle rocks, calculations by Van Orman et al.

(2006) predict the strongest chemical disequilibrium effects on U-series disequilibria at high solid upwelling rates. This prediction, however, does not agree well with our observations of particularly high (^{226}Ra/^{230}Th) at the Gakkel Ridge, where we envision particularly *slow* mantle upwelling. While shallow crustal processes (e.g., reactions with crustal cumulate rocks; Van Orman et al., 2006) may, in principle, be capable of generating high (^{226}Ra/^{230}Th) ratios in Gakkel MORB owing to the very low concentrations of Ra in plagioclase (Cooper et al., 2003) such a process would require extremely small melt/rock ratios to produce the large (^{226}Ra/^{230}Th) seen in most MORB. Furthermore, due to the limited volume of crust along the Gakkel Ridge, it is unlikely that the consistently high ^{226}Ra excesses observed were generated by extensive melt reaction with crustal cumulates. Finally, we note that while magma chamber crystallization and replenishment processes seem capable of generating major and trace element fractionations (O'Neill and Jenner, 2012), this model has not been applied to U-series isotope systematics.

5.2. Constraints on MORB petrogenesis

The trace element, radiogenic isotope, and U-series data described and discussed above support heterogeneous sources beneath the Arctic ridges. To further quantify these observations, we explore a model of mixing of melts from two different mantle source lithologies (as in e.g., Elkins et al., 2011; Ito and Mahoney, 2005; Kokfelt et al., 2006; Koornneef et al., 2012; Rudge et al., 2013; Shorttle and Maclennan, 2011; Sims et al., 2013a; Stracke and Bourdon, 2009; Waters et al., 2011) in such a manner as to reproduce our Knipovich Ridge, Mohns Ridge, and Eggvin Bank U-series data. We test a series of one-dimensional melt models that consider depth of melting and/or source heterogeneity, and also incorporate the effects of time-dependent melting on ^{238}U-^{230}Th and ^{235}U-^{231}Pa disequilibria (Bourdon et al., 1996b; Jull et al., 2002; Kelemen et

al., 1997; Lundstrom, 2000; Lundstrom, 2003; Lundstrom et al., 1998b; McKenzie, 1985; Sims et al., 1999; Sims et al., 2002; Spiegelman and Elliott, 1993; Tepley et al., 2004).

We consider a two-lithology scenario where one major garnet-bearing source is a mafic lithology such as eclogite (60% clinopyroxene and 40% garnet) (after e.g., Pertermann et al., 2004) or a more silica-poor garnet pyroxenite (70% clinopyroxene and 30% garnet), a lithologic variation that some have suggested to be a plausible melting mantle lithology (e.g., Hirschmann et al., 2003; Kogiso et al., 2004). Such pyroxenites may result from the impregnation and freezing of a peridotitic matrix with eclogitic source melts. We calculate the melts produced by these mafic lithologies by assuming a relatively trace element-enriched mafic source similar to "EM-2" mantle (($^{238}U/^{232}Th$) = 0.6) (Sims and Hart, 2006), which represents a particularly trace element-enriched mantle source component for U/Th ratios (i.e., low U/Th values) and thus produces an especially broad range of mantle melt compositions.

As in Section 5.1, we also consider a peridotite column originating in the garnet stability field (using a garnet peridotite comprising 12% garnet, 8% clinopyroxene, 59% olivine, and 21% orthopyroxene, with a 100 km peridotite solidus depth) that is trace element-depleted and resembles "DMM" (($^{238}U/^{232}Th$) = 1.6) (Sims and Hart, 2006). While 12% is a relatively high garnet content for peridotites (Walter et al., 2000), owing to the strong garnet control on ^{238}U-^{230}Th disequilibria, we consider a garnet-rich, fertile peridotite to be a useful test for how well, at best, peridotitic melting may explain observed trends. Mafic lithologies have deeper solidi and narrower melting intervals than peridotite, with eclogitic and pyroxenitic solidi respectively 50 km and 6.5 km deeper than the peridotite solidus (i.e. respective solidi at 150 km and 106.5 km), after calculations of Elkins et al. (2008) (Hirschmann and Stolper, 1996; Kogiso et al., 2004; Pertermann and Hirschmann, 2003b). We calculate the compositions of melts from both mafic

and peridotitic lithologies for a range of melting conditions, after which we consider possible mixtures of those melts.

We determine compositions for continuous dynamic melts for our posited peridotite, eclogite, and pyroxenite sources using the formulations of Zou (2000) and assuming constant melt productivities (mineral modes and mineral-melt partition coefficients are shown in Table 4). We test a broad range of maximum residual melt porosities (0.1% to 1%) and melting rates (5 x 10^{-5} to 1 x 10^{-3} kg/m^3/a), which, for constant melting rates and a total melt fraction of 20% in a 100 km melt column, would correspond to solid upwelling rates of 0.75 to 15 cm/a.

The final aggregated dynamic melt compositions extracted from the tops of eclogite, pyroxenite, and peridotite columns are shown in Figure 6. Each curve in the grids shown represents a series of melting outcomes extracted from the top of the melt column, for either a constant porosity and series of melting rates, or constant melt rate and series of different porosities. Melts produced by dynamic melting of both peridotite and the mafic lithologies can readily generate the high (^{230}Th/^{238}U) observed in Arctic basalts for a broad range of possible maximum residual porosities and melting rates (Figure 6). A variety of binary mixing scenarios between the various melts produced by the models have sufficiently high (^{230}Th/^{238}U) ratios to likewise reproduce the range of Knipovich Ridge basalt compositions, as long as one source is relatively enriched in trace elements (i.e. low U/Th ratio) and the other is relatively depleted (i.e. high U/Th ratio; Figure 6). For the initial source U/Th ratios used, it is thus relatively straightforward to produce (^{230}Th/^{232}Th) and (^{238}U/^{232}Th) ratios in melts that readily mix in ways resembling the sloped data arrays observed above (Figure 3). We expect that other melting and mixing models could produce similar trajectories (e.g., mixing melts of relatively trace element-depleted (high U/Th) and -enriched (low U/Th) garnet peridotite sources, with no mafic lithology

present). However, source heterogeneity is in keeping with previous suggestions for a heterogeneous mantle underlying the Mohns and Knipovich Ridges (Andres et al., 2004; Blichert-Toft et al., 2005; Haase et al., 1996; Mertz and Haase, 1997; Schilling et al., 1999; Trønnes et al., 1999) as well as the evidence presented above, i.e. the high (^{230}Th/^{238}U) observed for relatively deep ridge axes (Figure 5), the sloped Knipovich Ridge data array on an equiline diagram, and the low (^{231}Pa/^{235}U) ratios of Eggvin Bank, Mohns, and Knipovich MORB (e.g. Elkins et al., 2011).

In support of the above observations (see Section 5.1.), Figure 6 illustrates that lithology likely plays an important role in producing measured disequilibria, particularly for (^{231}Pa/^{235}U) ratios. Modeled eclogite melt compositions are best able to reproduce the low ^{231}Pa excesses we measured in samples from the Mohns and Knipovich Ridges, as well as neighboring Eggvin Bank samples (Elkins et al., 2011). Because of its short half-life (32.5 ka), ^{231}Pa is more sensitive than ^{230}Th to differences in melting rate caused by the presence of dramatically more fertile mantle lithologies (e.g. eclogite). The faster melting of eclogite substantially reduces the ingrowth of the short-lived daughter isotope during melting, resulting in anomalously low (^{231}Pa/^{235}U) for a given (^{230}Th/^{238}U) in modeled outcomes (Figure 6; Elkins et al., 2011). This sensitivity of ^{235}U-^{231}Pa to increased melting rates in the presence of secondary mantle lithologies makes the ^{235}U-^{231}Pa system a useful tool for fingerprinting eclogite. We note that eclogite melt modeling produces lower (^{231}Pa/^{235}U) for a given (^{230}Th/^{238}U) than pyroxenite; because eclogite is more fusible than pyroxenite, this outcome is consistent with our interpretation that the overall increased melt productivity and, thus, melting rate of a given lithology, is the strongest predictor of ^{235}U-^{231}Pa disequilibria in MORB. We note that it may also be possible to generate high (^{230}Th/^{238}U) and low (^{231}Pa/^{235}U) values similar to those for

Mohns and Knipovich MORB using a two-porosity peridotite melting model after Jull et al. (2002), as long as a high proportion of the final melt mixture is contributed from high porosity channels. However, this is inconsistent with the radiogenic isotope variations for the Mohns and Knipovich Ridges, which predict a heterogeneous source.

Because of the large number of modeled melt mixtures that can reasonably explain the data in Figure 6, and the uncertainty in experimental partition coefficients (e.g. Elkins et al., 2008; Elkins et al., 2011; Sims et al., 1999; Stracke et al., 2006), it is only possible to place broad constraints on the quantity of eclogite in the melt sources underlying these ridges using U-series disequilibria. In Figure 7a, we show two possible mixtures using one of our calculated eclogitic melt outcomes (for a high melting rate of 1 x 10^{-3} kg/m^3/s and a maximum residual melt porosity of 0.5%) and two different peridotitic melts (with a melting rate of 5 x 10^{-5} kg/m^3/s and porosities of 0.1% and 0.5%, respectively). Allowing for the experimental and model uncertainties mentioned above, we observe that the low (^{231}Pa/^{235}U) basalts from the Mohns and Knipovich Ridges require very high contributions of melt from an eclogite source. For both melt mixtures presented, greater than 90% eclogitic melt is required to produce the observed ^{235}U-^{231}Pa systematics. Because eclogite has a considerably deeper onset of melting than peridotite and higher incompatible element contents (Hirschmann and Stolper, 1996; Kogiso et al., 2004; Pertermann and Hirschmann, 2003b), this constraint does not imply a mantle source containing 90% eclogite rock. Ophiolite, abyssal peridotite, alpine massif, and mantle xenolith evidence for the abundance of mantle eclogites and pyroxenites have long suggested that a large, purely eclogitic mantle is implausible (e.g. Bailey et al., 1992; Dick et al., 1984; Frey, 1980; Nixon, 1987; Pearson et al., 1988; Suen and Frey, 1987; Wilshire et al., 1988), making such a conclusion problematic. Rather, for relatively low melt fractions, eclogite melting has a

particularly strong influence on bulk melt composition due to its deeper solidus and higher melt productivity (e.g. Hirschmann and Stolper, 1996). The interpretation that the Knipovich Ridge is underlain by a thick lithospheric cap (Hellevang and Pedersen, 2005), and the fact that such a cap could be reasonably predicted to exist beneath both the Knipovich and Mohns Ridges due to their effectively ultraslow spreading rates (Montesi and Behn, 2007) (i.e., due to the obliquity of their ridge axes) would further increase the proportion of eclogite melt in a binary melt mixture, as discussed above.

The total melt fraction of the source is, however, likewise poorly constrained, since previous calculations using major element compositions (Schilling et al., 1999) infer a purely peridotitic mantle control on the major element composition of the magma. We thus consider the axial ridge depth to be a better indicator of overall melt fraction for the Mohns and Knipovich Ridges; the axial depth to (^{230}Th/^{238}U) relationship presented in Figure 5 implies a total melt fraction of ~17% for the Mohns and Knipovich Ridges. For a constant melting rate of 1 x 10^{-4} kg/m^3/s, a local passive solid upwelling rate of 0.8 cm/a, and a total degree of melting of 17%, a melt column initiating 20 km below the peridotite solidus would have to contain 50% eclogite to generate this much crust, while a melt column only 10 km below the peridotite solidus only requires 25% eclogite in the source. These values are very high, but may be reasonable for a mantle source region widely inferred to contain unusually high quantities of mafic rocks (Blichert-Toft et al., 2005; Debaille et al., 2009; Haase et al., 1996; Haase et al., 2003; Mertz et al., 2004).

While we consider a 0.1% porosity melt, as modeled above, mechanistically unlikely to be efficiently extracted from the melt source, we present those mixing results in Figure 7a to further demonstrate that as residual melt porosity shrinks, MORB from the neighboring

Kolbeinsey Ridge can tolerate progressively higher proportions of eclogite-derived melt in the melt mixture. Due to this broad range of possible solutions, it is even more difficult to uniquely fingerprint the quantity of eclogite in the neighboring Kolbeinsey Ridge melt source: the two mixing models shown indicate a possible range of 0-80% eclogitic melt contributions to the mixture (Figure 7a). Thus, based on the overall higher (^{231}Pa/^{235}U) ratios measured for Kolbeinsey Ridge basalts and the above modeling, we infer that the Kolbeinsey MORB source likely contains substantially less eclogite than the source for Mohns and Knipovich Ridge basalts.

The quantity of eclogite in the melt source region beneath these ridges cannot presently be more precisely constrained from U-series isotopes because the degree of U-series disequilibria in melt mixtures depends so heavily on the exact melt productivity of eclogite below the peridotite solidus and the depth difference of the two solidi, both of which are relatively poorly constrained by experimental results (e.g., Hirschmann and Stolper, 1996; Kogiso et al., 2004; Pertermann and Hirschmann, 2003b). Because trace element concentrations in mantle eclogites and pyroxenites likewise are poorly constrained, previous work has shown that it is equally difficult to uniquely determine the abundance of eclogite in a mantle source using only trace element data in MORB (e.g., Hirschmann and Stolper, 1996). Radiogenic isotopes should provide additional constraints for melt contributions from long-lived enriched mantle sources. We show additional calculated melt mixtures in Figure 7b, using ε_{Nd} values as indicators of mantle source heterogeneity vs. (^{238}U/^{232}Th), which is directly proportional to the U/Th trace element ratio, making it a useful indicator of trace element enrichment in the source. We calculate dynamic melt compositions for peridotite and eclogite sources after Zou and Zindler (2002) and Zou et al. (1998), using the same melting parameters as in the 0.5% porosity

peridotite-eclogite mixture shown in Figure 7a, trace element partition coefficients from Table 4, and initial Nd source concentrations for the peridotitic DMM and eclogitic EM2 source rocks as in Workman et al. (2004; 2005). We used initial U concentrations of 0.0018 for DMM and 0.04 for EM2, and initial source ($^{238}U/^{232}Th$) values of 1.9 and 5.3, respectively (Sims and Hart, 2006). Most significantly, the curvature of the mixing trajectory closely parallels the compositions of Arctic MORB. The calculated binary mixing trajectory is, however, offset to higher ε_{Nd} and lower ($^{238}U/^{232}Th$) values than the measured Arctic data (this study; Elkins et al., 2011), suggesting local mantle source components that are less extreme than the most depleted DMM and most enriched EM2 global mantle reservoirs. While a number of different end member components can generate the observed data, one alternative is shown for a less depleted peridotite source and corresponding melt (ε_{Nd} lowered to +10) and a less enriched eclogite melt (($^{238}U/^{232}Th$) = 0.75), which only requires a more conservative 20% contribution of eclogite melt to the binary mixture in order to generate the most trace element and isotopically enriched Mohns and Knipovich Ridge magmas.

For the reasons expressed above that both spreading rate and isotopic evidence for source heterogeneity vary concurrently in the Arctic, and taking into account the effects of uncertainties in published experimental partition coefficient values (e.g. Elkins et al., 2011) and the relatively poor constraints on melt productivity and solidus depth of eclogite rocks (e.g., Hirschmann and Stolper, 1996; Kogiso et al., 2004; Pertermann and Hirschmann, 2003b), it is not possible to further uniquely constrain melting conditions such as upwelling rate, maximum porosity, or the precise nature of lithologic heterogeneity along-axis. We propose that the presence of additional eclogite in the mantle source region, coupled with slow upwelling and regionally cooler mantle creating a relatively shallow solidus with an overlying lithospheric cap, broadly explains the

geochemical indicators of heterogeneity, the low melt fraction inferred from major element geochemistry, and the deep ridge axes and thin crust measured on the Mohns and Knipovich Ridges.

6. CONCLUSIONS

Our slow- and ultraslow-spreading ridge data support a model in which global MORB ($^{230}Th/^{238}U$) is partly controlled by mantle temperature, with additional influence from 1) overlying lithospheric truncation of mantle melting due to regionally slow spreading rates, and 2) contributions from eclogitic mantle source components. As postulated by Bourdon et al. (1996b) and others (e.g. Langmuir et al., 1992; Niu and Batiza, 1993, 1997; Niu et al., 2001; Russo et al., 2009), we suggest that the full range of global ($^{230}Th/^{238}U$) is additionally affected by local and regional variations in factors including mixing of melts from different depths, efficiency of melt extraction, melt-rock reaction, solid upwelling rate, and residual melt porosity.

In particular, Eggvin Bank, Mohns, and Knipovich MORB are more isotopically enriched than either EVZ Gakkel Ridge basalts or the nearby Kolbeinsey Ridge south of 70.7ºN, indicating the presence of highly heterogeneous source material under those ridges. Knipovich Ridge basalts span a broad range of ($^{238}U/^{232}Th$) that correlates with radiogenic isotopic composition (e.g. $^{87}Sr/^{86}Sr$), indicating that these MORB are influenced by source heterogeneity. This is in keeping with the postulated presence of a combination of trapped subcontinental lithospheric material in the subsurface beneath the Mohns and Knipovich Ridges (Andres et al., 2004; Blichert-Toft et al., 2005) and locally emplaced mantle eclogite (e.g., Debaille et al., 2009; Schilling et al., 1999). High ($^{230}Th/^{238}U$) for relatively deep ridge axes and low ($^{231}Pa/^{235}U$) in

Mohns and Knipovich MORB support and corroborate the presence of eclogite in the mantle source, although it is difficult to constrain the exact quantity.

A remarkable feature of the present data set is the observation that basalts from 85ºE on the Gakkel Ridge are homogeneous with (^{230}Th/^{238}U) close to unity, ranging from 5% ^{230}Th excess to 5% ^{238}U excess, with very large minimum (^{226}Ra/^{230}Th) ratios (> 3.0). These samples lie at the extreme high (^{226}Ra/^{230}Th) end of the negative global correlation between (^{226}Ra/^{230}Th) and (^{230}Th/^{238}U), supporting a scenario in which MORB are the products of mixing of melts extracted from different depths during upwelling (Jull et al., 2002; Kelemen et al., 1997; Sims et al., 1995; Sims et al., 2002). In this scenario, Gakkel MORB represent the end member product of a short melt column with shallow melt-rock reaction and subsequent melt segregation. This additional cooling produces a thick lithospheric cap at ultraslow-spreading and upwelling rates and thus contributes to the particularly thin crust observed on the Gakkel Ridge.

Acknowledgments. This work benefited from valuable feedback and conversations from a number of colleagues, including Peter Kelemen, Fred Frey, and Marc Speigelman, as well as helpful and constructive suggestions from three anonymous reviewers. George Cherkashev supplied samples for this research from the Knipovich Ridge. This research was funded by the National Science Foundation grants OCE-0422278 to K.W.W.S. and OCE-1061037/1060434 to L.J.E. and K.W.W.S. J.B.T. acknowledges financial support from the French Agence Nationale de la Recherche (grant ANR-10-BLANC-0603 M&Ms – Mantle Melting – Measurements, Models, Mechanisms).

APPENDIX A: THE ARCTIC MID-OCEAN RIDGE SYSTEM

The Arctic oceanic basins are relatively young in age. Rifting between Greenland and Eurasia initiated at 53-55 Ma, forming the Aegir, Jan Mayen, Mohns, and Gakkel Ridges (Blichert-Toft et al., 2005; Glebovsky et al., 2006; Schilling et al., 1999; Shipilov, 2008). At 45 Ma, a north-propagating rift axis initiated to the west of the Jan Mayen Ridge; the northern propagation of this early Kolbeinsey Ridge isolated and trapped the ridge and the ensuing ridge jump was complete by 26 Ma. The spreading direction along the Mohns Ridge changed from NNW-SSE to NW-SE at 25 Ma (Mjelde et al., 2008a). This may have coincided with initiation of spreading along the transform between the Mohns and Gakkel Ridges, producing what is now the highly oblique Knipovich Ridge (Okino et al., 2002) (Figure 1).

Kolbeinsey Ridge, Eggvin Bank, Jan Mayen Fracture Zone

For comparison with the present work, we here note key information about the most southerly ridge in the Arctic MOR, the Kolbeinsey Ridge (Figure 1). Crustal thickness averages 7-10 km and may reach 15 km (Kodaira et al., 1997; Mjelde et al., 2008b) due to hotter mantle temperatures and enhanced melt production because of the proximity to Iceland. Spreading is nearly orthogonal to the ridge axis (full spreading rate is ~18 mm/a; Breivik et al., 2006; Mosar et al., 2002) and the ridge is volcanically active along its length. With the exception of more enriched compositions in the extreme south immediately adjacent to Iceland, southern Kolbeinsey MORB broadly reflect a relatively homogeneous, trace element-depleted (where "depleted" refers to long-term incompatible element depletion as manifested through less radiogenic $^{87}Sr/^{86}Sr$, $^{206}Pb/^{204}Pb$, $^{207}Pb/^{204}Pb$, and $^{208}Pb/^{204}Pb$ and high ε_{Nd} and ε_{Hf}), garnet-bearing, young, deep mantle source (Andres et al., 2004; Blichert-Toft et al., 2005; Devey et al., 1994; Elkins et al., 2011; Hanan et al., 2000; Mertz et al., 1991; Mertz and Haase, 1997; Salters,

1996; Schilling et al., 1999; Schilling et al., 1983; Waggoner, 1989) (Figure 2). Ancient trace element-enriched material containing eclogite or pyroxenite contributes melts to the Northern Kolbeinsey Ridge segment immediately south of the Jan Mayen Fracture Zone, which includes the anomalously shallow Eggvin Bank area (Blichert-Toft et al., 2005; Debaille et al., 2009; Devey et al., 1994; Elkins et al., 2011; Haase et al., 2003; Hanan et al., 2000; Mertz et al., 1991; Mertz et al., 2004; Schilling et al., 1999; Schilling et al., 1983; Trønnes et al., 1999) (Figure 2).

The Jan Mayen Fracture Zone bounds the Kolbeinsey Ridge to the south and the Mohns Ridge to the north and is adjacent to the volcanic Jan Mayen Island (Haase et al., 1996; Schilling et al., 1999; Trønnes et al., 1999). Jan Mayen-related magma production likely influences MORB composition on both adjacent ridge segments, producing basalts with enriched radiogenic isotope ratios (e.g. high $^{87}Sr/^{86}Sr$) and trace element ratios (e.g. high La/Yb_N) (Schilling et al., 1999).

Mohns Ridge

The Mohns Ridge (17 mm/a spreading rate; Mosar et al., 2002) is located immediately north of the Jan Mayen Fracture Zone and has an estimated crustal thickness of 4 to 8 km along a mostly continuous single ridge segment (Klingelhofer et al., 2000). Spreading direction (NW-SE) is oblique to the ridge axis orientation.

Basalts from the Mohns Ridge show variable isotopic and trace element signatures, but are generally more enriched than the Kolbeinsey Ridge (e.g. La/Yb_N = 0.6–5.6; $^{87}Sr/^{86}Sr$ = 0.70284–0.70321; ε_{Nd} = +7.2–+9.6; ε_{Hf} = +10–+24) (Blichert-Toft et al., 2005; Devey et al., 1994; Elkins et al., 2011; Haase et al., 1996; Haase et al., 2003; Hanan et al., 2000; Mertz et al., 1991; Mertz and Haase, 1997; Mertz et al., 2004; Neumann and Schilling, 1984; Schilling et al., 1999;

Schilling et al., 1983; Trønnes et al., 1999; Waggoner, 1989), suggesting melt input from a relatively trace element-enriched mantle source. Lead isotope ratios in Mohns Ridge basalts resemble a "DUPAL"-type enrichment (Blichert-Toft et al., 2005). Anomalously high ε_{Hf} values relative to ε_{Nd} may indicate the presence of streaks of subcontinental lithospheric material in the underlying mantle (Andres et al., 2004; Blichert-Toft et al., 2005); this is supported by additional geochemical measurements, such as Os isotopes and others (Blichert-Toft et al., 2005; Debaille et al., 2009; Haase et al., 1996; Haase et al., 2003; Hanan et al., 2000; Mertz et al., 2004; Neumann and Schilling, 1984; Schilling et al., 1999; Schilling et al., 1983; Waggoner, 1989) (Figure 2).

Knipovich Ridge

The ultraslow Knipovich Ridge (up to 16 mm/a; Mosar et al., 2002) has an estimated crustal thickness of 3.5-5.5 km (Jokat et al., 2012; Kandilarov et al., 2008; Ljones et al., 2004; Okino et al., 2002; Ritzmann et al., 2002) similar to the Mohns Ridge, but its spreading direction is even more oblique than that of the Mohns Ridge (35 - 49º obliquity; Okino et al., 2002). The ridge structure is highly asymmetric, with some isolated volcanic edifices (Crane et al., 2001). The axis is located in a series of small pull-apart basins along the strike of the ridge that are underlain by small-scale transform structures, and side-scan studies show abundant areas with little or no sediment cover (Okino et al., 2002). Recent magnetic and seismic data suggest the ridge axis is a detachment zone containing faulted ridge segments connected by transform boundaries (Sokolov, 2011; Yampol'skiy and Sokolov, 2012). The petrology of Knipovich Ridge MORB indicates a deep onset of fractional crystallization at 6 to 7 kbar that may indicate a relatively thick lithosphere of 20 km beneath this ridge (Hellevang and Pedersen, 2005).

Unaltered Knipovich MORB are variable in composition but broadly resemble Mohns Ridge basalts in chemical and isotope makeup (Andres et al., 2004; Blichert-Toft et al., 2005; Hanan et al., 2000; Neumann and Schilling, 1984; Schilling et al., 1999; Schilling et al., 1983; Waggoner, 1989) and thus likewise have been hypothesized to contain melts from a relatively trace element-enriched, "DUPAL"-like mantle source bearing streaks or veins of subcontinental lithospheric mantle material (Andres et al., 2004; Blichert-Toft et al., 2005; Debaille et al., 2009; Haase et al., 1996; Haase et al., 2003; Mertz et al., 2004) (Figure 2). Global MORB compilations by Salters et al. (2011) indicate that Knipovich MORB contain the most extreme high ε_{Hf} compositions of any MORB measured to date; they further explain these high ε_{Hf} values by invoking the presence of a lithospheric mantle component that experienced an ancient melt extraction event in the Knipovich Ridge mantle source region.

Gakkel Ridge

Gakkel Ridge crust is likely underlain by cold, thick lithospheric mantle at the ridge axis (Montesi and Behn, 2007) and is extremely thin (≤ 3 km) and amagmatic in many locations, with local thickening beneath isolated active volcanoes (Jokat and Schmidt-Aursch, 2007). The ridge is divided into three regions with distinct morphological and volcanic characteristics: the Western Volcanic Zone (WVZ; ~13 mm/a) with active magmatic centers along its entire length; the Sparsely Magmatic Zone (SMZ), where spreading is mainly occurring amagmatically; and the Eastern Volcanic Zone (EVZ; <12 mm/a), the slowest-spreading mid-ocean ridge segment on Earth, with active volcanism occurring only at discrete volcanic centers (Goldstein et al., 2008; Michael et al., 2003). The Gakkel Ridge connects to the Knipovich Ridge via the Lena Trough, a

dominantly nonvolcanic oceanic-continental transitional rift zone where rifting initiated in the Miocene (Crane et al., 2001; Hellebrand and Snow, 2003; Nauret et al., 2011).

Goldstein et al. (2008) observed that WVZ lavas have a strongly enriched Pb isotope "DUPAL"-type signature that the EVZ MORB lack, suggesting the presence of trapped subcontinental lithospheric mantle remnants from Svalbard-Greenland rifting in the WVZ mantle, although the exact source of those remnants has been contested (Choi et al., 2010; Griffin et al., 2012; Lassiter and Snow, 2009; Nauret et al., 2010). Osmium, Nd, and Hf isotope compositions of Gakkel Ridge and Lena Trough abyssal peridotites indicate a chemically and mineralogically heterogeneous mantle, containing extremely refractory, depleted material and fertile lithospheric veins possibly entrained during early basin formation (Lassiter and Snow, 2009; Liu et al., 2008; Nauret et al., 2010; Nauret et al., 2011; Stracke et al., 2011). Recent geophysical work suggests a heterogeneous uppermost mantle density structure (Urlaub et al., 2009). The uniformly isotopically depleted nature of EVZ lavas reflects melting of a relatively homogeneous, ancient trace element-depleted mantle source underlying the eastern part of the ridge (Goldstein et al., 2008) (Figure 2).

APPENDIX B: ANALYTICAL FACILITIES AND METHODS

Isotopic analyses measured in five different laboratory facilities contributed to this work. Here the techniques used in each facility are provided in further detail. A complete listing of the samples analyzed in each facility is provided in Tables 2 and 3.

Woods Hole Oceanographic Institution

Chemistry:

A suite of analyses comprising U and Th concentrations and (^{230}Th/^{232}Th), (^{234}U/^{238}U), (^{226}Ra/^{230}Th), ^{87}Sr/^{86}Sr, ^{206}Pb/^{204}Pb, ^{207}Pb/^{204}Pb, and ^{208}Pb/^{204}Pb was performed at WHOI. After the hand picking and leaching procedures described in the text, samples were dissolved using high-purity HF-HNO_3-HCl-$HClO_4$ acids. Following dissolution, well-mixed aliquots were weighed and separated for separate analysis. Except where indicated in Table 2, all analyses were performed using separate aliquots from a single sample dissolution.

For U and Th concentration analysis by isotope dilution, a dissolved sample aliquot was spiked with separate ^{233}U and ^{229}Th spike solutions. The sample and spike solutions were heated for 48 hours with concentrated $HClO_4$, dried, and then redissolved and fumed repeatedly to dryness in a HNO_3 + $HClO_4$ solution to ensure full spike-sample equilibration. Uranium and Th were subsequently separated for analysis with anion exchange resin in HNO_3 solution.

A second, unspiked sample aliquot from the same sample dissolution was used for U and Th isotopic composition measurements and, when permitted by sufficient sample quantity (Table 2), for ^{226}Ra concentration analysis. Radium concentrations were measured by isotope dilution using a ^{228}Ra spike, which was precisely weighed and added to the aliquot. The sample-spike mixture was heated for 48 hours, and then dried and repeatedly fumed in a HCl-$HClO_4$ solution. The aliquots were subsequently prepared for mass spectrometric analysis. Thorium and U were initially separated from the silicate matrix using anion exchange resin in HNO_3 solution, and subsequently from each other using anion exchange resin in HCl solution. A radium separate was further purified using a cation exchange resin in HCl, followed by Sr Spec resin in HNO_3 and a final cation exchange column in HCl immediately prior to analysis. Further details regarding these analytical methods are available in Sims et al. (2008b).

Separate aliquots of the dissolved samples were prepared for Sr isotope analysis using anion exchange resin in HCl, after Hart et al. (2004), Hart and Blusztajn (2006), and Sims et al. (2013a). Lead was separated for isotopic analysis using anion exchange resin in HBr-HNO_3 solution, after Abouchami et al. (1999), Hart and Blusztajn (2006). Additional analytical details for Sr, and Pb analyses using the WHOI NEPTUNE are detailed in the supplemental information of Sims et al. (2013a).

Mass Spectrometry:

Following separation and purification procedures, U and Th concentrations were measured by isotope dilution using the Thermo Element2 high-resolution ICP-MS (Sims et al., 2008a; Sims et al., 2008b). U and Th mass bias was corrected using sample-standard bracketing with standard NBL-112A and a linear interpolation. ^{229}Th and ^{233}U spikes were calibrated against the Ames ^{232}Th and the NIST ^{238}U standards (NBS960). Accounting for spike calibration reproducibility (~1%), uncertainty in the concentration of the gravimetric standards (<0.5%), and in-run errors for isotope dilution measurements, the propagated uncertainty on ^{232}Th and ^{238}U concentration measurements, is1-1.5 % (2σ). Previous work (e.g, Sims et al., 2008b; 2013b; Koornneef et al., 2010) has demonstrated interlaboratory reproducibilities for rock standards of <2 % for U and Th concentration measurements using isotope dilution mass spectrometry techniques.

Uranium and Th isotope ratios were measured using the ThermoFisher Neptune MC-ICP-MS instrument at WHOI. For U isotope analysis, mass bias and SEM yields were calibrated during analytical runs using sample-standard bracketing with U010 (^{238}U/^{236}U = 14,535 ± 149; Sims et al., 2008b; and ^{234}U/^{238}U = 5.4484 x 10^{-5}; Richter et al., 2006). Mass bias was corrected

with a linear interpolation, followed by a second standard correction using U960 ($^{234}U/^{238}U$ = 5.286 x 10^{-5}; Richter et al., 2006).

($^{230}Th/^{232}Th$) ratios were measured using sample-standard bracketing with UCSC Th 'A' ($^{230}Th/^{232}Th = 5.856 \pm 0.070 \times 10^{-6}$; Rubin, 2001), which corrects for drift of 0.5-1.0 % (Sims et al., 2008b). ^{230}Th peak intensities were corrected for the tail of the ^{232}Th peak using an exponential tailing correction, which is in turn ratioed to a theoretical ratio to correct for mass bias and SEM efficiency (Ball et al., 2008). Uncertainties for rock standard analyses using this technique range from 0.4-0.9% (2σ, Ball et al., 2008).

^{226}Ra concentrations were measured with the Thermofisher Neptune MC-ICP-MS, using a peak hopping routine on the SEM with an RPQ to measure $^{226}Ra/^{228}Ra$ (Sims et al., 2008b). The ^{228}Ra spike used at WHOI was calibrated using NIST4967 as the ^{226}Ra standard, which has a 1.18% 2σ uncertainty. Mass bias corrections were conducted with U isotopes from standard NBL-112a, and background levels on the SEM detector were corrected using a peak-hopping routine. When analytical precision is propagated with the NIST4967 spike calibration standard uncertainty of 1.2%, a conservative error analysis limits our knowledge of ($^{226}Ra/^{230}Th$) to less than or equal to 3%.

$^{87}Sr/^{86}Sr$ sample ratios were normalized for instrumental mass fractionation using $^{86}Sr/^{88}Sr = 0.1194$ and corrected with standard SRM987 ($^{87}Sr/^{86}Sr = 0.7102140$). Lead isotope compositions were normalized for instrumental mass bias relative to $^{205}Tl/^{203}Tl = 2.38709$ for SRM997 Tl standard, and then corrected using standard SRM981 with values from Todt et al. (1996). Lead isotopes at WHOI have reported internal precisions of 15 to 30 ppm for $^{206}Pb/^{204}Pb$, $^{207}Pb/^{204}Pb$, and $^{208}Pb/^{204}Pb$ (Hart and Blusztajn, 2006) and external reproducibilities from 17 ppm for $^{207}Pb/^{204}Pb$ to 117 ppm for $^{208}Pb/^{204}Pb$.

University of Bristol

Chemistry:

Uranium and Th concentrations, (^{230}Th/^{232}Th), (^{234}U/^{238}U), and (^{231}Pa/^{235}U) were analyzed for handpicked, leached glass chips (see text) using the Bristol Isotope Group facilities housed at the University of Bristol. Except for those analyses listed as separate dissolutions in Table 2, all analyses were conducted using a single dissolution. Both a mixed ^{236}U-^{229}Th spike and ^{233}Pa spike were weighed and added to each sample prior to HF-HNO_3-HCl-$HClO_4$-boric acid dissolution (after Regelous et al., 2004). During digestion samples were fumed to dryness in $HClO_4$, followed by repeated drying and redissolution in HNO_3 and then HCl to ensure full spike-sample equilibration. Uranium, Th, and Pa were separated using TruSpec (Eichrom) resin. Protactinium was further isolated using AG1-X8 anion exchange resin, followed by a TruSpec column to purify the Pa separate prior to mass spectrometric analysis (chemical separation procedure fully detailed in Regelous et al., 2004).

Mass spectrometry:

Uranium and Th concentrations were measured by MC-ICP-MS (Thermo Fisher NEPTUNE) at the University of Bristol (Hoffmann et al., 2007; Prytulak et al., 2008; Regelous et al., 2004; Sims et al., 2008b). Thorium isotope ratios were measured with sample-standard bracketing using the in-house Th TEDDi standard to correct for mass bias and yield (Hoffmann et al., 2007). Uranium mass bias and SEM yield corrections were made using standard-sample bracketing with U standard NBL-112a (^{235}U/^{238}U = 0.0072526, ^{234}U/^{238}U = 5.54887 x 10^{-5}; Hoffmann et al., 2007). Uranium standard NBL-112a was added to Pa solutions just prior to

analysis to correct for mass bias during Pa isotope analysis by static faraday measurement of ^{238}U and ^{235}U. Internal reproducibilities of $^{233}Pa/^{231}Pa$ were 0.5% (2σ) and external accuracy of ($^{231}Pa/^{235}U$) is 1.3% (2σ) (Prytulak et al., 2008).

Kiel University

Chemistry:

A suite of U and Th concentrations, ($^{230}Th/^{232}Th$), $^{87}Sr/^{86}Sr$, $^{143}Nd/^{144}Nd$, $^{206}Pb/^{204}Pb$, $^{207}Pb/^{204}Pb$, and $^{208}Pb/^{204}Pb$ were analyzed at Kiel University. Handpicked glass chips were spiked with 229Th and 236U prior to HF-HNO_3-HCl digestion. Further treatment with HCl and H_3BO_3 was used to ensure sample-spike equilibration. Prior to analysis by mass spectrometry, Th and U were separated using anion exchange resin with HNO_3 and HCl (Fretzdorff et al., 2003).

Mass spectrometry:

Uranium and Th concentrations were measured by ICP-MS (Micromass PlasmaTrace 2) at Kiel University (Fretzdorff et al., 2003). Analytical methods at Kiel University report 0.25 % (2σ) uncertainty for ($^{230}Th/^{232}Th$) measurements, with procedural U and Th blanks of 50 and 55 pg, respectively. Mass spectrometry data at Kiel were obtained using a linear correction for analytical bias, and internal laboratory results have shown good agreement within 2σ uncertainty for the rock standards RML, JB-1, and AGV-1 (Fretzdorff et al., 2003).

$^{87}Sr/^{86}Sr$ values were corrected for mass fractionation relative to $^{86}Sr/^{88}Sr = 0.1194$ and normalized to a NBS 987 $^{87}Sr/^{86}Sr$ value of 0.71025 (Haase et al., 2004). Internal measurements had reproducibilities of 0.000024 (2σ) and produced a mean standard NBS 987 value of $^{87}Sr/^{86}Sr$

= 0.710218 (Haase et al., 2004). Neodymium isotopes were corrected for mass fractionation relative to $^{146}Nd/^{144}Nd = 0.7219$. The La Jolla standard gave an internal precision of 0.000007 (2σ) for a value of 0.511827 for $^{143}Nd/^{144}Nd$. The normalizing value used for the La Jolla standard was 0.511855 (Haase et al., 2004). Lead isotope analyses were corrected using NBS 981 with values from Todt et al. (1996), producing 2σ analytical precisions of < 1 per mil.

University of Iowa

Chemistry and alpha counting:

Activities of ^{210}Pb were determined for three samples by alpha counting of its descendent (^{210}Po) at the University of Iowa and assuming secular equilibrium (($^{210}Po/^{210}Pb$) = 1). Fine-grained, whole-rock sample material was leached using the procedure described in the main text. Samples were then spiked with a ^{209}Po solution calibrated against TML ((^{210}Po) = 7.95 dpm/g; Reagan et al., 2005) and tested frequently against USGS rock standards BCR-2 and RGM-2 to monitor spike calibration. Samples were then digested in HF and HNO_3, dried, and dissolved in 1 N HCl. Complete dissolution was assured by centrifuging sample solutions. Polonium was separated prior to analysis using anion exchange resin, after which Po was autoplated on Ag in warm 0.5 N HCl in preparation for alpha counting on an EGG Ortec alpha spectrometry system. Alpha counts were corrected for blank measurements, background (0.0002 to 0.002 dpm), and a small tail from the adjacent ^{209}Po peak. ^{210}Pb activity was determined Methods are described in further detail in Reagan et al. (2005), Reagan et al. (2006), and Waters et al. (2013).

Ecole Normale Supérieure de Lyon

Chemistry:

$^{143}Nd/^{144}Nd$ and $^{176}Hf/^{177}Hf$ were analyzed at the Ecole Normale Supérieure in Lyon using methods detailed in Blichert-Toft et al. (1997), Blichert-Toft (2001), and Blichert-Toft and Albarède (2009). Samples were leached for 30 minutes in hot 6M HCl prior to weighing and HF-HNO_3 digestion. Hafnium was initially separated from Nd through precipitation of a Ca-Mg-fluoride rare-earth bearing precipitate using HF. The Hf fraction in the resulting supernatant was further purified for mass spectrometry using anion-exchange resin with HF-HCl, followed by a final cation-exchange column with HCl-H_2O_2, which was preceded by $HClO_4$ fuming of the fraction collected from the anion-exchange column to remove all fluorides. Neodymium was extracted and purified for mass spectrometry from the Ca-Mg fluoride precipitate left after the HF leaching mentioned above using cation-exchange resin with HCl followed by purification on HDEHP columns using HCl. Further chemistry procedure details are available from Blichert-Toft et al. (1997), Blichert-Toft (2001), and Blichert-Toft and Albarede (2009).

Mass spectrometry:

Hafnium isotope compositions are reported relative to the Hf standard JMC-475 ($^{176}Hf/^{177}Hf = 0.282163 \pm 0.000009$; Blichert-Toft et al., 1997) using $^{179}Hf/^{177}Hf$ of 0.7325 and an exponential law to correct for instrumental mass bias. External reproducibility using this method is 30 ppm, with internal precisions of 10-15 ppm for MORB (Blichert-Toft, 2001; Blichert-Toft et al., 1997). Neodymium isotope compositions are reported relative to the in-house "Rennes" standard ($^{143}Nd/^{144}Nd = 0.511961 \pm 0.000013$; Chauvel and Blichert-Toft, 2001), with external reproducibility of 30 ppm and internal run precisions between 10-15 ppm. Ratios were normalized for instrumental mass bias relative to a value of 0.7219 for $^{146}Nd/^{144}Nd$ using an exponential law.

REFERENCES

Abouchami, W., Galer, S.J.G., and Koschinsky, A., (1999). Pb and Nd isotopes in NE Atlantic Fe–Mn crusts: proxies for trace metal paleosources and paleocean circulation. *Geochim. Cosmochim. Acta* **63**, 1489–1505.

Andres, M., Blichert-Toft, J., and Schilling, J.-G., 2004. Nature of the depleted upper mantle beneath the Atlantic: evidence from Hf isotopes in normal mid-ocean ridge basalts from 79°N to 55°S. Earth Planet. Sci. Lett. **225**, 89-103.

Asimow, P.D., Hirschmann, M.M., Stolper, E.M. (2001) Calculation of peridotite partial melting from thermodynamic models of minerals and melts. IV. Adiabatic decompression and the composition and mean properties of mid-ocean ridge basalts. *Journal of Petrology* **42,** 963-998.

Aumento, F. (1971) Uranium Content of Mid-Ocean Ridge Basalts. *Earth Planet Sci. Lett.* **11,** 90-94.

Bacon, M.P. (1978) Radioactive Disequilibrium in Altered Mid-Oceanic Basalts. *Earth Planet Sci. Lett.* **39,** 250-254.

Bailey, J.C., Campsie, J., Hald, N., Dittmer, F., Fine, S., Rasmussen, M. (1992) Petrology and Geochemistry of a Dredged Clinopyroxenite Dolerite Basal Complex from the Jan Mayen Volcanic Province, Norwegian Greenland Sea. *Mar. Geol.* **105,** 63-76.

Ball, L., Sims, K.W.W., Schwieters, J. (2008) Measurement of U-234/U-238 and Th-230/Th-232 in volcanic rocks using the Neptune MC-ICP-MS. *Journal of Analytical Atomic Spectrometry* **23,** 173-180.

Beattie, P. (1993a) The Generation of Uranium Series Disequilibria by Partial Melting of Spinel Peridotite - Constraints from Partitioning Studies. *Earth Planet Sci. Lett.* **117,** 379-391.

Beattie, P. (1993b) Uranium Thorium Disequilibria and Partitioning on Melting of Garnet Peridotite. *Nature* **363,** 63-65.

Blichert-Toft, J. (2001) On the Lu-Hf isotope geochemistry of silicate rocks. *Geostandards Newsletter-the Journal of Geostandards and Geoanalysis* **25,** 41-56.

Blichert-Toft, J., Albarède, F. (2009) Mixing of isotopic heterogeneities in the Mauna Kea plume conduit. *Earth Planet. Sci. Lett.* **282**, 190-200.

Blichert-Toft, J., Chauvel, C., Albarède, F. (1997) Separation of Hf and Lu for high-precision isotope analysis of rock samples by magnetic sector-multiple collector ICP-MS. *Contrib. Mineral. Petr.* **127,** 248-260.

Blichert-Toft, J., Agranier, A., Andres, M., Kingsley, R., Schilling, J.G., Albarede, F. (2005) Geochemical segmentation of the Mid-Atlantic Ridge north of Iceland and ridge-hot spot interaction in the North Atlantic. *Geochem. Geophys. Geosys.* **6,** 2004GC000788.

Blundy, J.D., Wood, B.J. (2003) Mineral-melt partitioning of uranium, thorium, and their daughters, *Reviews in Mineralogy* **52**, pp. 59-123.

Bourdon, B., Langmuir, C.H., Zindler, A. (1996a) Ridge-hotspot interaction along the Mid-Atlantic Ridge between 37 degrees 30' and 40 degrees 30'N: The U-Th disequilibrium evidence. *Earth Planet Sci. Lett.* **142,** 175-189.

Bourdon, B., Zindler, A., Elliott, T., Langmuir, C.H. (1996b) Constraints on mantle melting at mid-ocean ridges from global U-238-Th-230 disequilibrium data. *Nature* **384,** 231-235.

Bourdon, B., Joron, J.L., Claude-Ivanaj, C., Allegre, C.J. (1998) U-Th-Pa-Ra systematics for the Grande Comore volcanics: melting processes in an upwelling plume. *Earth Planet Sci. Lett.* **164,** 119-133.

Bourdon, B., Goldstein, S.J., Bourles, D., Murrell, M.T., Langmuir, C.H. (2000) Evidence from ^{10}Be and U series disequilibria on the possible contamination of mid-ocean ridge basalt glasses by sedimentary material. *Geochem. Geophys. Geosys.* **1,** 2000GC000047.

Bourdon, B., Turner, S.P., Ribe, N.M. (2005) Partial melting and upwelling rates beneath the Azores from a U-series isotope perspective. *Earth Planet Sci. Lett.* **239,** 42-56.

Breivik, A.J., Mjelde, R., Faleide, J.I., Murai, Y. (2006) Rates of continental breakup magmatism and seafloor spreading in the Norway Basin-Iceland plume interaction. *J. Geophys. Res.-Sol. Ea.* **111,** 2005JB004004.

Chauvel, C., Blichert-Toft, J. (2001) A hafnium isotope and trace element perspective on melting of the depleted mantle. *Earth Planet. Sci. Lett.* **190,** 137-151.

Cheng, H., Edwards, R.L., Hoff, J., Gallup, C.D., Richards, D.A., Asmerom, Y., 2000. The half-lives of uranium-234 and thorium-230. *Chemical Geology* **169,** 17-33.

Choi, S.H., Suzuki, K., Mukasa, S.B., Lee, J.I., Jung, H. (2010) Lu-Hf and Re-Os systematics of peridotite xenoliths from Spitsbergen, western Svalbard: Implications for mantle-crust coupling. *Earth Planet. Sci. Lett.* **297,** 121-132.

Claude-Ivanaj, C., Bourdon, B., Allegre, C.J. (1998) Ra-Th-Sr isotope systematics in Grande Comore Island: a case study of plume-lithosphere interaction. *Earth Planet. Sci. Lett.* **164,** 99-117.

Claude-Ivanaj, C., Joron, J.L., Allegre, C.J. (2001) U-238-Th-230-Ra-226 fractionation in historical lavas from the Azores: long-lived source heterogeneity vs. metasomatism fingerprints. *Chemical Geology* **176,** 295-310.

Coakley, B.J., Cochran, J.R. (1998) Gravity evidence of very thin crust at the Gakkel Ridge (Arctic Ocean). *Earth Planet. Sci. Lett.* **162,** 81-95.

Cohen, R.S., Evensen, N.M., Hamilton, P.J., Onions, R.K. (1980) U-Pb, Sm-Nd and Rb-Sr Systematics of Mid-Ocean Ridge Basalt Glasses. *Nature* **283,** 149-153.

Condomines, M., Morand, P., Allegre, C.J., Sigvaldason, G. (1981) Th-230-U-238 Disequilibria in Historical Lavas from Iceland. *Earth Planet. Sci. Lett.* **55,** 393-406.

Cooper, K.M., Goldstein, S.J., Sims, K.W.W., Murrell, M.T. (2003) Uranium-series chronology of Gorda Ridge volcanism: new evidence from the 1996 eruption. *Earth Planet. Sci. Lett.* **206,** 459-475.

Crane, K., Doss, H., Vogt, P., Sundvor, E., Cherkashov, G., Poroshina, I., Joseph, D. (2001) The role of the Spitsbergen shear zone in determining morphology, segmentation and evolution of the Knipovich Ridge. *Mar. Geophys. Res.* **22,** 153-205.

Debaille, V., Trønnes, R.G., Brandon, A.D., Waight, T.E., Graham, D.W., Lee, C.-T.A. (2009) Primitive off-rift basalts from Iceland and Jan Mayen: Os-isotopic evidence for a mantle source containing enriched subcontinental lithosphere. *Geochim. Cosmochim. Acta* **73,** 3423-3449.

Devey, C.W., Garbeschonberg, C.D., Stoffers, P., Chauvel, C., Mertz, D.F. (1994) Geochemical Effects of Dynamic Melting beneath Ridges - Reconciling Major and Trace-Element Variations in Kolbeinsey (and Global) Midocean Ridge Basalt. *J. Geophys. Res.-Sol. Ea.* **99,** 9077-9095.

Dick, H.J.B., Fisher, R.L., Bryan, W.B. (1984) Mineralogic Variability of the Uppermost Mantle Along Mid-Ocean Ridges. *Earth Planet. Sci. Lett.* **69,** 88-106.

Dick, H.J.B., Lin, J., Schouten, H. (2003) An ultraslow-spreading class of ocean ridge. *Nature* **426,** 405-412.

Dupre, B., Allegre, C.J. (1980) Pb-Sr-Nd Isotopic Correlation and the Chemistry of the North-Atlantic Mantle. *Nature* **286,** 17-22.

Elkins, L.J., Gaetani, G.A., Sims, K.W.W. (2008) Partitioning of U and Th during garnet pyroxenite partial melting: Constraints on the source of alkaline ocean island basalts. *Earth Planet. Sci. Lett.* **265,** 270-286.

Elkins, L.J., Sims, K.W.W., Prytulak, J., Mattielli, N., Elliott, T., Blichert-Toft, J., Blusztajn, J., Dunbar, N., Devey, C.W., Mertz, D.F., Schilling, J.G. (2011) Understanding melt generation beneath the slow spreading Kolbeinsey Ridge from ^{238}U, ^{230}Th, and ^{231}Pa excesses. *Geochim. Cosmochim. Acta* **75,** 6300-6329.

Elliott, T., Spiegelman, M., 2003. Melt Migration in Oceanic Crustal Production: A U-series Perspective, in: Rudnick, R.L. (Ed.), *Treatise on Geochemistry*. Elsevier, Amsterdam, pp. 465-510.

Fretzdorff, S., Haase, K.M., Leat, P.T., Livermore, R.A., Garbe-Schonberg, C.D., Fietzke, J., Stoffers, P. (2003) Th-230-U-238 disequilibrium in East Scotia backarc basalts: Implications for slab contributions. *Geology* **31,** 693-696.

Frey, F.A. (1980) The origin of pyroxenites and garnet pyroxenites from Salt Lake Crater, Oahu, Hawaii: trace element evidence. *Am. Journal Sci.* **280A,** 427-449.

Furman, T., Frey, F.A., Park, K.H. (1991) Chemical Constraints on the Petrogenesis of Mildly Alkaline Lavas from Vestmannaeyjar, Iceland - the Eldfell (1973) and Surtsey (1963-1967) Eruptions. *Contrib. Mineral. Pet.* **109,** 19-37.

Glass, J.B., Cooper, K.M., Alt, J.C., Elliott, T., Teagle, D.A. (2005) Recent Alteration of 15-Ma Oceanic Crust, ODP Site 1256, Leg 206. *Eos Trans. American Geophys. Union* **86,** V43B-1568.

Glebovsky, V.Y., Kaminsky, V.D., Minakov, A.N., Merkur'ev, S.A., Childers, V.A., Brozena, J.M. (2006) Formation of the Eurasia Basin in the arctic ocean as inferred from geohistorical analysis of the anomalous magnetic. *Geotectonics* **40,** 263-281.

Goldstein, S.J., Murrell, M.T., Jackecky, D.R. (1989) Th and U isotopic systematics of basalts from the Juan de Fuca and Gorda Ridges by mass spectrometry. *Earth Planet. Sci. Lett.* **96,** 134-146.

Goldstein, S.J., Murrell, M.T., Janecky, D.R., Delaney, J.R., Clague, D.A. (1991) Geochronology and Petrogenesis of Morb from the Juan-De-Fuca and Gorda Ridges by U-238 Th-230 Disequilibrium. *Earth Planet. Sci. Lett.* **109,** 255-272.

Goldstein, S.J., Murrell, M.T., Williams, R.W. (1993) Pa-231 and Th-230 Chronology of Midocean Ridge Basalts. *Earth Planet. Sci. Lett.* **115,** 151-159.

Goldstein, S.L., Soffer, G., Langmuir, C.H., Lehnert, K.A., Graham, D.W., Michael, P.J. (2008) Origin of a 'Southern Hemisphere' geochemical signature in the Arctic upper mantle. *Nature* **453,** 89-93.

Griffin, W.L., Nikolic, N., O'Reilly, S.Y., Pearson, N.J. (2012) Coupling, decoupling and metasomatism: Evolution of crust-mantle relationships beneath NW Spitsbergen. *Lithos* **149,** 115-135.

Haase, K.M., Devey, C.W., Mertz, D.F., Stoffers, P., GarbeSchonberg, D. (1996) Geochemistry of lavas from Mohns ridge, Norwegian-Greenland Sea: Implications for melting conditions and magma sources near Jan Mayen. *Contrib. Mineral. Pet.* **123,** 223-237.

Haase, K.M., Devey, C.W., Wieneke, M. (2003) Magmatic processes and mantle heterogeneity beneath the slow-spreading northern Kolbeinsey Ridge segment, North Atlantic. *Contrib. Mineral. Pet.* **144,** 428-448.

Haase, K.M., Goldschmidt, B., Garbe-Schonberg, C.D. (2004) Petrogenesis of tertiary continental intra-plate lavas from the Westerwald region, Germany. *Journal of Petrology* **45,** 883-905.

Hanan, B.B., Blichert-Toft, J., Kingsley, R., Schilling, J.G. (2000) Depleted Iceland mantle plume geochemical signature: artifact of multicomponent mixing? *Geochem. Geophys. Geosy*s. **1,** 1003.

Hardarson, B.S., Fitton, J.G. (1997) Mechanisms of crustal accretion in Iceland. *Geology* **25,** 1043-1046.

Hards, V.L., Kempton, P.D., Thompson, R.N. (1995) The Heterogeneous Iceland Plume - New Insights from the Alkaline Basalts of the Snaefell Volcanic Center. *J. Geol. Soc. London* **152,** 1003-1009.

Hart, S.R., Blusztajn, J. (2006) Age and geochemistry of the mafic sills, ODP site 1276, Newfoundland margin. *Chemical Geology* **235,** 222-237.

Hart, S. R., M. Coetzee, R. K. Workman, J. Blusztajn, K. T. M. Johnson, J. M. Sinton, B. Steinberger and J. W. Hawkins (2004) Genesis of the Western Samoa Seamount Province: Age, Geochemical Fingerprint and Tectonics. *Earth Planet. Sci. Lett.* **227,** 37-56.

Hauri, E.H., Wagner, T.P., Grove, T.L. (1994) Experimental and Natural Partitioning of Th, U, Pb and Other Trace-Elements between Garnet, Clinopyroxene and Basaltic Melts. *Chemical Geology* **117,** 149-166.

Hellebrand, E., Snow, J.E. (2003) Deep melting and sodic metasomatism underneath the highly oblique-spreading Lena Trough (Arctic Ocean). *Earth Planet. Sci. Lett.* **216,** 283-299.

Hellebrand, E., Snow, J.E., Muhe, R. (2002) Mantle melting beneath Gakkel Ridge (Arctic Ocean): abyssal peridotite spinel compositions. *Chemical Geology* **182,** 227-235.

Hellevang, B., Pedersen, R.B. (2005) Magmatic segmentation of the northern Knipovich Ridge: Evidence for high-pressure fractionation at an ultraslow spreading ridge. *Geochem. Geophys. Geosys.* **6,** 2004GC000898.

Hemond, C., Arndt, N.T., Lichtenstein, U., Hofmann, A.W., Oskarsson, N., Steinthorsson, S. (1993) The Heterogeneous Iceland Plume - Nd-Sr-O Isotopes and Trace-Element Constraints. *J. Geophys. Res.-Sol. Ea.* **98,** 15833-15850.

Hilton, D.R., Thirlwall, M.F., Taylor, R.N., Murton, B.J., Nichols, A. (2000) Controls on magmatic degassing along the Reykjanes Ridge with implications for the helium paradox. *Earth Planet. Sci. Lett.* **183,** 43-50.

Hirschmann, M.M., Stolper, E.M. (1996) A possible role for garnet pyroxenite in the origin of the "garnet signature" in MORB. *Contrib. Mineral. Pet.* **124,** 185-208.

Hirschmann, M.M., Kogiso, T., Baker, M.B., Stolper, E.M. (2003) Alkalic magmas generated by partial melting of garnet pyroxenite. *Geology* **31,** 481-484.

Hoffmann, D.L., Prytulak, J., Richards, D.A., Elliott, T., Coath, C.D., Smart, P.L., Scholz, D. (2007) Procedures for accurate U and Th isotope measurements by high precision MC-ICPMS. *International Journal of Mass Spectrometry* **264,** 97-109.

Holden, N.E. (1990) Total Half-Lives for Selected Nuclides. *Pure and Applied Chemistry* **62,** 941-958.

Ito, G., Mahoney, J.J., 2005. Flow and melting of a heterogeneous mantle: 1. Method and importance to the geochemistry of ocean island and mid-ocean ridge basalts. *Earth Planet. Sci. Lett.* **230**, 29-46.

Iwamori, H. (1994) ^{238}U-^{230}Th-^{226}Ra and ^{235}U-^{231}Pa disequilibria produced by mantle melting with porous and channel flows. *Earth Planet. Sci. Lett.* **125,** 1-16.

Jackson, M.G., Hart, S.R., 2006. Strontium isotopes in melt inclusions from Samoan basalts: Implications for heterogeneity in the Samoan plume. *Earth Planet. Sci. Lett.* **245**, 260-277.

Jaffey, A.H., Flynn, K.F., Glendeni.Le, Bentley, W.C., Essling, A.M. (1971) Precision Measurement of Half-Lives and Specific Activities of U-235 and U-238. *Physical Review* **C4,** 1889-1906.

Jakobsson, M., Macnab, R., Mayer, L., Anderson, R., Edwards, M., Hatzky, J., Schenke, H.W., Johnson, P. (2008) An improved bathymetric portrayal of the Arctic Ocean: Implications for ocean modeling and geological, geophysical and oceanographic analyses. *Geophysical Research Letters* **35,** L07602-07605.

Jokat, W., Schmidt-Aursch, M.C. (2007) Geophysical characteristics of the ultraslow spreading Gakkel Ridge, Arctic Ocean. *Geophysical Journal International* **168,** 983-998.

Jokat, W., Kollofrath, J., Geissler, W.H., Jensen, L. (2012) Crustal thickness and earthquake distribution south of the Logachev Seamount, Knipovich Ridge. *Geophysical Research Letters* **39.**

Jull, M., Kelemen, P., Sims, K. (2002) Consequences of diffuse and channeled porous melt migration on uranium series disequilibria. *Geochim. Cosmochim. Acta* **66,** A719.

Kandilarov, A., Mjelde, R., Okino, K., Murai, Y. (2008) Crustal structure of the ultra-slow spreading Knipovich Ridge, North Atlantic, along a presumed amagmatic portion of oceanic crustal formation. *Mar. Geophys. Res.* **29,** 109-134.

Kelemen, P.B., Hirth, G., Shimizu, N., Spiegelman, M., Dick, H.J.B. (1997) A review of melt migration processes in the adiabatically upwelling mantle beneath oceanic spreading ridges. *Phil. Trans. Royal Soc. London* **355,** 283-318.

Klein, E.M., Langmuir, C.H. (1987) Global Correlations of Ocean Ridge Basalt Chemistry with Axial Depth and Crustal Thickness. *J. Geophys. Res.-Solid* **92,** 8089-8115.

Klemme, S. and O'Neill, H.S. (2000) The near-solitud transition in CMAS. *Contrib. Mineral. Petrol.* **138,** 237-248.

Klingelhofer, F., Geli, L., White, R.S. (2000) Geophysical and geochemical constraints on crustal accretion at the very-slow spreading Mohns Ridge. *Geophysical Research Letters* **27,** 1547-1550.

Kodaira, S., Mjelde, R., Gunnarsson, K., Shiobara, H., Shimamura, H. (1997) Crustal structure of the Kolbeinsey Ridge, North Atlantic, obtained by use of ocean bottom seismographs. *J. Geophys. Res.-Sol. Ea.* **102,** 3131-3151.

Kogiso, T., Hirschmann, M.M., Pertermann, M. (2004) High-pressure partial melting of mafic lithologies in the mantle. *Journal of Petrology* **45,** 2407-2422.

Kokfelt, T.F., Hoernle, K., Hauff, F. (2003) Upwelling and melting of the Iceland plume from radial variation of U-238-Th-230 disequilibria in postglacial volcanic rocks. *Earth Planet Sc Lett* **214,** 167-186.

Kokfelt, T.F., Lundstrom, C., Hoernle, K., Hauff, F., Werner, R. (2005) Plume-ridge interaction studied at the Galapagos spreading center: Evidence from Ra-226-Th-230-U-238 and Pa-231-U-235 isotopic disequilibria. *Earth Planet. Sci. Lett.* **234,** 165-187.

Kokfelt, T.F., Hoernle, K., Hauff, F., Fiebig, J., Werner, R., Garbe-Schonberg, D., 2006. Combined trace element and Pb-Nd-Sr-O isotope evidence for recycled oceanic crust (upper and lower) in the Iceland mantle plume. *Journal of Petrology* **47**, 1705-1749.

Koornneef, J.M., Stracke, A., Meier, M.A., Bourdon, B., Gronvold, K., Stoll, B., Jochum, K.P. (2010) Plume-influenced melting of a two-component source beneath Iceland. *Geochim. Cosmochim. Acta* **74,** A530.

Koornneef, J.M., Stracke, A., Bourdon, B., Meier, M.A., Jochum, K.P., Stoll, B., Gronvold, K., 2012. Melting of a Two-component Source beneath Iceland. *Journal of Petrology* **53**, 127-157.

Ku, T.L., Knauss, K.G., Mathieu, G.G. (1977) Uranium in Open Ocean - Concentration and Isotopic Composition. *Deep-Sea Research* **24,** 1005-1017.

La Tourette, T.Z., Burnett, D.S. (1992) Experimental determination of U-partitioning and Th-partitioning between cpx and natural and synthetic basaltic liquid. *Earth Planet. Sci. Lett.* **110,** 227-244.

La Tourette, T.Z., Kennedy, A.K., Wasserburg, G.J. (1993). Thorium-uranium fractionation by garnet: Evidence for a deep source and rapid rise of oceanic basalts. *Science* **261,** 729-742.

Landwehr, D., Blundy, J., Chamorro-Perez, E.M., Hill, E., Wood, B. (2001) U-series disequilibria generated by partial melting of spinel lherzolite. *Earth Planet. Sci. Lett.* **188,** 329-348.

Langmuir, C., Klein, E.M., Plank, T. (1992) Petrological systematics of mid-ocean ridge basalts: constraints on melt generation beneath ocean ridges. *Mantle Flow and Melt Generation at Mid-Ocean Ridges,* AGU Monograph, pp. 183-280.

Lassiter, J.C., Snow, J.E. (2009) Os-isotope constraints on the origin of Lena Trough peridotites, Arctic Ocean: Asthenospheric mantle or continental lithosphere? *Geochim. Cosmochim. Acta* **73,** A725.

Le Roux, L.J., Glendenin, L.E. (1963) Half-life of ^{232}Th. *Proceedings of the National Meeting on Nuclear Energy*, Pretoria, South Africa, pp. 83-94.

Lin, J., Purdy, G.M., Schouten, H., Sempere, J.C., Zervas, C., 1990. Evidence from Gravity-Data for Focused Magmatic Accretion Along the Mid-Atlantic Ridge. *Nature* **344**, 627-632.

Liu, C.Z., Snow, J.E., Hellebrand, E., Brugmann, G., von der Handt, A., Buchl, A., Hofmann, A.W. (2008) Ancient, highly heterogeneous mantle beneath Gakkel ridge, Arctic Ocean. *Nature* **452,** 311-316.

Ljones, F., Kuwano, A., Mjelde, R., Breivik, A., Shimamura, H., Murai, Y., Nishimura, Y. (2004) Crustal transect from the North Atlantic Knipovich Ridge to the Svalbard margin west of hornsund. *Tectonophysics* **378,** 17-41.

Lundstrom, C. (2000) Models of U-series disequilibria generation in MORB: the effects of two scales of melt porosity. *Phys. Earth Planet. Int.* **121,** 189-204.

Lundstrom, C.C. (2003) Uranium-series disequilibria in mid-ocean ridge basalts: Observations and models of basalt genesis. *Rev. Mineral. Geochem.* **52,** 175-214.

Lundstrom, C.C., Gill, J., Williams, Q., Perfit, M.R. (1995) Mantle Melting and Basalt Extraction by Equilibrium Porous Flow. *Science* **270,** 1958-1961.

Lundstrom, C.C., Gill, J., Williams, Q., Hanan, B.B. (1998a) Investigating solid mantle upwelling beneath mid-ocean ridges using U-series disequilibria. II. A local study at 33 degrees Mid-Atlantic Ridge. *Earth Planet. Sci. Lett.* **157,** 167-181.

Lundstrom, C.C., Williams, Q., Gill, J.B. (1998b) Investigating solid mantle upwelling rates beneath mid-ocean ridges using U-series disequilibria, 1: a global approach. *Earth Planet. Sci. Lett.* **157,** 151-165.

Lundstrom, C.C., Sampson, D.E., Perfit, M.R., Gill, J., Williams, Q. (1999) Insights into mid-ocean ridge basalt petrogenesis: U-series disequilibria from the Siqueiros Transform, Lamont Seamounts, and East Pacific Rise. *J. Geophys. Res.-Sol. Ea.* **104,** 13035-13048.

Macdougall, J.D. (1977) Uranium in Marine Basalts - Concentration, Distribution and Implications. *Earth Planet. Sci. Lett.* **35,** 65-70.

Macdougall, J.D., Finkel, R.C., Carlson, J., Krishnaswami, S. (1979) Isotopic Evidence for Uranium Exchange during Low-Temperature Alteration of Oceanic Basalt. *Earth Planet. Sci. Lett.* **42,** 27-34.

Mckenzie, D. (1985) Th-230-U-238 Disequilibrium and the Melting Processes beneath Ridge Axes. *Earth Planet. Sci. Lett.* **72,** 149-157.

Mertz, D.F., Haase, K.M. (1997) The radiogenic isotope composition of the high-latitude North Atlantic mantle. *Geology* **25,** 411-414.

Mertz, D.F., Devey, C.W., Todt, W., Stoffers, P., Hofmann, A.W. (1991) Sr-Nd-Pb Isotope Evidence against Plume Asthenosphere Mixing North of Iceland. *Earth Planet. Sci. Lett.* **107,** 243-255.

Mertz, D.F., Sharp, W.D., Haase, K.M. (2004) Volcanism on the Eggvin Bank (Central Norwegian-Greenland Sea, latitude similar to 71 degrees N): age, source, and relationship to the Iceland and putative Jan Mayen plumes. *J. Geodynamics* **38,** 57-83.

Michael, P.J., Langmuir, C.H., Dick, H.J.B., Snow, J.E., Goldstein, S.L., Graham, D.W., Lehnert, K., Kurras, G., Jokat, W., Muhe, R., Edmonds, H.N. (2003) Magmatic and amagmatic seafloor generation at the ultraslow-spreading Gakkel ridge, Arctic Ocean. *Nature* **423,** 956-961.

Mjelde, R., Breivik, A.J., Raum, T., Mittelstaedt, E., Ito, G., Faleide, J.I. (2008a) Magmatic and tectonic evolution of the North Atlantic. *J. Geol. Soc. London* **165,** 31-42.

Mjelde, R., Raum, T., Breivik, A.J., Faleide, J.I. (2008b) Crustal transect across the North Atlantic. *Mar. Geophys. Res.* **29,** 73-87.

Montesi, L.G.J., Behn, M.D. (2007) Mantle flow and melting underneath oblique and ultraslow mid-ocean ridges. *Geophysical Research Letters* **34,** L24307.

Moran, S.B., Buesseler, K.O. (1992) Short Residence Time of Colloids in the Upper Ocean Estimated from U-238 Th-234 Disequilibria. *Nature* **359,** 221-223.

Moran, S.B., Buesseler, K.O. (1993) Size-Fractionated Th-234 in Continental-Shelf Waters Off New-England - Implications for the Role of Colloids in Oceanic Trace-Metal Scavenging. *J. Mar. Res.* **51,** 893-922.

Mosar, J., Lewis, G., Torsvik, T.H. (2002) North Atlantic sea-floor spreading rates: implications for the Tertiary development of inversion structures of the Norwegian-Greenland Sea. *J. Geol. Soc. London* **159,** 503-515.

Murton, B.J., Taylor, R.N., Thirlwall, M.F. (2002) Plume-ridge interaction: A geochemical perspective from the Reykjanes Ridge. *Journal of Petrology* **43,** 1987-2012.

Nauret, F., Moreira, M., Snow, J.E. (2010) Rare gases in lavas from the ultraslow spreading Lena Trough, Arctic Ocean. *Geochem. Geophys. Geosys.* **11,** 2010GC003027.

Nauret, F., Snow, J.E., Hellebrand, E., Weis, D. (2011) Geochemical Composition of K-rich Lavas from the Lena Trough (Arctic Ocean). *Journal of Petrology* **52,** 1185-1206.

Neumann, E.R., Schilling, J.G. (1984) Petrology of Basalts from the Mohns-Knipovich Ridge - the Norwegian-Greenland Sea. *Contrib. Mineral. Pet.* **85,** 209-223.

Niu, Y.L., Batiza, R. (1993) Chemical Variation Trends at Fast and Slow-Spreading Midocean Ridges. *J. Geophys. Res.-Sol. Ea.* **98,** 7887-7902.

Niu, Y.L., Batiza, R. (1997) Trace element evidence from seamounts for recycled oceanic crust in the eastern Pacific mantle. *Earth Planet. Sci. Lett.* **148,** 471-483.

Niu, Y.L., Bideau, D., Hekinian, R., Batiza, R. (2001) Mantle compositional control on the extent of mantle melting, crust production, gravity anomaly, ridge morphology, and ridge segmentation: a case study at the Mid-Atlantic Ridge 33-35 degrees N. *Earth Planet. Sci. Lett.* **186,** 383-399.

Nixon, P.H. (1987) *Mantle xenoliths.* Wiley, New York.

O'Neill, H.S., Jenner, F.E., 2012. The global pattern of trace-element distributions in ocean floor basalts. *Nature* **491**, 698.

O'Nions, R.K., Pankhurst, R.J. (1973) Secular Variation in Sr-Isotope Composition of Icelandic Volcanic-Rocks. *Earth Planet. Sci. Lett.* **21,** 13-21.

Okino, K., Curewitz, D., Asada, M., Tamaki, K., Vogt, P., Crane, K. (2002) Preliminary analysis of the Knipovich Ridge segmentation: influence of focused magmatism and ridge obliquity on an ultraslow spreading system. *Earth Planet. Sci. Lett.* **202,** 275-288.

Pearson, G.B., Messiga, B., Vannucci, R. (1988) Geochemical constraints on the petrogenesis of diamond facies pyroxenites from the Beni Bousera peridotite massif. *Journal of Petrology* **34,** 125-172.

Peate, D.W., Hawkesworth, C.J., van Calsteren, P.W., Taylor, R.N., Murton, B.J. (2001) U-238-Th-230 constraints on mantle upwelling and plume-ridge interaction along the Reykjanes Ridge. *Earth Planet. Sci. Lett.* **187,** 259-272.

Pelt, E., Chabaux, F., Innocent, C., Navarre-Sitchler, A.K., Sak, P.B., Brantley, S.L. (2008) Uranium-thorium chronometry of weathering rinds: Rock alteration rate and paleo-isotopic record of weathering fluids. *Earth Planet. Sci. Lett.* **276,** 98-105.

Pertermann, M., Hirschmann, M. (2003a) Partial melting experiments on MORB-like pyroxenite between 2 and 3 GPa: Constraints on the presence of pyroxenite in basalt source regions from solidus location and melting rate. *J. Geophys. Res.* **108(B2),** 2125.

Pertermann, M., Hirschmann, M.M. (2003b) Anhydrous partial melting experiments on MORB-like eclogite: Phase relations, phase compositions and mineral-melt partitioning of major elements at 2-3 GPa. *Journal of Petrology* **44,** 2173-2201.

Pertermann, M., Hirschmann, M.M., Hametner, K., Gunther, D., Schmidt, M.W. (2004) Experimental determination of trace element partitioning between garnet and silica-rich liquid during anhydrous partial melting of MORB-like eclogite. *Geochem. Geophys. Geosys.* **5,** Q05A01.

Pickett, D.A., Murrell, M.T. (1997) Observations of (^{231}Pa)/(^{235}U) disequilibrium in volcanic rocks. *Earth Planet. Sci. Lett.* **148,** 259-271.

Pietruszka, A.J., Rubin, K.H., Garcia, M.O. (2001) Ra-226-Th-230-U-238 disequilibria of historical Kilauea lavas (1790-1982) and the dynamics of mantle melting within the Hawaiian plume. *Earth Planet. Sci. Lett.* **186,** 15-31.

Pietruszka, A.J., Hauri, E.H., Blichert-Toft, J. (2009) Crustal contamination of mantle-derived magmas within Piton de la Fournaise Volcano, Réunion Island. *Journal of Petrology* **50,** 661-684.

Pietruszka, A.J., Keyes, M.J., Duncan, J.A., Hauri, E.H., Carlson, R.W., Garcia, M.O. (2011) Excesses of seawater-derived ^{234}U in volcanic glasses from Loihi Seamount due to crustal contamination. *Earth Planet. Sci. Lett.* **304,** 280-289.

Poreda, R., Schilling, J.G., Craig, H. (1986) Helium and Hydrogen Isotopes in Ocean-Ridge Basalts North and South of Iceland. *Earth Planet. Sci. Lett.* **78,** 1-17.

Prytulak, J., Elliott, T. (2009) Determining melt productivity of mantle sources from U-238-Th-230 and U-235-Pa-231 disequilibria; an example from Pico Island, Azores. *Geochim. Cosmochim. Acta* **73,** 2103-2122.

Prytulak, J., Elliott, T., Hoffmann, D.L., Coath, C.D. (2008) Assessment of USGS BCR-2 as a reference material for silicate rock u-pa disequilibrium measurements. *Geostand. Geoanal. Res.* **32,** 55-63.

Reagan, M., Tepley, III, F.J., Gill, J.B., Wortel, M., Hartman, B. (2005) Rapid time scales of basalt to andesite differentiation at Anatahan volcano, Mariana Islands. *J. Volcanol. Geotherm. Res.* **146,** 171-183.

Reagan, M., Tepley, III, F.J., Gill, J.B., Wortel, M., Garrison, J. (2006) Timescales of degassing and crystallization implied by ^{210}Po-^{210}Pb-^{226}Ra disequilibria for andesitic lavas erupted from Arenal volcano. *Jour. Volc. Geotherm. Res.* **157,** 135-146.

Regelous, M., Turner, S.P., Elliott, T.R., Rostami, K., Hawkesworth, C.J. (2004) Measurement of femtogram quantities of protactinium in silicate rock samples by multicollector inductively coupled plasma mass spectrometry. *Analytical Chemistry* **76,** 3584-3589.

Richter, S., Alonso, A., Truyens, J., Kühn, H., Verbruggen, A., Wellum, R. (2006) *REIMEP 18: Inter-Laboratory Comparison for the Measurement of Uranium Isotopic Radios in Nitric Acid Solution.* European Commission.

Ritzmann, O., Jokat, W., Mjelde, R., Shimamura, H. (2002) Crustal structure between the Knipovich Ridge and the Van Mijenfjorden (Svalbard). *Mar. Geophys. Res*. **23,** 379-401.

Robinson, J.A.C. and Wood, B.J. (1998) The depth of the spinel to garnet transition at the peridotite solidus. *Earth Planet. Sci. Lett.* **164,** 277-284.

Rubin, K.H., 2001. Analysis of Th-232/Th-230 in volcanic rocks: a comparison of thermal ionization mass spectrometry and other methodologies. *Chemical Geology* **175**, 723-750.

Rubin, K.H., van der Zander, I., Smith, M.C., Bergmanis, E.C. (2005) Minimum speed limit for ocean ridge magmatism from Pb-210-Ra-226-Th-230 disequilibria. *Nature* **437,** 534-538.

Rudge, J.F., Maclennan, J., Stracke, A., 2013. The geochemical consequences of mixing melts from a heterogeneous mantle. *Geochim. Cosmochim. Acta* **114**, 112-143.

Russo, C.J., Rubin, K.H., Graham, D.W. (2009) Mantle melting and magma supply to the Southeast Indian Ridge: The roles of lithology and melting conditions from U-series disequilibria. *Earth Planet. Sci. Lett.* **278,** 55-66.

Saal, A.E., Van Orman, J.A., 2004. The Ra-226 enrichment in oceanic basalts: Evidence for melt-cumulate diffusive interaction processes within the oceanic lithosphere. *Geochem. Geophys. Geosys.* **5**.

Salters, V.J.M. (1996) The generation of mid-ocean ridge basalts from the Hf and Nd isotope perspective. *Earth Planet. Sci. Lett.* **141,** 109-123.

Salters, V.J.M., Longhi, J. (1999) Trace element partitioning during the initial stages of melting beneath mid-ocean ridges. *Earth Planet. Sci. Lett.* **166,** 15-30.

Salters, V.J.M., White, W.M. (1998) Hf isotope constraints on mantle evolution. *Chemical Geology* **145,** 447-460.

Salters, V.J.M., Longhi, J.E., Bizimis, M. (2002) Near mantle solidus trace element partitioning at pressures up to 3.4 GPa. *Geochem. Geophys. Geosys.* **3,** 1038.

Salters, V.J.M., Mallick, S., Hart, S.R., Langmuir, C.E., Stracke, A. (2011) Domains of depleted mantle: New evidence from hafnium and neodymium isotopes. *Geochem. Geophys. Geosys.* **12,** 2011GC003617.

Schilling, J.G. (1975) Rare-Earth Variations across Normal-Segments of Reykjanes Ridge, 60 degrees-53 degrees N, Mid-Atlantic Ridge, 29 degrees S, and East Pacific Rise, 2 degrees-19 degrees S, and Evidence on Composition of Underlying Low-Velocity Layer. *J. Geophys. Res.* **80,** 1459-1473.

Schilling, J.G., Zajac, M., Evans, R., Johnston, T., White, W., Devine, J.D., Kingsley, R. (1983) Petrologic and Geochemical Variations Along the Mid-Atlantic Ridge from 29-Degrees-N to 73-Degrees-N. *Am. J. Sci.* **283,** 510-586.

Schilling, J.G., Kingsley, R., Fontignie, D., Poreda, R., Xue, S. (1999) Dispersion of the Jan Mayen and Iceland mantle plumes in the Arctic: A He-Pb-Nd-Sr isotope tracer study of basalts from the Kolbeinsey, Mohns, and Knipovich Ridges. *J. Geophys. Res.-Sol. Ea.* **104,** 10543-10569.

Shipilov, E.V. (2008) Generations of spreading basins and stages of breakdown of Wegener's Pangea in the geodynamic evolution of the Arctic Ocean. *Geotectonics* **42,** 105-124.

Shorttle, O., Maclennan, J., 2011. Compositional trends of Icelandic basalts: Implications for short-length scale lithological heterogeneity in mantle plumes. *Geochem. Geophys. Geosys.* **12**.

Sigmarsson, O., Carn, S., Carracedo, J.C. (1998) Systematics of U-series nuclides in primitive lavas from the 1730-36 eruption on Lanzarote, Canary Islands, and implications for the role of garnet pyroxenites during oceanic basalt formations. *Earth Planet. Sci. Lett.* **162,** 137-151.

Sigurdsson, H. (1981) 1st-Order Major Element Variation in Basalt Glasses from the Mid-Atlantic Ridge - 29-Degrees-N to 73-Degrees-N. *J. Geophys. Res.* **86,** 9483-9502.

Sims, K.W.W., Hart, S.R. (2006) Comparison of Th, Sr, Nd and Pb isotopes in oceanic basalts: Implications for mantle heterogeneity and magma genesis. *Earth Planet Sc Lett* **245,** 743-761.

Sims, K.W.W., Depaolo, D.J., Murrell, M.T., Baldridge, W.S., Goldstein, S.J., Clague, D.A. (1995) Mechanisms of Magma Generation beneath Hawaii and Midocean Ridges - Uranium/Thorium and Samarium/Neodymium Isotopic Evidence. *Science* **267,** 508-512.

Sims, K.W.W., DePaolo, D.J., Murrell, M.T., Baldridge, W.S., Goldstein, S., Clague, D., Jull, M. (1999) Porosity of the melting zone and variations in the solid mantle upwelling rate beneath Hawaii: Inferences from U-238-Th-230-Ra-226 and U-235-Pa-231 disequilibria. *Geochim. Cosmochim. Acta* **63,** 4119-4138.

Sims, K.W.W., Goldstein, S.J., Blichert-Toft, J., Perfit, M.R., Kelemen, P., Fornari, D.J., Michael, P., Murrell, M.T., Hart, S.R., DePaolo, D.J., Layne, G., Ball, L., Jull, M.,

Bender, J. (2002) Chemical and isotopic constraints on the generation and transport of magma beneath the East Pacific Rise. *Geochim. Cosmochim. Acta* **66,** 3481-3504.

Sims, K.W.W., Blichert-Toft, J., Fornari, D.J., Perfit, M.R., Goldstein, S.J., Johnson, P., DePaolo, D.J., Hart, S.R., Murrell, P.J., Michael, P.J., Layne, G.D., Ball, L.A. (2003) Aberrant youth: Chemical and isotopic constraints on the origin of off-axis lavas from the East Pacific Rise, 9 degrees-10 degrees N. *Geochem. Geophys. Geosys.* **4,** 8621.

Sims, K.W.W., Gill, J.B., Dosseto, A., Hoffmann, D.L., Lundstrom, C.C., Williams, R.W., Ball, L., Tollstrup, D., Turner, S., Prytulak, J., Glessner, J.J.G., Standish, J.J., Elliott, T. (2008a) An inter-laboratory assessment of the thorium isotopic composition of synthetic and rock reference materials. *Geostand. Geoanal. Res.* **32,** 65-91.

Sims, K.W.W., Hart, S.R., Reagan, M.K., Blusztajn, J., Staudigel, H., Sohn, R.A., Layne, G.D., Ball, L.A. (2008b) ^{238}U-^{230}Th-^{226}Ra-^{210}Pb-^{210}Po, ^{232}Th-^{228}Ra, and ^{235}U-^{231}Pa constraints on the ages and petrogenesis of Vailulu'u and Malumalu Lavas, Samoa. *Geochem. Geophys. Geosy*s. **9,** Q04003.

Sims, K.W.W., Maclennan, J., Blichert-Toft, J., Mervine, E.M., Bluzstajn, J., Grönvold, K. (2013) Short length scale mantle heterogeneity beneath Iceland probed by glacial modulation of melting. *Ear. Planet. Sci. Lett.* **379,** 146-157.

Sims, K.W.W., Pichat, S., Reagan, M.K., Kyle, P.R., Dulaiova, H., Dunbar, N.W., Prytulak, J., Sawyer, G., Layne, G.D., Blichert-Toft, J., Gauthier, P.J., Charette, M.A., and Elliott, T.R. (2013) On the time scales of magma genesis, melt evolution, crystal growth rates and magma degassing in the Erebus Volcano magmatic system using the ^{238}U, ^{235}U, and ^{232}Th decay series. *Jour. Petrology* **54,** 235-271.

Small, C. (1998) in: Buck, W., Dleaney, P.T., Karson, J.A., Lagabrielle, Y. (Eds.), *Faulting and Magmatism at Mid-Ocean Ridges.* American Geophysical Union, Washington, D.C., pp. 1-26.

Smith, W.H.F., Sandwell, D.T. (1997) Global sea floor topography from satellite altimetry and ship depth soundings. *Science* **277,** 1956-1962.

Sokolov, S.Y. (2011) Tectonic evolution of the Knipovich Ridge based on the anomalous magnetic field. *Doklady Earth Sciences* **437,** 343-348.

Spiegelman, M., 2000. UserCalc: a web-based uranium series calculator for magma migration problems. *Geochem. Geophys. Geosys.* **1**, 11.

Spiegelman, M., Elliott, T. (1993) Consequences of Melt Transport for Uranium Series Disequilibrium in Young Lavas. *Earth Planet. Sci. Lett.* **118,** 1-20.

Standish, J.J., Sims, K.W.W. (2010) Young off-axis volcanism along the ultraslow-spreading Southwest Indian Ridge. *Nature Geoscience* **3,** 286-292.

Stecher, O., Carlson, R.W., Gunnarsson, B. (1999) Torfajokull: a radiogenic end-member of the Iceland Pb-isotopic array. *Earth Planet. Sci. Lett.* **165,** 117-127.

Stracke, A., Bourdon, B., 2009. The importance of melt extraction for tracing mantle heterogeneity. *Geochim. Cosmochim. Acta* **73**, 218-238.

Stracke, A., Salters, V.J.M., Sims, K.W.W. (1999) Assessing the presence of garnet-pyroxenite in the mantle sources of basalts through combined hafnium-neodymium-thorium isotope systematics. *Geochem. Geophys. Geosys.* **1,** 1999GC000013.

Stracke, A., Zindler, A., Salters, V.J.M., McKenzie, D., Blichert-Toft, J., Albarede, F., Gronvold, K. (2003a) Theistareykir revisited. *Geochem. Geophys. Geosys.* **4,** 8507.

Stracke, A., Zindler, A., Salters, V.J.M., McKenzie, D., Gronvold, K., 2003b. The dynamics of melting beneath Theistareykir, northern Iceland. *Geochem. Geophys. Geosys.* **4,** 8513.

Stracke, A., Bourdon, B., McKenzie, D. (2006) Melt extraction in the Earth's mantle: Constraints from U-Th-Pa-Ra studies in oceanic basalts. *Earth Planet. Sci. Lett.* **244,** 97-112.

Stracke, A., Snow, J.E., Hellebrand, E., von der Handt, A., Bourdon, B., Birbaum, K., Gunther, D. (2011) Abyssal peridotite Hf isotopes identify extreme mantle depletion. *Earth Planet. Sci. Lett.* **308,** 359-368.

Sturm, M.E., Goldstein, S.J., Klein, E.M., Karson, J.A., Murrell, M.T. (2000) Uranium-series age constraints on lavas from the axial valley of the Mid-Atlantic Ridge, MARK area. *Earth Planet. Sci. Lett.* **181,** 61-70.

Suen, C.J., Frey, F.A. (1987) Origins of the mafic and ultramafic rocks in the Ronda peridotite. *Earth Planet. Sci. Lett.* **85,** 183-202.

Sun, S.S., Jahn, B. (1975) Lead and Strontium Isotopes in Postglacial Basalts from Iceland. *Nature* **255,** 527-530.

Tepley, F.J., Lundstrom, C.C., Sims, K.W.W., Hekinian, R. (2004) U-series disequilibria in MORB from the Garrett Transform and implications for mantle melting. *Earth Planet. Sci. Lett.* **223,** 79-97.

Thirlwall, M.F., Gee, M.A.M., Taylor, R.N., Murton, B.J. (2004) Mantle components in Iceland and adjacent ridges investigated using double-spike Pb isotope ratios. *Geochim. Cosmochim. Acta* **68,** 361-386.

Thurber, D. (1962) Anomalous $^{234}U/^{238}U$ in nature. *J. Geophys. Res.* **67,** 4518-4520.

Todt, W., Cliff, R.A., Hanser, A., Hofmann, A. (1996) Evaluation of a ^{202}Pb-^{205}Pb double spike for high-precision lead isotope analysis, in: Basu, A., Hart, S.R. (Eds.), *Earth Processes Reading the Isotope Code*. AGU, pp. 429-437.

Trønnes, R.G., Planke, S., Sundvoll, B., Imsland, P. (1999) Recent volcanic rocks from Jan Mayen: Low-degree melt fractions of enriched northeast Atlantic mantle. *J. Geophys. Res.-Sol. Ea.* **104,** 7153-7168.

Turekian, K.K., Bertine, K.K. (1971) Deposition of Molybdenum and Uranium Along Major Ocean Ridge Systems. *Nature* **229,** 250-251.

Turner, S., Hawkesworth, C., Rogers, N., King, P. (1997) U-Th isotope disequilibria and ocean island basalt generation in the Azores. *Chemical Geology* **139,** 145-164.

Turner, S., Beier, C., Niu, Y.L., Cook, C., 2011. U-Th-Ra disequilibria and the extent of off-axis volcanism across the East Pacific Rise at 9 degrees 30 ' N, 10 degrees 30 ' N, and 11 degrees 20 ' N. *Geochem. Geophys. Geosys.* **12**.

Urlaub, M., Schmidt-Aursch, M.C., Jokat, W., Kaul, N. (2009) Gravity crustal models and heat flow measurements for the Eurasia Basin, Arctic Ocean. *Mar. Geophys. Res.* **30,** 277-292.

Van Orman, J.A., Saal, A.E., Bourdon, B., Hauri, E.H., 2006. Diffusive fractionation of U-series radionuclides during mantle melting and shallow-level melt-cumulate interaction. *Geochim. Cosmochim. Acta* **70**, 4797-4812.

Waggoner, D. (1989) An isotopic and trace element study of mantle heterogeneity beneath the Norwegian-Greenland Sea. University of Rhode Island, Kingston, RI, p. 270.

Walter, M., Katsura, T., Kubo, A., Shinmei, T., Nishikawa, O., Ito, E., Lesher, C., Funakoshi, K. (2002) Spinel-garnet lherzolite transition in the system CaO-MgO-Al2O3-SiO2 revisited: An in situ X-ray study. *Geochim. Cosmochim. Acta* **66,** 2109-2121.

Waters, C.L., Sims, K.W.W., Perfit, M.R., Blichert-Toft, J., Blusztajn, J. (2011) Perspective on the genesis of E-MORB from chemical and isotopic heterogeneity at 9º-10ºN East Pacific Rise. *Journal of Petrology* **52,** 565-602.

Waters, C.L., Sims, K.W.W., Klein, E.M., White, S.M., Reagan, M., Girard, G. (2013) Sill to surface: Linking young off-axis volcanism with subsurface melt at the overlapping spreading center at 9º03'N East Pacific Rise. *Earth Planet. Sci. Lett.* **369,** 59-70.

Waters, C.L., Sims, K.W.W., Soule, S.A., Blichert-Toft, J., Dunbar, N.W., Plank, T., Prytulak, J., Sohn, R.A., Tivey, M.A. (2013) Recent volcanic accretion at 9-10ºN East Pacific Rise as resolved by combined geochemical and geological observations. *Geochem. Geophys. Geosys.* **14,** 2547-2574.

Widom, E., Carlson, R.W., Gill, J.B., Schmincke, H.U. (1997) Th-Sr-Nd-Pb isotope and trace element evidence for the origin of the Sao Miguel, Azores, enriched mantle source. *Chemical Geology* **140,** 49-68.

Wilshire, H.G., Meyer, C.E., Nakata, J.K., Calk, L.C., Shervais, J.W., Nielson, J.E., Schwarzman, E.C. (1988) Mafic and ultramafic xenoliths from volcanic rocks of the Western United States, in: *USGS (Ed.), Open-File Report,* pp. 85-139.

Wood, B.J., Blundy, J.D., Robinson, J.A.C. (1999) The role of clinopyroxene in generating U-series disequilibrium during mantle melting. *Geochim. Cosmochim. Acta* **63,** 1613-1620.

Workman, R.K., Hart, S.R., 2005. Major and trace element composition of the depleted MORB mantle (DMM). *Earth Planet. Sci. Lett.* **231**, 53-72.

Workman, R.K., Hart, S.R., Jackson, M., Regelous, M., Farley, K.A., Blusztajn, J., Kurz, M., Staudigel, H., 2004. Recycled metasomatized lithosphere as the origin of the Enriched Mantle II (EM2) end-member: Evidence from the Samoan Volcanic Chain. *Geochem. Geophys. Geosys.* **5**.

Yampol'skiy, K.P., Sokolov, S.Y. (2012) Sedimentary Cover and Bouguer Anomalies in the Northern Part of the Knipovich Ridge. *Doklady Earth Sciences* **442,** 188-192.

Zou, H.B., 1998. Trace element fractionation during modal and nonmodal dynamic melting and open-system melting: A mathematical treatment. *Geochim. Cosmochim. Acta* **62**, 1937-1945.

Zou, H.B., Zindler, A. (2000) Theoretical studies of U-238-Th-230-Ra-226 and U-235-Pa-231 disequilibria in young lavas produced by mantle melting. *Geochim. Cosmochim. Acta* **64,** 1809-1817.

Zou, H.B., Zindler, A., Niu, Y.L. (2002) Constraints on melt movement beneath the East Pacific Rise from Th-230-U-238 disequilibrium. *Science* **295,** 107-110.

FIGURE CAPTIONS

Figure 1. Sample locations. (a) Regional map showing dredge and dive locations for Mohns, Knipovich, and Gakkel Ridge samples analyzed in and of interest to this study; bathymetric data by Smith & Sandwell (1997) and Jakobsson et al. (2008). For comparison, blue circles and green triangles indicate the locations of crustally uncontaminated, age-constrained samples measured in Elkins et al. (2011) for the neighboring Kolbeinsey Ridge. (b) Bathymetric and topographic profile along the Arctic ridge system, with sample locations of interest. [To be printed in color.]

Figure 2. Along-axis variations. Distance along the Arctic ridge system vs. radiogenic isotope, trace element, and U-series data (this study and Elkins et al., 2011) in MORB, with regional literature data shown as small black circles (Blichert-Toft et al., 2005; Cohen et al., 1980; Condomines et al., 1981; Devey et al., 1994; Dupre and Allegre, 1980; Elkins et al., 2011; Furman et al., 1991; Goldstein et al., 2008; Haase et al., 2003; Hanan et al., 2000; Hardarson and Fitton, 1997; Hards et al., 1995; Hemond et al., 1993; Hilton et al., 2000; Kokfelt et al., 2003; Mertz et al., 1991; Mertz and Haase, 1997; Murton et al., 2002; Neumann and Schilling, 1984; O'Nions and Pankhurst, 1973; Peate et al., 2001; Poreda et al., 1986; Salters and White, 1998; Schilling, 1975; Schilling et al., 1999; Schilling et al., 1983; Sigurdsson, 1981; Stecher et al., 1999; Stracke et al., 2006; Stracke et al., 2003a; Stracke et al., 2003b; Sun and Jahn, 1975; Thirlwall et al., 2004; Waggoner, 1989). [To be printed in color.]

Figure 3. ^{238}U-^{234}U-^{230}Th of Arctic Basalts. (a) ($^{238}U/^{232}Th$) vs. ($^{230}Th/^{232}Th$) diagram showing data from all Mohns, Knipovich, and Gakkel Ridge samples measured in this study, as well as young, uncontaminated Kolbeinsey Ridge samples, including the Eggvin Bank (Elkins et al., 2011). Symbols for data from this study indicate which samples lack age constraints on ^{238}U-^{230}Th data (i.e. no measured ^{226}Ra or ^{231}Pa excess), which have measured ($^{234}U/^{238}U$) out of equilibrium (indicating likely alteration; see text for criteria), and which lack ($^{234}U/^{238}U$) data implying that alteration is possible (Table 2). Atlantic, Pacific, Indian, and Australian-Antarctic (AAD) MORB data (Bourdon et al., 1996a; Goldstein et al., 1989; Goldstein et al., 1991; Goldstein et al., 1993; Kokfelt et al., 2005; Lundstrom et al., 1999; Peate et al., 2001; Rubin et al., 2005; Russo et al., 2009; Sims et al., 1995; Sims et al., 2002; Standish and Sims, 2010; Sturm et al., 2000; Tepley et al., 2004; Waters et al., 2011), global ocean island basalt (OIB) data

(Bourdon et al., 1998; Claude-Ivanaj et al., 1998; Claude-Ivanaj et al., 2001; Pietruszka et al., 2009; Pietruszka et al., 2001; Prytulak and Elliott, 2009; Sigmarsson et al., 1998; Sims et al., 1999; Sims et al., 1995; Sims and Hart, 2006; Sims et al., 2008b; Turner et al., 1997; Widom et al., 1997); and Icelandic data (Kokfelt et al., 2003; Stracke et al., 2003a; Stracke et al., 2003b), filtered to a first order (see text) for geochemical indicators of alteration and for age constraints, are shown for comparison. Samples from the Eggvin Bank area on the neighboring Northern Kolbeinsey Ridge segment are isotopically enriched and more closely resemble Mohns Ridge and Knipovich Ridge samples than the rest of the Kolbeinsey Ridge (Elkins et al., 2011). Knipovich Ridge data lie along a sloped array, while age-constrained Mohns Ridge ^{238}U-^{230}Th data (Table 2; see Section 5) cluster tightly at the enriched end of the Knipovich data array. Gakkel Ridge samples are relatively trace element-depleted and homogeneous and range from 5% ^{230}Th excesses to 5% ^{238}U excesses. (b) ($^{234}U/^{238}U$) vs. ($^{230}Th/^{238}U$) diagram showing results from this study and all (altered and unaltered) Kolbeinsey Ridge data from Elkins et al. (2011). High ($^{234}U/^{238}U$) ratios suggest the influence of alteration processes on the basalts. (c) $^{87}Sr/^{86}Sr$ vs. ($^{238}U/^{232}Th$) (top panel) and ($^{230}Th/^{238}U$) (bottom panel) in Arctic MORB (Table 3; Blichert-Toft et al., 2005; Elkins et al., 2011; Hanan et al., 2000; Neumann and Schilling, 1984; Schilling et al., 1999; Schilling et al., 1983; Sigurdsson, 1981; Waggoner, 1989). Position along the sloped data array formed by Knipovich Ridge samples in panel (a) (e.g. ($^{238}U/^{232}Th$) values) correlates with radiogenic isotope values, suggesting that source composition controls sample position along those arrays. Gakkel Ridge samples are relatively homogeneous and isotopically depleted. [To be printed in color.]

Figure 4. ^{230}Th-^{226}Ra of Arctic basalts. (^{226}Ra/^{230}Th) vs. (^{230}Th/^{238}U) disequilibria data for Arctic MORB from this study and Elkins et al. (2011), with global MORB data (Bourdon et al., 2000; Bourdon et al., 2005; Cooper et al., 2003; Kokfelt et al., 2005; Lundstrom et al., 1998a; Lundstrom et al., 1995; Lundstrom et al., 1999; Peate et al., 2001; Rubin et al., 2005; Russo et al., 2009; Sims et al., 2003; Sims et al., 2002; Standish and Sims, 2010; Sturm et al., 2000; Tepley et al., 2004; Waters et al., 2011) presented for additional comparison. Literature data have been filtered to a first order for geochemical indicators of alteration (i.e. all have measured (^{234}U/^{238}U) = 1.00 ± 1%). Off-axis global MORB are shown as symbols containing crosshairs, and definitively young, age-constrained samples are indicated with purple outlines. Gray arrow indicates general predicted decay trajectory of a relatively high-(^{226}Ra/^{230}Th) material due to aging. Age-constrained global MORB form a negative correlation that is suggested to indicate mixing of melts from different depths in MOR melting columns (Sims et al., 2002). [To be printed in color.]

Figure 5. Global (^{230}Th/^{238}U) vs. Axial Depth. Diagram of measured (^{230}Th/^{238}U) vs. axial ridge depth showing data from this study (Mohns, Knipovich, and Gakkel Ridges) and the global ridge system (Bourdon et al., 1996a; Cooper et al., 2003; Elkins et al., 2011; Lundstrom et al., 1999; Peate et al., 2001; Russo et al., 2009; Sims et al., 2003; Sims et al., 2002; Standish and Sims, 2010; Waters et al. 2011), after Bourdon et al. (1996b). We restrict the global literature data to oceanic (i.e. not Icelandic), age-constrained (i.e. (^{226}Ra/^{230}Th) and/or (^{231}Pa/^{235}U) out of equilibrium or stratigraphic age constraints), unaltered samples (i.e. (^{234}U/^{238}U) = 1.00 ± 0.01), using the filtering criteria outlined in the text; and although it generates a higher degree of scatter, we show the full, filtered global data set, rather than averaging ridge segments to reduce

local variability as in Bourdon et al. (1996b), because we are interested in examining the full range of global MORB compositions. The curves show results of peridotite reactive porous flow melting from UserCalc (Spiegelman, 2000) after calculations by Bourdon et al. (1996b) for various representative melting rates (M) and residual porosities (ϕ) as labeled, and as explained in further detail in the text. All calculations were conducted using partition coefficients as in Table 4 and assuming a 2-layer peridotitic melting source. We determined axial depth using a mantle density of 3300 kg/m^3, a crustal density of 2700 kg/m^3, and a 200 km isostatic compensation depth. Inset shows eclogitic melting for comparison (blue lines), calculated using partition coefficients as in Table 4 and melting rates of 1.1 x 10^{-4} kg/m^3/a (dashed line) and 1.9 x 10^{-4} kg/m^3/a (solid line). Our peridotite model curves (black and gray lines) are lower than those of Bourdon et al. (1996b) due to the newer partition coefficients chosen, and overall drop to low (^{230}Th/^{238}U) at lower axial depths than previous trajectories due to our use of 25 kbar instead of 20 kbar for the peridotite garnet-out reaction pressure. We additionally show the results of peridotite melting that is truncated at 20 km due to an overlying lithospheric cap (gray dashed line), which maintains higher (^{230}Th/^{238}U) at moderately high axial depths than the other peridotite melting curves. The geochemical variance observed in the global data set is likely due to a number of factors that influence melt composition, as discussed in further detail in the text. [To be printed in color.]

Figure 6. Melting Model Calculations. Diagrams showing global and Arctic MORB compositions, as well as melting model calculations, using the methods explained in the text and after Elkins et al. (2011). (a) Equiline diagram showing data as in Figure 3, with suggested compositions for depleted peridotitic DMM and enriched mafic EM-2 sources (Sims and Hart,

2006). Dashed lines and associated labels indicate the relative positions for different ^{230}Th excesses; the exact position of a calculated melt composition on any one dashed line depends on the initial source composition chosen (e.g. DMM or EM-2 sources). (b) (^{231}Pa/^{235}U) vs. (^{230}Th/^{238}U) diagram showing the global basalt data set, filtered to a first order for sample alteration as explained in the text, and including Arctic (this study; Elkins et al., 2011), Iceland (Stracke et al., 2006), global OIB (Bourdon et al., 1998; Pickett and Murrell, 1997; Pietruszka et al., 2001; Prytulak and Elliott, 2009; Sims et al., 1999; Sims et al., 1995; Sims and Hart, 2006; Sims et al., 2008b; Turner et al., 1997), and global MORB data (Goldstein et al., 1993; Kokfelt et al., 2005; Lundstrom et al., 1999; Sims et al., 1995; Sims et al., 2002; Sturm et al., 2000). We note that the age constraints indicated in the key pertain to ^{238}U-^{230}Th data, not ^{235}U-^{231}Pa, which are only age constrained in a few Arctic samples (Table 2) and a small subset of the global data set due to the shorter half-life of ^{231}Pa. Also shown are calculated melt compositions for melts extracted from the top of a dynamically-melting, garnet pyroxenite melt column (Table 4) after Elkins et al. (2011). As in that work, all modeled trajectories show calculated melt compositions that assume either variable residual melt porosities and constant melting rates ranging from 5 x 10^{-5} to 1 x 10^{-3} kg/m^3/a, *or* variable melting rates and constant porosities ranging from 0.05 % to 1 %. Compositions shown are for the top of a 106.5 km pyroxenite melt column. The two lines in bold are for reference and indicate a constant melting rate of 5 x 10^{-4} kg/m^3/a and a constant residual melt porosity of 0.5 %. (^{231}Pa/^{235}U) vs. (^{230}Th/^{238}U) diagrams for (c) a garnet peridotite melt column with a 100 km solidus and (d) an eclogite melt column with a 150 km solidus depth are also shown, likewise with Arctic data and similarly calculated model melt compositions after Elkins et al. (2011) and as explained in the text and Table 4. [To be printed in color.]

Figure 7. Magma mixing. (a) ($^{231}Pa/^{235}U$) vs. ($^{230}Th/^{238}U$) diagram showing Arctic data from this study and Elkins et al. (2011), with calculated mixing trajectories (black lines) between an eclogitic melt (with 0.5% maximum residual melt porosity and 1 x 10^{-4} kg/m^3/s melting rate; pink square) and both 0.5% porosity (light blue square) and 0.1% porosity peridotite melts (as labeled in blue text) with a melting rate of 5 x 10^{-5} kg/m^3/a, as described in the text. Tick marks along melt mixing trajectories and pink labels indicate the percentage of the melt mixture derived from an eclogitic source. Note that because the denominators of both axial isotopic ratios in Figure 7 are isotope activities of the same element (uranium), all mixing trajectories form straight lines with evenly spaced mixing intervals (tick marks). (b) ($^{238}U/^{232}Th$) vs. ε_{Nd} diagram showing Arctic MORB (this study; Elkins et al., 2011), with a calculated mixing trajectory (solid line) for binary mixing between peridotitic and eclogitic melts with 0.5% residual porosities, for the same melting rates as in (a). Tick marks and labels are the same as in panel (a). A second calculated mixture is shown (dashed line) for alternate source compositions, as explained in the text.

Table 1. Sample Information. Locations, collection data, and cruise descriptions for samples analyzed in this study.

Sample*	Ridge	Expedition	Year	Lat. (°N)	Long. (°E)	Depth (m)	Cruise log sample descriptions
END0026-009-001G	Mohns	R/V Endeavour 26	1973	71.6420	-3.0570	2220	Fresh basalt glass. **
TRI0139-030-002G	Mohns	R/V Trident 139	1971	71.8200	-2.0800	2550	Fresh basalt glass.
END0026-010-001G	Mohns	R/V Endeavour 26	1973	71.8880	-1.3930	2900	Fresh basalt glass.
END0026-010-003G	Mohns	R/V Endeavour 26	1973	71.8880	-1.3930	2900	Fresh basalt glass.
END0026-011-001G	Mohns	R/V Endeavour 26	1973	71.9900	-0.6500	2340	Fresh basalt glass.
TRI0139-031-002G	Mohns	R/V Trident 139	1971	72.1800	0.2300	2462	Fresh basalt glass.
END0026-012-002G	Mohns	R/V Endeavour 26	1973	72.3230	1.4820	2525	Fresh basalt glass.
TRI0139-032-001G	Mohns	R/V Endeavour 26	1973	72.6080	3.3750	3020	Fresh basalt glass.
END0026-014-001G	Mohns	R/V Endeavour 26	1973	72.8100	4.2630	2540	Fresh basalt glass.
TRI0139-033-002G	Mohns	R/V Trident 139	1971	73.0100	5.1800	2900	Fresh basalt glass.
END0026-015-001G	Mohns	R/V Endeavour 26	1973	73.2150	6.4380	2840	Fresh basalt glass.
END0026-016-001G	Mohns	R/V Endeavour 26	1973	73.4050	7.3880	2623	Fresh basalt glass.
END0026-032-003G	Mohns	R/V Endeavour 26	1973	73.5200	8.1080	2288	Fresh basalt glass.
END0026-030-001G	Knipovich	R/V Endeavour 26	1973	74.1950	8.8350	3210	Fresh basalt glass.
END0026-021-001G	Knipovich	R/V Endeavour 26	1973	76.5570	7.1880	2810	Fresh basalt glass.
PL96 67-2	Knipovich	R/V Professor Logatchev	1996	76.8170	7.4180	3400	Fresh basalt glass.
PL96 57-1	Knipovich	R/V Professor Logatchev	1998	76.8170	7.4180	3400	Fresh basalt glass.
PL96 54-3	Knipovich	R/V Professor Logatchev	1999	76.8170	7.4180	3400	Fresh basalt glass.
END0026-025-002G	Knipovich	R/V Endeavour 26	1973	77.5280	7.6720	2925	Fresh basalt glass.
Camper 12-1	Gakkel	R/V Oden 11	2007	85.6263	85.2398	4000	Fresh basaltic glass fragments.
Camper 13-1	Gakkel	R/V Oden 11	2007	85.6138	85.3242	4116	Sediment consisting dominantly of fresh basaltic glass shards (>80%), small crystallized basaltic fragments, and foraminifera tests.
Camper 19-1	Gakkel	R/V Oden 11	2007	85.6047	85.2517	3910	Sheet flow with drape textures. Glassy outer surfaces, some showing slight weathering. Fine grained; plag. mpc. <<1%.

Table 1. (cont.)

Sample*	Ridge	Cruise	Year	Lat. (°N)	Long. (°E)	Depth (m)	Description
Camper 20-1	Gakkel	R/V Oden 11	2007	85.5945	85.5275	4023	Pillow bud broken from large pillow. Glassy outer rim up to 1 cm thick – fresh except for outer layer that has white alteration along cracks in glass.
Camper 23-1	Gakkel	R/V Oden 11	2007	85.5992	85.5817	4131	Glassy, large pillow bud broken from pillow. Parts of it are glass only; interior portion is fine-grained, plag. mpc (<1%). Outer surface of some of glass weathered; rock is fresh to slightly weathered.
Camper 23-1 glass	Gakkel	R/V Oden 11	2007	85.5992	85.5817	4131	Loose glass from Camper 23-1.
Camper 25-1	Gakkel	R/V Oden 11	2007	85.6048	85.2845	3904	Glassy, large pillow bud broken from pillow. Interior portion is fine-grained, plag. mpc (<<1%). Vesicles <<1%. Glass fresh except outer layer with white alteration along cracks.

* All samples collected by dredge, except for Gakkel Ridge samples collected using the Camper ROV. Start and end locations are not available for dredged samples due to the age of research expeditions.

** Cruise descriptions of samples from older expeditions are very brief. We report them here for completeness, with the further note that all samples were carefully handpicked for fresh, unaltered glass chips prior to analysis in this study.

ACCEPTED MANUSCRIPT

Table 2. Results of U-Th-Ra-Pb analyses.[+] ($^{234}U/^{238}U$) values in bold are considered in equilibrium and thus uncontaminated by seawater.*

Sample**	Ridge	Th (ppm)	U (ppm)	Pa (fg/g)	(^{230}Th)/(^{238}U)	(^{238}U)/(^{232}Th)	(^{230}Th)/(^{232}Th)	(^{234}U)/(^{238}U) [†]	(^{226}Ra)/(^{230}Th)	(^{231}Pa)/(^{235}U) [#]	(^{210}Po)[d] (dpm)	(^{210}Pb)/(^{226}Ra)	Age Constraint [e]
END0026-009-001G[b]	Mohns	1.30	0.335	-	1.297	0.784(16)	1.017(1)	**1.003(1)**	1.05(3)	-			< 8 ka
TRI0139-030-002G[a]	Mohns	2.11	0.541	-	1.247	0.777(3)	0.969(3)	1.003(2)	-	-			
(separate dissolution)[b]	Mohns	2.01	0.523	-	1.253	0.790(19)	0.990(2)	1.004(1)	1.00(3)	-			
Average		*2.06*	*0.532*	-		*0.784*	*0.980*	***1.003***	*1.00*				< 375 ka
END0026-010-001G[a]	Mohns	0.661	0.174	-	1.209	0.799(10)	0.97(1)	1.001(2)	-	-			
(replicate analysis)[a]	Mohns	0.662	0.171	92.1	1.231	0.783(24)	0.964(3)	1.001(2)	-	1.64(1)			
(separate dissolution)[a]	Mohns	0.702	0.182	92.7	1.233	0.787(19)	0.970(6)	1.003(2)	-	1.55(6)			
(separate dissolution)[a]	Mohns	-	0.172	-	-	-	-	0.999(2)	-	-			
(separate dissolution)[b]	Mohns	0.650	0.174	-	1.204	0.809(19)	0.974(1)	1.004(1)	-	-			
(separate dissolution)[b]	Mohns	0.645	0.172	-	1.196	0.808(21)	0.966(2)	1.002(1)	1.08(3)	-			
Average		*0.664*	*0.174*	*92.4*		*0.797*	*0.968*	***1.002***	*1.08*	*1.60*			< 8 ka
END0026-010-003G[b]	Mohns	0.646	0.170	-	1.252	0.798(18)	0.999(1)	**1.005(1)**	0.99(3)	-			< 375 ka
END0026-011-001G[b,]	Mohns	1.02	0.270	-	1.245	0.805(22)	1.002(1)	-	1.05(3)	-			< 8 ka
TRI0139-031-002G[b]	Mohns	0.373	0.102	-	1.016	0.831(17)	0.844(3)	**1.003(1)**	-	-			< 375 ka
END0026-012-002G[a]	Mohns	1.87	0.499	-	1.178	0.809(2)	0.953(23)	1.001(2)	-	-			
(replicate analysis)[a]	Mohns	1.86	0.502	225.1	1.170	0.820(5)	0.959(5)	0.999(2)	-	1.37(1)			
(separate dissolution)[a]	Mohns	-	0.497	-	-	-	-	0.999(2)	-	-			
(separate dissolution)[b]	Mohns	1.85	0.501	-	1.197	0.823(21)	0.985(1)	1.0041(5)	0.97(3)	-			
Average		*1.86*	*0.500*	*225.1*		*0.816*	*0.966*	***1.001***	*0.97*	*1.37*			< 150 ka
TRI0139-032-001G[b]	Mohns	0.539	0.150	-	1.072	0.842(19)	0.903(3)	**1.003(1)**	-	-			< 375 ka
END0026-014-001G[a]	Mohns	0.130	0.078	42.6	1.075	1.83(4)	1.967(3)	1.022(2)	-	1.68(1)			
(separate dissolution)[a]	Mohns	-	0.077	-	-	-	-	1.022(2)	-	-			
Average		*0.130*	*0.078*	*42.6*		*1.83*	*1.967*	*1.022*	-	*1.68*			
TRI0139-033-002G[b]	Mohns	0.535	0.146	-	1.143	0.828(16)	0.946(2)	**1.005(1)**	-	-			< 375 ka
END0026-015-001G[b]	Mohns	0.693	0.184	-	1.177	0.803(15)	0.945(1)	**1.005(1)**	1.24(4)	-			< 8 ka
END0026-016-001G[b]	Mohns	0.126	0.041	-	1.047	0.979(19)	1.025(5)	1.016(1)	-	-			

Table 2 (cont.).

Sample**	Ridge	Th (ppm)	U (ppm)	Pa (fg/g)	(^{230}Th)/(^{238}U)	(^{238}U)/(^{232}Th)	(^{230}Th)/(^{232}Th)	(^{234}U)/(^{238}U) †	(^{226}Ra)/(^{230}Th)	(^{231}Pa)/(^{235}U) #	(^{210}Po)[d] (dpm)	(^{210}Pb)/(^{226}Ra)	Age Constraint [e]
END0026-032-003G[b]	Mohns	0.213	0.062	-	1.082	0.888(19)	0.961	1.006(1)	-	-			
END0026-030-001G[a]	Knipovich	1.29	0.322	-	1.203	0.755(4)	0.908(3)	0.996(2)	-	-			
(separate dissolution)[a]	Knipovich	0.972	0.240	-	1.213	0.748(6)	0.907(5)	1.000(2)	-	-			
(separate dissolution)[a]	Knipovich	-	0.242	129.8	-	-	-	0.994	-	1.65(1)			
(separate dissolution)[b]	Knipovich	0.936	0.237	-	1.172	0.769(15)	0.901(3)	1.000(1)	1.08(3)	-			
Average		*0.95*	*0.240*	*129.8*		*0.757*	*0.905*	***0.998***	*1.08*	*1.65*			< 8 ka
END0026-021-001G[b]	Knipovich	0.489	0.160	-	1.075	0.994(20)	1.069(2)	1.009(5)	-	-			
END0026-025-002G[b]	Knipovich	0.743	0.226	-	1.101	0.921(18)	1.014(1)	**1.003(1)**	1.24(4)	-			< 8 ka
PL96 67-2[c, *]	Knipovich	0.760	0.234	-	1.156	0.934(7)	1.08(2)	-	-	-			< 375 ka
PL96 57-1[c, *]	Knipovich	0.452	0.140	-	1.202	0.940(4)	1.13(1)	-	-	-			< 375 ka
PL96 54-3[c, *]	Knipovich	0.570	0.170	-	1.182	0.905(5)	1.07 (1)	-	-	-			< 375 ka
Camper 12-1[b]	Gakkel	0.190	0.086	-	1.018	1.369(26)	1.394(3)	**1.0037(4)**	3.2(1)	-	0.20(1)	0.96(10)	< 8 ka
Camper 13-1[b]	Gakkel	0.194	0.085	-	1.045	1.327(27)	1.387(3)	**1.002(1)**	3.07(9)	-			< 8 ka
Camper 19-1[b]	Gakkel	0.196	0.083	-	1.051	1.286(24)	1.352(3)	**1.001(1)**	3.3(1)	-	0.20(1)	0.94(9)	< 8 ka
Camper 20-1[b]	Gakkel	0.205	0.092	-	0.999	1.359(26)	1.358(2)	**1.0019(4)**	3.5(1)	-	0.22(1)	0.93(11)	< 8 ka
Camper 23-1[b]	Gakkel	0.181	0.083	-	0.955	1.386(28)	1.323(2)	**1.0023(4)**	3.4(1)	-			< 8 ka
Camper 25-1[b]	Gakkel	0.180	0.080	-	0.995	1.356(31)	1.349(2)	**1.0025(6)**	3.6(1)	-			< 8 ka

[a] Sample analyzed for U, Th concentrations and isotopes by MC-ICP-MS (ThermoFinnigan Neptune) at the University of Bristol. Th concentration and isotopic data are not presented for a sample batch for which Th was not successfully extracted; analyses of affected samples were replicated on either a second aliquot or the same dissolution or on separate dissolutions, as indicated. Concurrent standard runs are presented in Elkins et al. (2011) and Prytulak et al. (2008).

[b] Sample dissolved and analyzed for U, Th, and/or Ra concentrations and isotopes by ICP-MS at WHOI, with concurrent standard runs presented in Elkins et al. (2011). In cases of replicates with Bristol University, all WHOI analyses were conducted using separate sample dissolutions, as indicated.

[c] Sample analyzed for U and Th concentrations and isotopes by MC-ICP-MS at the University of Kiel.

[d] (^{210}Pb) measured by alpha counting of ^{210}Po at the University of Iowa; uncertainties reported as 1s standard error.

[e] Age limits for samples measured in this study, based on isotopic disequilibria. No constraints reported for samples with (^{234}U/^{238}U) > 1.000.*

* (^{234}U/^{238}U) was measured to determine sample alteration. One unsuccessful sample from WHOI and three samples from Kiel were not measured for (^{234}U/^{238}U). Samples considered in U isotopic equilibrium are indicated in bold.

Table 2 (cont.).

Standard		Th (ppm)	U (ppm)	Pa (fg/g)	(^{230}Th)/(^{238}U)	(^{238}U)/(^{232}Th)	(^{230}Th)/(^{232}Th)	(^{234}U)/(^{238}U) †	(^{226}Ra)/(^{230}Th)	(^{231}Pa)/(^{235}U) #	(^{210}Po)[d] (dpm)	(^{210}Pb)/(^{226}Ra)	Age Constraint [e]
ATh-O	09/06 [f]	7.532	2.351		1.08(2)	0.95(2)	1.018(1)	1.00634(5)					
ATh-O	10/07 [f]	7.385	2.302		1.08(3)	0.95(2)	1.017(1)	1.0038(6)					
BHVO-1	09/06 [f]	1.207	0.4344		0.99(2)	1.09(2)	1.081(1)	1.00305(7)					
W-2	09/06 [f]	2.157	0.5101		0.98(2)	0.72(1)	0.7049(4)	1.0049(1)					
BCR-1	03/08 [f]	5.665	1.683		0.98(2)	0.90(2)	0.884(1)	1.00408(9)					
TML	03/08 [f]	29.789	10.505		1.00(2)	1.07(2)	1.070(1)	1.00274(4)					
BCR-2	Average [g]	5.835	1.670			0.874(9)	0.87(1)	1.0025(4)		1.00(1)			
TML	Average [g]	29.705	10.481			0.935(4)	1.070(8)	0.9995(8)					

** Each line of data represents results for a single extraction and analytical run, consisting of ICP-MS or MC-ICP-MS sample blocks of 20+ analyses.

† Data are reported using the following decay constant values: $\lambda_{U\text{-}238} = 1.551 \times 10^{-10}$ (Jaffey et al., 1971), $\lambda_{Th\text{-}232} = 4.948 \times 10^{-11}$ (LeRoux and Glendenin, 1963), $\lambda_{Th\text{-}230} = 9.158 \times 10^{-6}$, (Cheng et al., 2000), $\lambda_{U\text{-}234} = 2.826 \times 10^{-6}$ (Cheng et al., 2000).

+ Uncertainty reported is percent 2σ standard error, unless stated otherwise.

Pa concentration and isotopic standard analyses and uncertainties reported in Prytulak et al. (2008).

[f] Rock standard measured with samples for this study at WHOI, as previously reported in Elkins et al. (2011).

[g] Average of multiple rock standard analysis including several standards run with samples for this study at the University of Bristol, as previously reported in Prytulak et al. (2008).

ACCEPTED MANUSCRIPT

Table 3. Radiogenic Isotope Measurements. Measured Sr, Pb, Nd, and Hf isotopes in samples analyzed for this study.[a]

Sample	Ridge	$^{143}Nd/^{144}Nd$	ε_{Nd}	$^{176}Hf/^{177}Hf$	ε_{Hf}	$^{87}Sr/^{86}Sr$	$^{206}Pb/^{204}Pb$	$^{207}Pb/^{204}Pb$	$^{208}Pb/^{204}Pb$
TRI0139-032-001G	Mohns	0.513065(5)[+]	8.33	0.283363(5)	20.90				
END0026-032-003G	Mohns	0.513101(5)	9.03	0.283388(5)	21.78				
PL96 67-2	Knipovich	0.513091(7)	8.84			0.703064(31)	18.310 (2)	15.468(2)	38.026(5)
PL96 57-1	Knipovich	0.513128(10)	9.56				18.194(4)	15.429(4)	37.826(9)
PL96 54-3	Knipovich	0.513127(10)	9.54			0.702843(12)	18.209(1)	15.442(2)	37.876(3)
Camper 12-1	Gakkel	0.513134(4)	9.67	0.283210(3)	15.50	0.702621(10)	18.0170(1)	15.4356(1)	37.6198(6)
Camper 13-1	Gakkel	0.513139(4)	9.76	0.283207(3)	15.40	0.702626(10)	18.0141(5)	15.4363(5)	37.619(2)
Camper 19-1	Gakkel	0.513139(5)	9.78	0.283207(3)	15.38	0.702615(10)	18.0083(3)	15.4342(2)	37.6084(7)
Camper 20-1	Gakkel	0.513147(5)	9.93	0.283216(4)	15.71	0.702653(10)	18.0400(3)	15.4383(3)	37.6465(8)
Camper 23-1	Gakkel	0.513162(5)	10.22	0.283215(3)	15.66	0.702574(10)	17.9382(3)	15.4270(3)	37.5402(8)
Camper 23-1 glass	Gakkel	0.513147(4)	9.93	0.283197(3)	15.02	0.702574(10)	17.9389(2)	15.4282(2)	37.5439(4)
Camper 25-1	Gakkel	0.513140(5)	9.79	0.283208(4)	15.43	0.702623(10)	18.0135(3)	15.4365(3)	37.618(1)

[a] $^{176}Hf/^{177}Hf$ and $^{143}Nd/^{144}Nd$ in Mohns and Gakkel Ridge samples measured by MC-ICP-MS at the Ecole Normale Supérieure de Lyon, and normalized relative to 179Hf/177Hf = 0.7325 and $^{146}Nd/^{144}Nd$ = 0.7219, respectively. Uncertainties are 2σ standard errors. $^{176}Hf/^{177}Hf$ of JMC-475 Hf standard = 0.282160 ± 0.000010 (n=15); $^{143}Nd/^{144}Nd$ of Rennes in-house standard = 0.511961± 0.000013 (n=50) (Chauvel and Blichert-Toft, 2001). $^{87}Sr/^{86}Sr$, $^{206}Pb/^{204}Pb$, $^{207}Pb/^{204}Pb$, and $^{208}Pb/^{204}Pb$ in Mohns and Gakkel Ridge samples measured by MC-ICP-MS (ThermoFinnigan Neptune) at WHOI, with Sr standard NBS987 $^{87}Sr/^{86}Sr$ = 0.710240 ± 0.000020, Pb standard NBS981 $^{206}Pb/^{204}Pb$ = 16.9356, $^{207}Pb/^{204}Pb$ = 15.4891, and $^{208}Pb/^{204}Pb$ = 36.7006; internal precisions for these ratios ranges from 15-30 ppm, external reproducibility ranges from 17 ppm for $^{207}Pb/^{204}Pb$ to 117 ppm for $^{208}Pb/^{204}Pb$ (Hart and Blusztajn, 2006), and samples analyzed for Pb were compared with internal Tl standard and by repeat analysis of NBS981 (Hart and Blusztajn, 2006; Sims and Hart, 2006). $^{87}Sr/^{86}Sr$, $^{206}Pb/^{204}Pb$, $^{207}Pb/^{204}Pb$, and $^{208}Pb/^{204}Pb$ of Knipovich Ridge samples measured on a ThermoFinnigan MAT262 at GEOMAR, Kiel, Germany following procedures of Haase et al (2004).

[+] All uncertainties reported are 2σ standard error.

ACCEPTED MANUSCRIPT

Table 4: Mineral/melt partition coefficients and mineral modes for melting model calculations. D_{Pa} = 1 x 10^{-5} for all models.*

	Mineral/melt partition coefficient D_i			Mineral
	U	**Th**	**Nd**	**Mode**
	Garnet peridotite [a]			
Garnet	0.038	0.017	0.074	0.12
Clinopyroxene	0.0030	0.0040	0.072	0.08
Olivine	0.00005	0.00047	0.001	0.59
Orthopyroxene	0.0078	0.0086	0.021	0.21
	Spinel peridotite [a]			
Clinopyroxene	0.0080	0.0070		0.20
Olivine	0.00005	0.00047		0.60
Orthopyroxene	0.0024	0.0027		0.20
	Garnet pyroxenite [b]			
Garnet	0.013	0.0032		0.40
Clinopyroxene	0.017	0.015		0.60
	Eclogite [c]			
Garnet	0.024	0.0042	0.290	0.25
Clinopyroxene	0.0041	0.0032	0.122	0.75

* Peridotite melting calculations assume a U_0 (initial U concentration) of 0.0018 ppm, Th_0 of 0.00071, and Pa_0 of 5.81 x 10^{-7} ppb. The peridotite melting interval is 450 ºC, while the eclogite melting interval is 100 ºC (where "melting interval" refers to the isobaric temperature difference between the liquidus and the solidus).

[a] Partition coefficients from Salters et al. (2002).

[b] Partition coefficients from Elkins et al. (2008).

[c] Partition coefficients from Pertermann et al. (2004).

ACCEPTED MANUSCRIPT

Figure 1

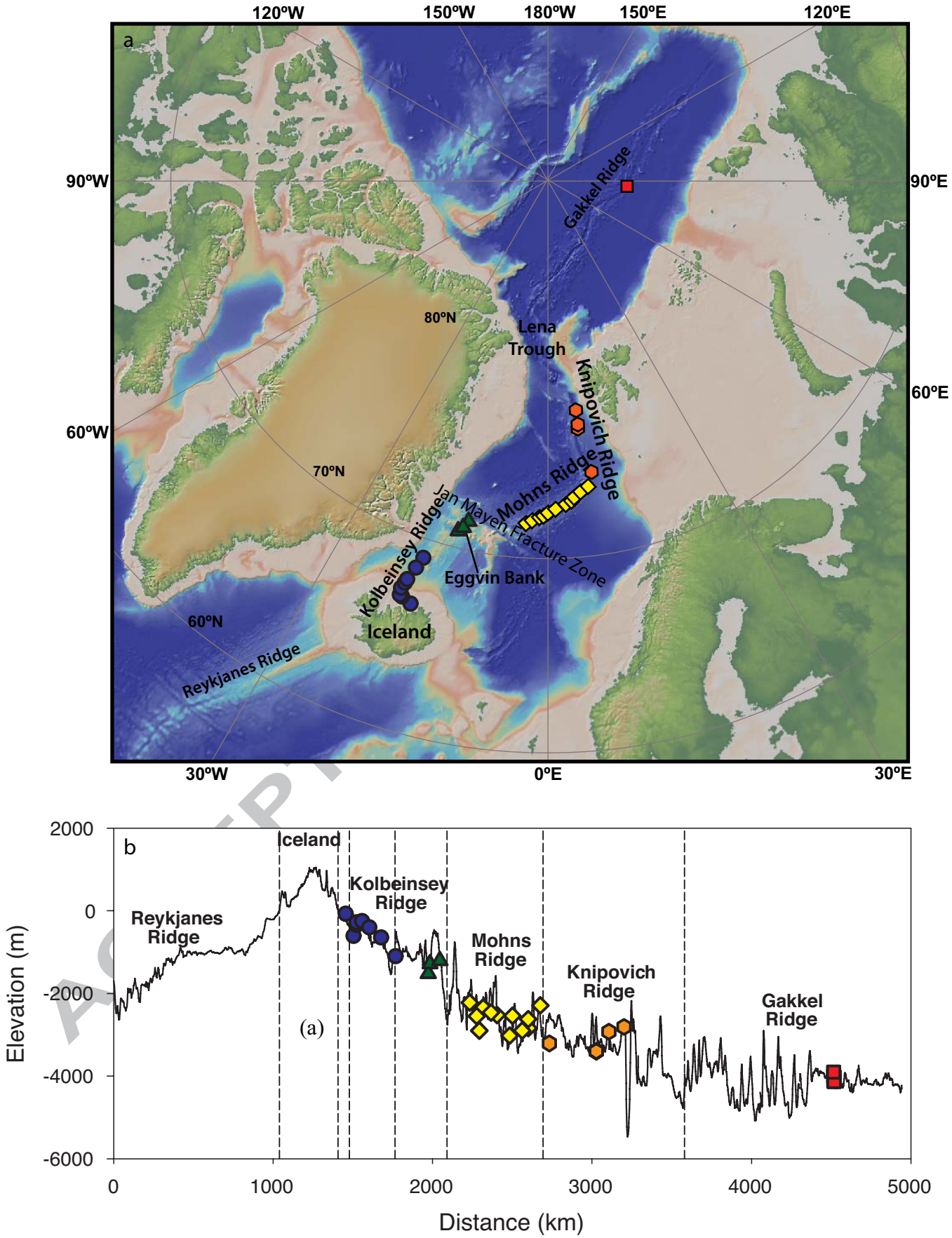

Figure 1

Figure 2

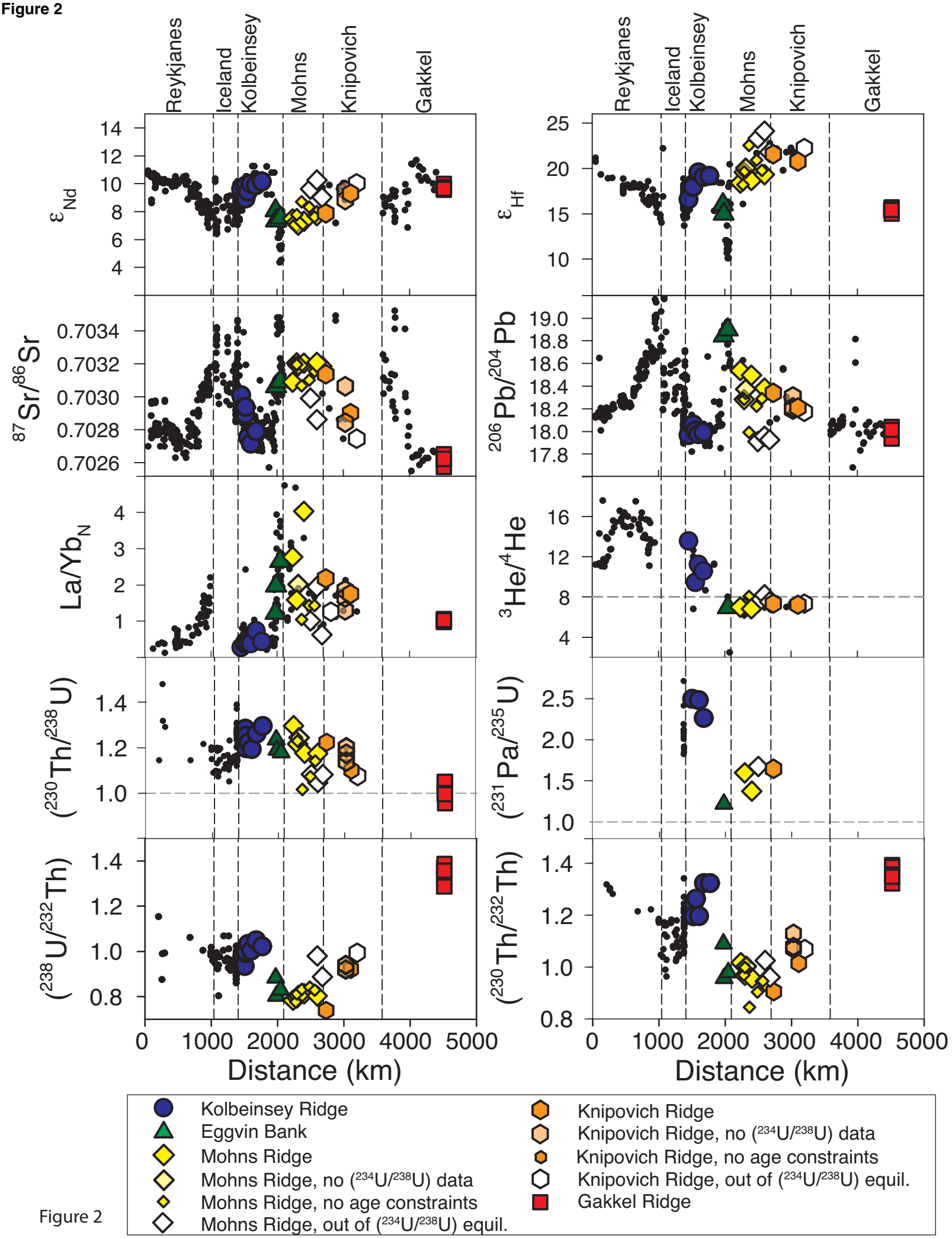

Figure 2

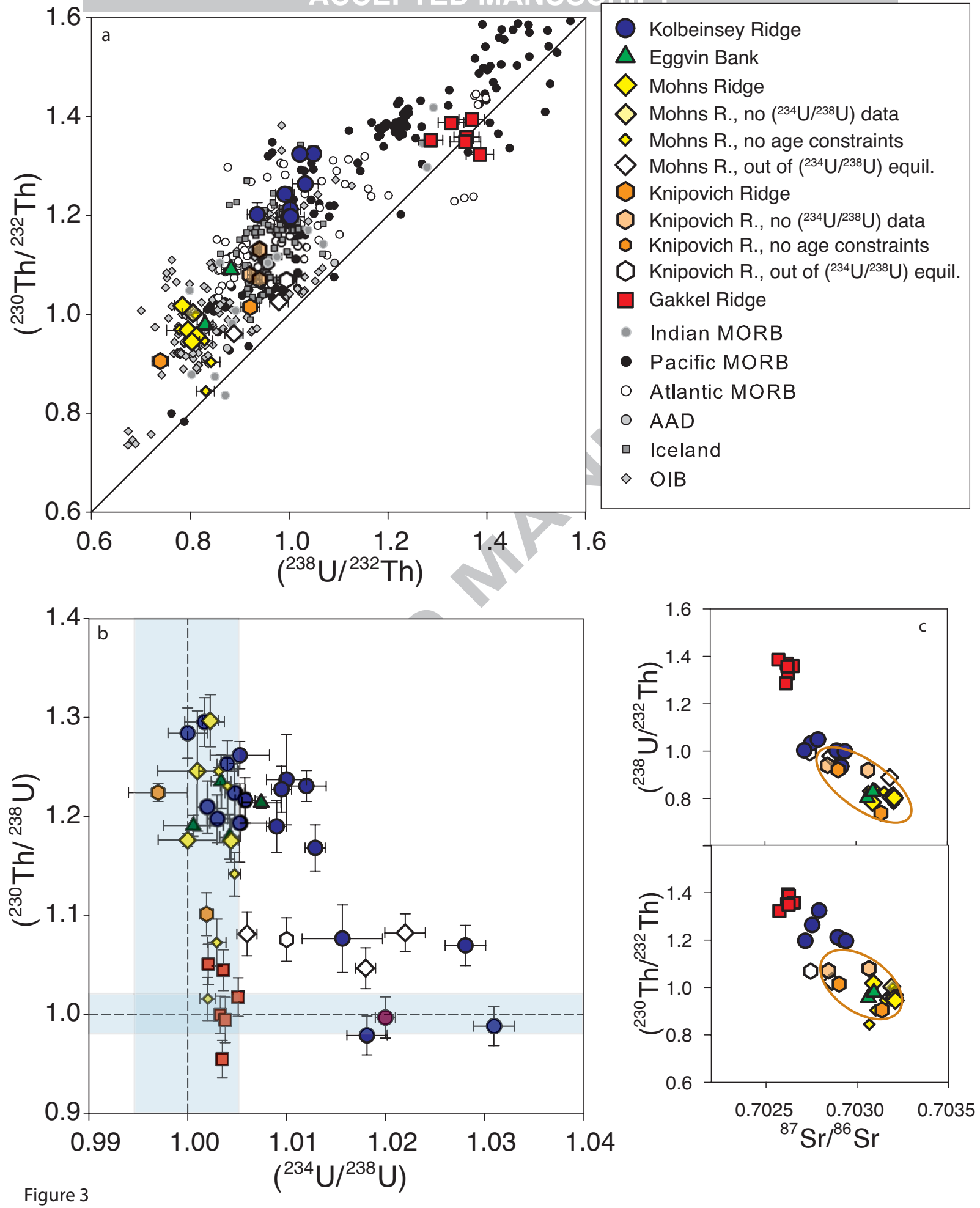

Figure 3

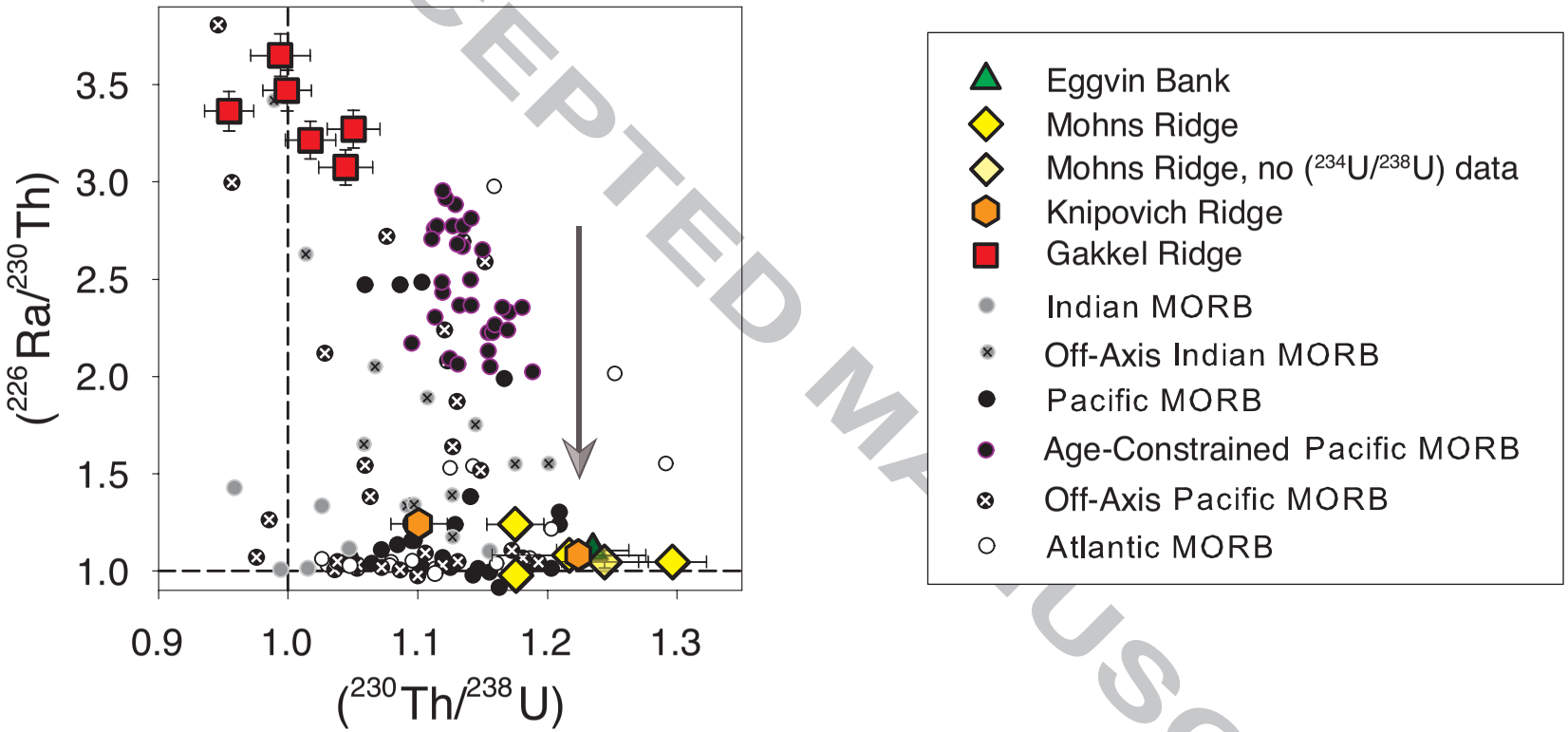

Figure 4

ACCEPTED MANUSCRIPT

Figure 5

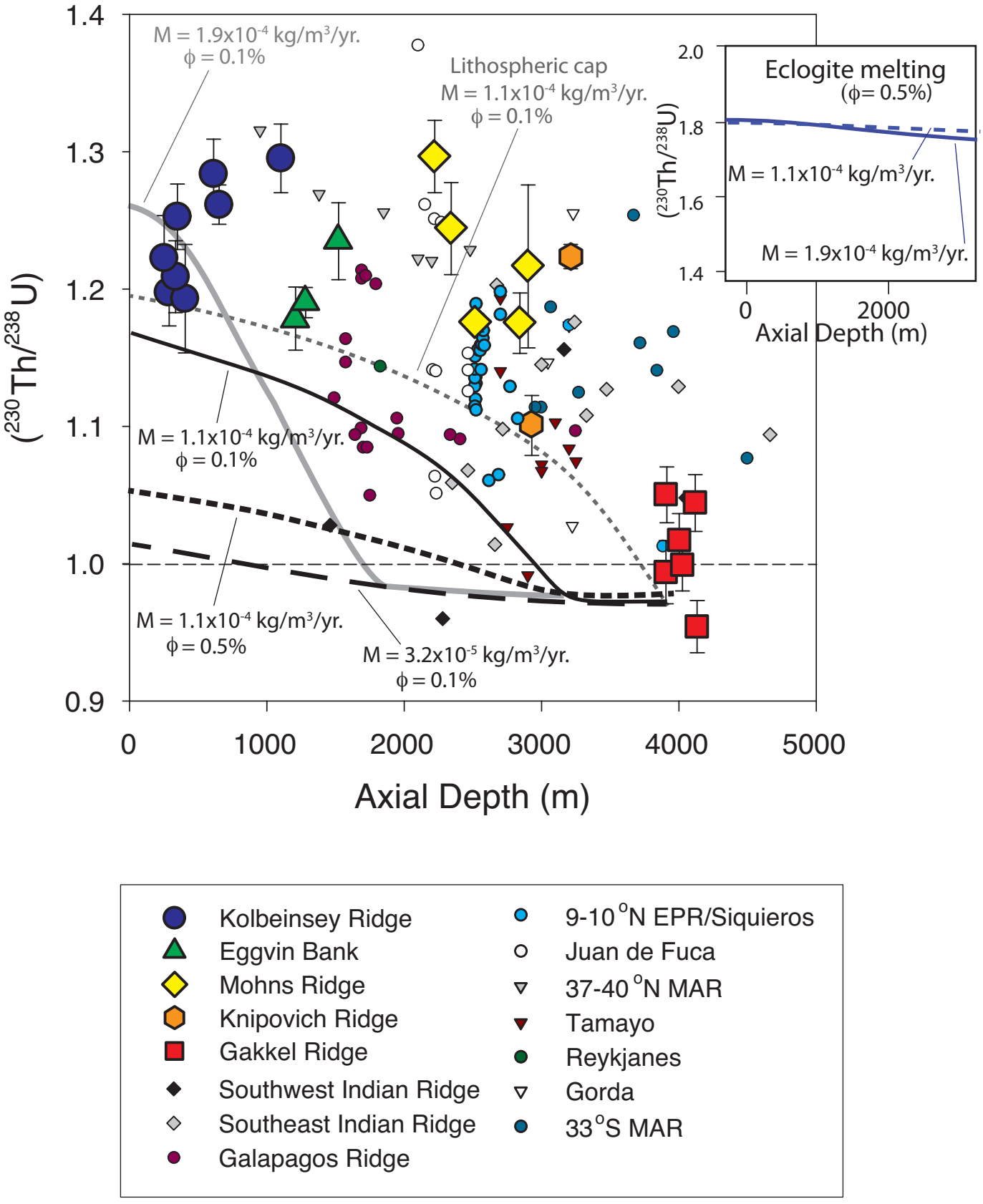

Figure 5

Figure 6

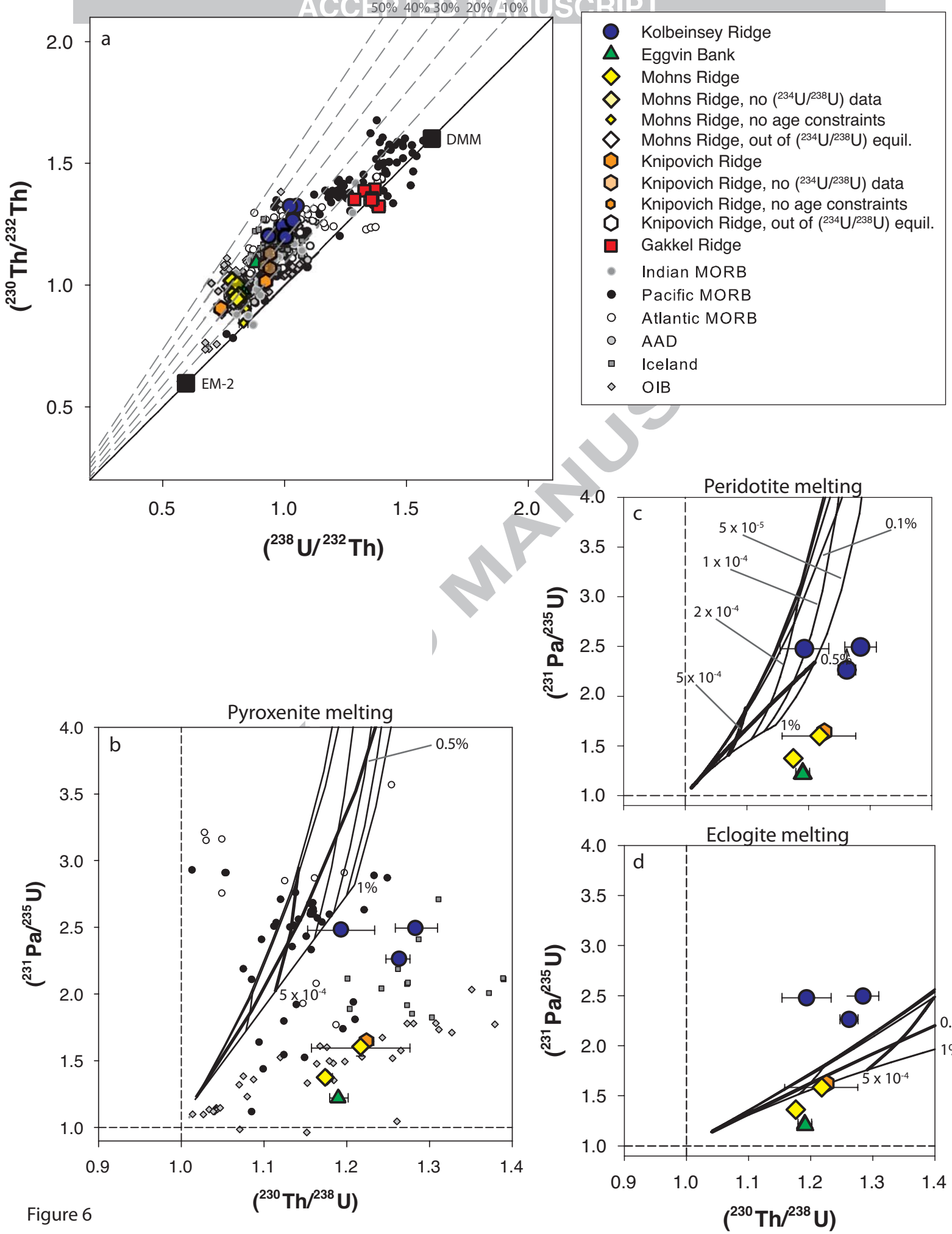

Figure 6

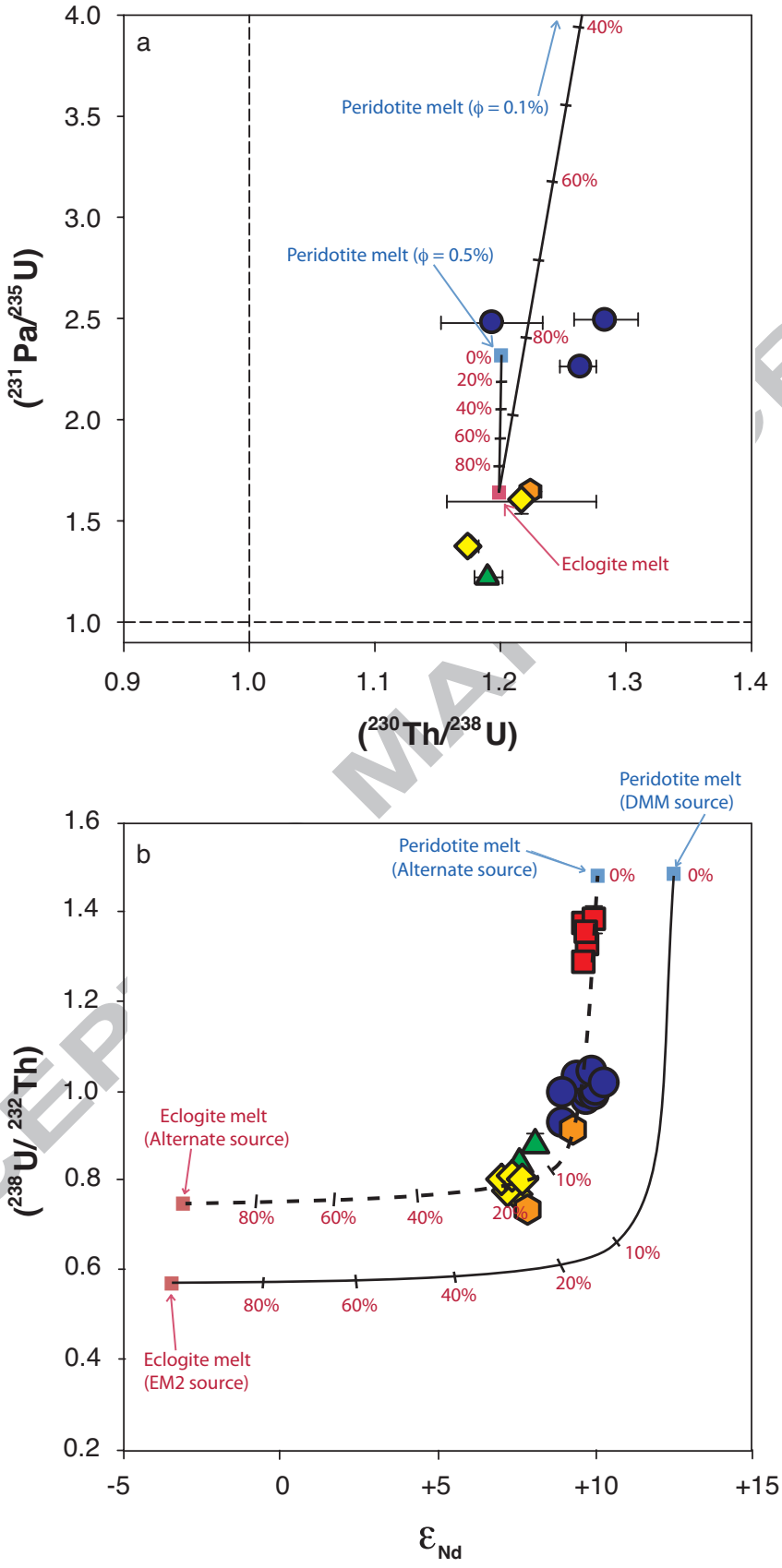

Figure 7